bioRxiv preprint doi: https://doi.org/10.1101/2021.06.08.447555; this version posted June 8, 2021. The copyright holder for this preprint (which was not certified by peer review) is the author/funder. All rights reserved. No reuse allowed without permission.

The Ebola virus matrix protein clusters phosphatidylserine, a critical step in viral budding

Monica L. Husby[1,2], Souad Amiar[1,2¶], Laura I. Prugar[3¶], Emily A. David[1&], Caroline B. Plescia[1&], Kathleen E. Huie[3&], Jennifer M. Brannan[3], John M. Dye[3], Elsje Pienaar[2,4], Robert V. Stahelin[1,2*]

[1] Department of Medicinal Chemistry & Molecular Pharmacology, Purdue University, West Lafayette, Indiana, United States of America

[2] Purdue Institute of Inflammation, Immunology and Infectious Disease (PI4D), Purdue University, West Lafayette, Indiana, United States of America

[3] United States Army Medical Research Institute of Infectious Diseases USAMRIID, Fort Detrick, Frederick, Maryland, United States of America

[4] Weldon School of Biomedical Engineering, Purdue University, West Lafayette, Indiana, United States of America

*Corresponding author

E-mail:rstaheli@purdue.edu (RVS)

[¶] These authors contributed equally to this work

[&] These authors also contributed equally to this work

Running title: Targeting PS levels to inhibit EBOV

Keywords: Ebola virus, fendiline, filovirus, matrix protein, phosphatidylserine, plasma membrane, viral budding, VP40

bioRxiv preprint doi: https://doi.org/10.1101/2021.06.08.447555; this version posted June 8, 2021. The copyright holder for this preprint (which was not certified by peer review) is the author/funder. All rights reserved. No reuse allowed without permission.

Abstract

Phosphatidylserine (PS) has been shown to be a critical lipid factor in the assembly and spread of numerous lipid enveloped viruses. Here, we describe the ability of the Ebola virus (EBOV) matrix protein eVP40 to induce clustering of PS and promote viral budding *in vitro*, as well as the ability of an FDA approved drug, fendiline, to reduce PS clustering subsequently reducing virus budding and entry. To gain mechanistic insight into fendiline inhibition of EBOV replication, multiple *in vitro* assays were employed including imaging, viral budding and viral entry assays. Fendiline reduced the PS content in mammalian cells and PS in the plasma membrane, reducing the ability of VP40 to form new virus particles. Further, particles that do form from fendiline treated cells have altered particle morphology and decreased infectivity capacity. These complementary studies reveal the mechanism by which filovirus matrix proteins cluster PS to enhance viral assembly, budding, and spread from the host cell while also laying the groundwork for fundamental drug targeting strategies.

bioRxiv preprint doi: https://doi.org/10.1101/2021.06.08.447555; this version posted June 8, 2021. The copyright holder for this preprint (which was not certified by peer review) is the author/funder. All rights reserved. No reuse allowed without permission.

Introduction

Ebola virus (EBOV), which was first discovered in 1976[1,2], has been of much concern recently due to an ongoing outbreak in the Democratic Republic of Congo as well as the unprecedented 2014-16 outbreak in Western Africa. The FDA recently approved an EBOV vaccine that shows efficacy when administered prior to virus exposure[3]; however, the duration and breadth of these recent outbreaks underscore that with an increasingly interconnected world, the dangers of reoccurring outbreaks are increasingly high and there is an imminent need to develop small molecule counter measures to treat patients who test positive for EBOV and exhibit symptoms. Further, there is still a large gap in knowledge in how EBOV hijacks host cell components to replicate and spread from cell-to-cell, elucidation of which may identify new drug targets.

In the Filoviridae family, EBOV and Marburg virus (MARV) are two of the most highly pathogenic viruses. EBOV and MARV are lipid enveloped negative-sense single stranded RNA viruses[4,5]. One commonly overlooked characteristic of many pathogenic viruses, including EBOV and MARV, is their lipid envelope, which is acquired from the host cell they infect. Furthermore, lipid enveloped negative-strand RNA viruses possess limited viral machinery, often encoding for just a handful of viral proteins. Amongst these viral proteins is the multi-functional matrix protein. These matrix proteins, including the VP40 protein of Ebola (eVP40) and Marburg (mVP40) viruses, are essential to efficient viral assembly and egress. In fact, independent expression of eVP40 or mVP40 leads to the production of virus-like particles (VLPs), nearly indistinguishable from infectious virions[6–8]. Although these matrix proteins travel through different trafficking pathways within cells, they coalesce at the plasma membrane (PM) to form the viral matrix, which

bioRxiv preprint doi: https://doi.org/10.1101/2021.06.08.447555; this version posted June 8, 2021. The copyright holder for this preprint (which was not certified by peer review) is the author/funder. All rights reserved. No reuse allowed without permission.

directs viral assembly, budding and the acquisition of their characteristic lipid envelope[9–13]. Importantly, phosphatidylserine (PS) has been implicated in recruiting matrix proteins to the PM and coordinating the assembly of progeny virions[14–16].

While lipids play a critical role in assembly of progeny viral particles, lipids are also actively involved in viral entry in a phenomenon known as “apoptotic mimicry”. Apoptotic mimicry is central to the efficient entry of numerous lipid-enveloped viruses[17–19]. During apoptotic mimicry, PS is transferred from the inner to the outer leaflet of the PM; this causes PS to become a component of the outer viral envelope during infection[14,20,21]. Subsequently, the exposed PS in the viral envelope is recognized by target cell receptors for viral uptake, continuing the viral lifecycle[18,22,23].

The two bilayers of the PM have varying compositions of four main phospholipid classes asymmetrically distributed across the two bilayers[24,25]. However, the most abundant anionic lipid within the inner leaflet of the PM is PS, a frequent participant in peripheral protein recruitment[26]. Extensive work has looked at the dynamic nature of lipids within the PM, including PS, and their tendency to cluster into domains several hundred nanometers in size[15,27,28]. Clustering of anionic lipids into domains enriches regions of the PM with anionic charge, creating a platform for electrostatic interactions at the PM and cytosolic interface for peripheral protein recruitment. This phenomenon has been reported between PS and the matrix protein of influenza A virus[15]. Although significant work has underscored the importance of PS in filovirus budding and entry[14,18,22,29–32], the molecular details of the interaction has not been explored in the context of the lateral organization of PS, matrix assembly or implications on viral spread.

bioRxiv preprint doi: https://doi.org/10.1101/2021.06.08.447555; this version posted June 8, 2021. The copyright holder for this preprint (which was not certified by peer review) is the author/funder. All rights reserved. No reuse allowed without permission.

Recently, an FDA approved drug, fendiline, was reported to reduce PS levels within the PM inner leaflet[33,34], which was sufficient to inhibit the oncogenic protein K-Ras PM localization and signaling[34,35]. Fendiline was initially approved by the FDA in the 1970s as a non-selective calcium channel blocker to treat coronary heart disease[36]; however, these recently identified off target properties were found to be calcium independent and associated with the indirect inhibition of acid sphingomyelinase (ASM)[33,34]. eVP40 and mVP40 have been shown to utilize PS for their PM localization, assembly, and production of progeny virions; however, detailed molecular insight into this relationship is lacking. To delineate the molecular architecture and requirements of PS concentration on VP40 assembly, oligomerization and budding, we employed biochemical and biophysical assays *in vitro* and in cells. We also tested the ability and mechanism by which VP40 clusters PS *in vitro* and in cells. We hypothesized that reduction of PS from the PM with fendiline treatment would perturb filovirus assembly and inhibit viral budding. Lastly, fendiline treatment was tested as a potential therapy for inhibition of EBOV budding and spread in biosafety level (BSL)-2 and BSL-4 models of infection. Our results demonstrate that VP40 clusters PS, a critical requirement for viral budding, spread and subsequent entry that can be inhibited with the FDA-approved drug fendiline.

Results

EBOV VP40 localizes to PS enriched regions in synthetic membranes and in living cells

bioRxiv preprint doi: https://doi.org/10.1101/2021.06.08.447555; this version posted June 8, 2021. The copyright holder for this preprint (which was not certified by peer review) is the author/funder. All rights reserved. No reuse allowed without permission.

Previous work investigating the relationship between PS and eVP40 has been limited to the transient expression of the PS probe, GFP-LactC2, and PS-deficient cell lines[14,29]. The drawback to these techniques is the inability to capture PS and eVP40 localization simultaneously, as GFP-LactC2 and GFP-eVP40 compete for PS binding within the PM. To overcome this limitation, we utilized a synthetic fluorescent analogue of PS, TopFluor® TMR-PS (tetramethylrhodmaine-PS (TMR-PS)) which permits visualization of PS and eVP40 localization and dynamics in real time in synthetic membranes and in cells.

It was previously reported that eVP40 has selectivity and high affinity for PS and PI(4,5)P_2, both *in vitro* and in cells[14,31,37–40]. To test if eVP40 colocalizes with PS, we employed a TMR-PS labelled giant unilamellar vesicle (GUV) system with fluorescently labelled His_6-eVP40. Because of their large size, GUVs are a reliable tool for fluorescence analysis of lipid-protein interactions by confocal microscopy. To simultaneously image eVP40 and PS localization, we generated an Alexa-488 conjugated His_6-eVP40 dimer (eVP40-Alexa488) through conjugation of the fluorophore to two cysteine residues within the dimer structure (positions 311 and 314) using a previously described protocol[41]. First, we tested the ability of conjugated eVP40 to bind control and anionic membranes by incubating different GUVs with eVP40-Alexa488. Confocal microscopy was performed and fluorescence plot profile analysis of both eVP40-Alexa488 and TMR-PS was analyzed (Expanded View Fig. 1a-d). As expected, no significant overlap of fluorescence signals was observed following incubation of eVP40-Alexa488 with control GUVs (DPPC:Chol) (Expanded View Fig. 1a *left panel* & Expanded View Fig 1b). Furthermore, the quantification of protein enrichment showed no eVP40 enrichment on this control

bioRxiv preprint doi: https://doi.org/10.1101/2021.06.08.447555; this version posted June 8, 2021. The copyright holder for this preprint (which was not certified by peer review) is the author/funder. All rights reserved. No reuse allowed without permission.

membrane despite the presence of 0.2 % anionic fluorescent PS (enrichment index 1.0 ± 0.2, Expanded View Fig. 1e). This result clearly supports previous data demonstrating that eVP40 membrane binding is anionic lipid dose-dependent[14,31,39] requiring a level of PS similar to that found at the PM inner leaflet.

In GUVs supplemented with DPPS, we observed a homogeneous ring structure of eVP40-Alexa488 surrounding the GUV membrane (Expanded View Fig. 1a, *middle panel*) and the plot profile analysis indicates a small overlap of the two fluorescent signals at the GUV membrane (Expanded View Fig. 1c, indicated by the asterisk). However, the protein enrichment at the GUV membrane does not indicate a significant increase in the amount of Alexa488 fluorescence at the GUV membrane (enrichment index 1.4 ± 0.4, Expanded View Fig. 1e). These data indicate that the conjugated protein binds weakly to DPPS-containing GUVs. To investigate further the ability of eVP40-Alexa488 to bind an anionic membrane similar to the PM, similar analyses as above were performed on GUVs containing both DPPS and PI(4,5)P_2 (Expanded View Fig. 1a *right panel)*. The plot profile analysis of the image in Supplementary Fig. 1a revealed a strong overlap between the two fluorescence signals (eVP40 and TMR-PS) (Expanded View Fig. 1d). The protein enrichment analysis also supported this previous observation with an enrichment index of ~5.4 ± 2, four times more than membranes devoid of PI(4,5)P_2 (Expanded View Fig. 1e). These data are in agreement with the previously published findings that eVP40 requires both anionic lipids for efficient membrane binding and oligomerization and suggest eVP40 is able to enrich fluorescent PS at sites of VP40 oligomerization.

To expand upon our findings, we investigated if eVP40 localizes to PS enriched regions within living cells. PS can be exogenously added to media of cells and within

bioRxiv preprint doi: https://doi.org/10.1101/2021.06.08.447555; this version posted June 8, 2021. The copyright holder for this preprint (which was not certified by peer review) is the author/funder. All rights reserved. No reuse allowed without permission.

minutes it will be incorporated into the inner leaflet of the PM as a result of PS flippases, which are widely expressed in mammalian cells and rapidly translocate PS from the outer to the inner leaflet of the PM[42]. To visualize PS and protein localization simultaneously, we transiently expressed EGFP-fused proteins in HEK293 cells and supplemented the cells with TMR-PS immediately prior to imaging (Expanded View Fig. 2a). Plot profile analysis of the fluorescence intensities for both EGFP and TMR-PS was performed (Expanded View Fig. 2b-f). To first verify our experimental setup, monomeric EGFP or EGFP-LactC2 were expressed in HEK293 cells. Plot profile analysis comparing the EGFP vs. TMR-PS signals revealed almost no overlap of the fluorophores, as EGFP was primarily cytosolic (Expanded View Fig. 2a,b). Additionally, the plot profile analysis of the EGFP-LactC2 vs. TMR-PS signals showed strong overlap of these two fluorophores (Expanded View Fig. 2a,c). These results confirmed that TMR-PS was specifically localized to the PM and was detectable by a peripheral protein with PS specificity.

To test the hypothesis that eVP40 localizes to PS enriched regions of the PM, we next examined the plot profile analysis of TMR-PS and eVP40 by expressing functionally unique EGFP fused eVP40 proteins: WT-eVP40, K224A-eVP40 (a PS-binding residue mutant[31]), and WE/A-eVP40 (oligomerization deficient mutant[43]). The fluorescence profile of EGFP-WT-eVP40 vs. TMR-PS revealed a strong overlap between the two fluorophores (Expanded View Fig. 2a,d). This cellular data corroborates our *in vitro* data, demonstrating that EGFP-eVP40 localizes to PS enriched regions of both model membranes and in the PM of cells. Additionally, there was no significant fluorescence signal overlap between the EGFP-K224A-eVP40 mutant and TMR-PS (Expanded View Fig. 2a,e) which supports the requirement for PS binding for PM localization of eVP40[31].

bioRxiv preprint doi: https://doi.org/10.1101/2021.06.08.447555; this version posted June 8, 2021. The copyright holder for this preprint (which was not certified by peer review) is the author/funder. All rights reserved. No reuse allowed without permission.

Importantly, plot profile analysis revealed a moderate overlap in the fluorescence signals of the oligomerization deficient mutant WE/A-eVP40 and TMR-PS (Expanded View Fig. 2a,f). This is important to note as this protein is still able to interact with PS at the PM, however, is unable to properly oligomerize[43,44]. These results suggest that VP40 interacts with PS at the PM inner leaflet as a dimer without significant oligomerization, in line with VP40 *in vitro* lipid-binding[31].

EBOV-VP40 enhances clustering of PS in synthetic membranes and in living cells

The proper localization and function of numerous peripheral proteins are dependent on the presence of PS in the inner leaflet[45–47]. Biophysical and molecular studies into PS dynamics in both model membranes and in living cells revealed that PS basally distributes into clustered domains enriched with PS[15,27,28]. Interestingly, cellular proteins such as Annexins are known to significantly enhance the clustering of PS[48] and viral proteins such as M1 of Influenza A virus have a selectivity for these PS clusters[15]. However, detailed examination of PS clustering and whether filovirus matrix proteins such as eVP40 alter the organization of PS has not yet been explored.

To quantitatively investigate how eVP40 affects PS clustering *in vitro*, we investigated TMR-PS labelled PS:PI(4,5)P_2 GUVs incubated with eVP40-Alexa488 using confocal microscopy. Confocal 3D reconstruction of GUVs (with DPPS and PI(4,5)P_2) in the absence of protein indicates a homogeneous distribution of TMR-PS across the section of the GUV membrane (Fig. 1a; *left column*). However, after incubation with 1.25 μM of eVP40:eVP40-Alexa488 (9:1 ratio), different structures of TMR-PS clusters are clearly observed where eVP40-Alexa488 fluorescence is enriched (Fig. 1a, *three right*

bioRxiv preprint doi: https://doi.org/10.1101/2021.06.08.447555; this version posted June 8, 2021. The copyright holder for this preprint (which was not certified by peer review) is the author/funder. All rights reserved. No reuse allowed without permission.

columns). Furthermore, the Mander's coefficient index of correlation was quantified between the TMR-PS and eVP40-Alexa488 fluorescence signals of GUVs with varying lipid compositions (Fig. 1b). The index of correlation revealed no correlation between PS and eVP40 when anionic lipids were not abundant (DPPC:Chol:TMR-PS). Conversely, a notable increase in PS clustering was detected when eVP40-Alexa488 was incubated with DPPS GUVs (Fig. 1b; $p=0.0544$). Furthermore, a statistically significant increase in PS clustering was detected when eVP40-Alexa488 was incubated with GUVs containing both DPPS and $PI(4,5)P_2$ (Fig. 1b; $*p<0.0001$). These results suggest that eVP40 induces PS clustering *in vitro,* which is significantly enhanced in the presence of both PS and $PI(4,5)P_2$, akin to the lipid composition typically found in the PM inner leaflet.

Next, we were interested to determine if eVP40 was able to induce PS clustering in synthetic membranes in the absence of $PI(4,5)P_2$. Therefore, we performed a TMR self-quenching experiment as described previously[49,50]. The TMR fluorescent group has potent self-quenching properties when two molecules or more are brought to close distance from each other. Because of the low molar ratio of TMR-PS (0.2%) used in this assay, self-quenching is expected to be minimal in the absence of induced PS-clustering. We tested the ability of eVP40 to undergo TMR self-quenching when fluorescent PS was incorporated in lipid vesicles, as a secondary effect to eVP40-induced PS-clustering. We also tested different eVP40 concentrations and different PS ratios to investigate if TMR self-quenching was concentration dependent. The strongest TMR self-quenching in all membranes was observed at 1.5 μM eVP40 (Fig. 1c). As expected, higher PS molar ratios resulted in stronger eVP40 induction of TMR self-quenching except for a high molar ratio of DPPS (60% molar ratio). However, the addition of $PI(4,5)P_2$ at 2.5% molar ratio to 60%

bioRxiv preprint doi: https://doi.org/10.1101/2021.06.08.447555; this version posted June 8, 2021. The copyright holder for this preprint (which was not certified by peer review) is the author/funder. All rights reserved. No reuse allowed without permission.

DPPS-containing membranes rescued TMR self-quenching similarly to 40% DPPS-containing membranes. Further, DPPS-containing membranes at 60% molar ratio with or without PI(4,5)P_2 displayed a maximum of TMR-PS self-quenching at 2 μM eVP40. These observations may indicate a saturation of the liposome membranes with eVP40 at high PS concentrations. Altogether, this assay demonstrated that eVP40 is able to cluster PS, which is enhanced in the presence of PI(4,5)P_2.

We next examined if eVP40 enhanced PS clustering in the PM of living cells. We first expressed monomeric EGFP in HEK293 cells supplemented with TMR-PS and examined the ability of confocal microscopy to detect PS clusters (Fig. 1d *top panel,* Fig. 1e). As previously mentioned, PS selectively localizes into clustered regions[15,27,28]; therefore, a basal degree of PS clustering should be observed. We developed a custom ImageJ macro to perform a moments-based thresholding analysis to identify regions of the PM with enriched PS content (Expanded View Fig. 3a). From there, we quantified the total area of these identified clusters as a percentage of the entire PM area. Through this analysis we were able to detect a basal level of PS enriched clusters in our control GFP expressing cells, with PS clusters accounting for approximately ~8% of the PM (Fig. 1d *top panel* and Fig. 1e). Our method was further validated by expressing an additional control protein with a glycosylphosphatidylinositol membrane anchor conjugated to GFP (GFP-GPI) in HEK293 cells supplemented with TMR-PS, which revealed PS clusters in ~8% of the PM area (Fig. 1e; Representative image available in Expanded View Fig. 3b *top panel*).

We next sought to determine if our technique accurately captured enhanced PS clustering, therefore, we expressed EGFP-Annexin A2 in HEK293 cells. Annexin A2 has

bioRxiv preprint doi: https://doi.org/10.1101/2021.06.08.447555; this version posted June 8, 2021. The copyright holder for this preprint (which was not certified by peer review) is the author/funder. All rights reserved. No reuse allowed without permission.

been shown to enhance the clustering of PS in a calcium dependent manner[48]. Therefore, in EGFP-Annexin A2 expressing cells, supplementation with TMR-PS was preceded with supplementing the cellular media with 10 mM calcium and 5 μM of the calcium ionophore ionomycin. As shown in Fig. 1d&e, expression of EGFP-Annexin A2 in cells significantly enhanced PS clustering roughly 2-fold, compared to EGFP expressing cells (***p=0.0001). Taken together, these findings corroborate the previously reported effect of Annexin A2 on PS organization, as well as validate the method developed for our assay.

To further examine the selectivity of PS clustering for lipid-binding proteins that localize to the PM inner leaflet, we expressed EGFP-PLCδ-PH and EGFP-LactC2 in HEK293 cells supplemented with TMR-PS (Representative images available in Expanded View Fig. 3b, *middle & bottom panel*). EGFP-PLCδ-PH binds specifically to $PI(4,5)P_2$, another critical component of many virus assembly processes, including filoviral assembly[39]. Again, EGFP-LactC2 specifically and reversibly binds to PS. As expected, expression of neither EGFP-PLCδ-PH or EGFP-LactC2 significantly altered the extent of PS clustering (Fig. 1e). This confirms that transient expression of fluorescently conjugated lipid-binding proteins is not sufficient to enhance PS clustering at the PM.

Finally, we evaluated the effect of eVP40 expression on PS organization across the PM. We independently expressed three functionally distinct EGFP fused eVP40 constructs: WT-eVP40, K224A-eVP40, and WE/A-eVP40 and supplemented the cells with TMR-PS prior to imaging. Strikingly, expression of EGFP-WT-eVP40 increased PS clustering by ~2 fold (*p=0.004), similar to the PS clustering observed with Annexin A2 expression (Fig. 1d,e). However, expression of the PS-binding deficient mutant EGFP-

bioRxiv preprint doi: https://doi.org/10.1101/2021.06.08.447555; this version posted June 8, 2021. The copyright holder for this preprint (which was not certified by peer review) is the author/funder. All rights reserved. No reuse allowed without permission.

K224A-eVP40 showed no significant change in PS clustering (Fig. 1d,e), supporting the hypothesis that eVP40 must interact with PS to promote its clustering at the PM. Additionally, to investigate if eVP40 matrix oligomerization was important for PS clustering, we expressed EGFP-WE/A-eVP40 in HEK293 cells. It is important to note that this mutant still colocalizes with PS at the PM (Expanded View Fig. 2a,f) albeit to a lesser extent than WT[43]. Although the WE/A-eVP40 and PS interaction is maintained in cells, no significant increase in PS clustering was observed (Fig. 1d,e). To the best of our knowledge, this is the first account of a filovirus matrix protein modulating the organization of PS within the PM. Moreover, these results demonstrate that both membrane binding and oligomerization of eVP40 is central to eVP40-mediated PS clustering.

eVP40 membrane binding and oligomerization are dependent on phosphatidylserine content in lipid membranes

As eVP40 binds to PS through electrostatic and stereospecific interactions [14,31,37], we hypothesized eVP40 may require PS clustering for productive interactions at the PM during assembly. Enrichment of PS within regions of the PM would provide additional PS molecules available to recruit eVP40 to platforms of viral budding. To investigate how increasing the amount of PS within membranes dictates eVP40 membrane affinity, surface plasmon resonance (SPR) was performed with His_6-eVP40 and large unilamellar vesicles (LUVs) with increasing concentrations of PS (from 1% to 22 mol% PS; Fig. 2a-c). eVP40 displayed moderate binding to LUVs with 1% PS, with an apparent affinity of 2.5 μM (Fig. 2a). However, increasing the concentration of PS to 11% increased the apparent affinity of eVP40 to 0.65 μM (Fig. 2b). eVP40 displayed even

bioRxiv preprint doi: https://doi.org/10.1101/2021.06.08.447555; this version posted June 8, 2021. The copyright holder for this preprint (which was not certified by peer review) is the author/funder. All rights reserved. No reuse allowed without permission.

stronger affinity to vesicles with 22% PS, with an apparent affinity of ~0.18 μM (Fig. 2c). These results indicate that by increasing the amount of PS in membranes, the affinity of eVP40 to lipid membranes can be modulated. This finding supports the hypothesis that PS clustering may be a mechanism for the virus to provide the necessary electrostatic contacts needed for matrix assembly during viral production.

Once at the PM, VP40 oligomerizes into the extensive matrix that gives rise to the stability and structure of the virion. Previously, Adu-Gyamfi *et al.* (2015) highlighted the importance of PS in this process, where a cell line deficient in PS synthesis showed a significant reduction in eVP40 oligomerization at the PM. Moreover, our confocal clustering data (Fig. 1d,e) revealed that eVP40 oligomerization is crucial for modulating PS organization into clustered domains. To investigate how increasing PS concentration alters eVP40 oligomerization, we utilized chemical crosslinking of His_6-eVP40 which had been incubated with LUVs of increasing PS concentration (Fig. 2d,e). We found that when eVP40 is incubated with LUVs that contain 0% PS, no detectable higher order structures of eVP40 are found (Fig. 2d *lane 1,* Fig. 1e). However, by introducing 15% PS into LUVs, the extent of eVP40 oligomerization beyond dimeric eVP40 is significantly higher than when 0% PS LUVs are used (Fig. 2d *lane 2*, Fig. 1e). We next tested LUVs containing 30% and 60% PS and found that eVP40 oligomerization was even more significantly detected than when just 15% PS was used (Fig. 2d *lane 3 and lane 4, respectively*, Fig. 1e). Compared to LUVs with 0% PS, both 30% PS and 60% led to a significant increase in eVP40 oligomerization (*p=0.021 and *p=0.017, respectively). Further, eVP40 oligomerization appeared to saturate when 30% PS was included, as increasing PS content to 60% did not increase eVP40 oligomerization (compared to 30% PS). Taken

bioRxiv preprint doi: https://doi.org/10.1101/2021.06.08.447555; this version posted June 8, 2021. The copyright holder for this preprint (which was not certified by peer review) is the author/funder. All rights reserved. No reuse allowed without permission.

together, these studies suggest a dynamic relationship between PS clustering and eVP40 affinity and oligomerization as a critical step in eVP40 viral assembly.

Total cellular and plasma membrane levels of phosphatidylserine are reduced by fendiline treatment

A recent study reported an FDA-approved drug, fendiline, inhibited K-Ras PM localization and signaling[35] and reduced PM PS content in MDCK cells[33]. Therefore, it was our goal to determine if fendiline could also reduce PS levels in the human cell line HEK293, a cell line commonly used in BSL-2 filovirus studies, and subsequently inhibit virus spread. The initial finding that fendiline reduced PS levels within the PM (40% reduction, IC_{50} ~3uM) was conducted in MDCK cells using thin-layer chromatography[33], therefore it had not been established if this effect was cell-type specific. To address this, we first established fendiline's toxicity in HEK293 cells. After 24 and 48 hours of treatment, no significant toxicity was observed in treatments up to 5 μM fendiline (Expanded View Fig. 4a). Next, to evaluate the effect of fendiline on PS in HEK293 cells, cells were treated with fendiline for 48 hours, harvested, and lipids were extracted and quantified by liquid chromatography-tandem mass spectrometry (LC-MS/MS). We observed a significant reduction in cellular PS levels compared to DMSO treated cells, after 48 hour treatment with 1 μM fendiline (~18% reduction; *p=0.012) and 5 μM fendiline (~30% reduction; ***p=0.0003)(Fig. 3a). Fendiline exhibited no selectivity in reducing different PS species, as 5 μM fendiline reduced long chain (C>38) and saturated PS species nearly equally (Expanded View Fig. 4b). It is important to note that the effect of fendiline on PS was specific in that fendiline treatment had no significant effect on another anionic

bioRxiv preprint doi: https://doi.org/10.1101/2021.06.08.447555; this version posted June 8, 2021. The copyright holder for this preprint (which was not certified by peer review) is the author/funder. All rights reserved. No reuse allowed without permission.

phospholipid, phosphatidic acid (Expanded View Fig. 4c). Therefore, our data supports the reported finding that fendiline reduced total cellular levels of PS, and that the effect is not cell dependent.

As PS is an integral anionic component of the PM inner leaflet, we sought to confirm that fendiline treatment also reduced PS levels within the PM in HEK293 cells. PS localization within the PM has been readily studied by expressing EGFP-LactC2 in mammalian cells[42,51]. Therefore, HEK293 cells expressing EGFP-LactC2 were imaged at 24 hours (representative images in Expanded View Fig. 4d) and 48 hours (representative images in Fig. 3b) post-treatment with increasing concentrations of fendiline. Single doses of 500 nM fendiline had no effect on EGFP-LactC2 PM localization at 24 or 48 hours post treatment (Expanded View Fig. 4e and Fig. 3c, respectively). However, we found a ~30% reduction in PM EGFP-LactC2 localization after 24 hours of treatment for both 1 μM (**p=0.0003) and 5 μM fendiline (**p=0.0045) (Expanded View Fig. 1e). However, a single dose of 1 μM fendiline treatment did not significantly affect Lact-C2 PM localization after 48 hours of treatment (Fig. 3c). Conversely, a single dose of 5 μM fendiline significantly reduced Lact-C2 PM localization even at 48 hours post treatment (~30% reduction; **p=0.0031; Fig. 3c), a reduction similar to that observed at 24 hours post treatment. These finding corroborate Cho *et al.* (2015) where reduction of PS levels by fendiline at the PM were slow acting but could be sustained with 5 μM treatment after 48 hours[33] and were also consistent with our LC-MS/MS analysis (Fig. 3a).

Fendiline reduces PS clustering

bioRxiv preprint doi: https://doi.org/10.1101/2021.06.08.447555; this version posted June 8, 2021. The copyright holder for this preprint (which was not certified by peer review) is the author/funder. All rights reserved. No reuse allowed without permission.

Next, we hypothesized that reduced levels of PS within the PM would therefore reduce the degree of PS clustering. To determine if fendiline treatment reduced the degree of PS clustering, we utilized the Number & Brightness technique (N&B). N&B is a quantitative fluorescence microscopy technique that allows one to detect the aggregation state of proteins with pixel resolution in real time within living cells[52]. Previously, N&B was used to quantify PS clustering by analyzing the N&B profile of EGFP-LactC2[15]. To accurately capture PS clustering at the PM, imaging was performed at a focal plane near the cell surface. Importantly, HEK293 cells expressing monomeric EGFP were imaged and quantified to establish the experimental brightness value for a monomeric aggregation state (Expanded View Fig. 4f).

To evaluate PS clustering, HEK293 cells expressing EGFP-LactC2 were treated with the control or fendiline for 48 hours and the EGFP-LactC2 N&B profile was examined (Fig. 3d,e). Three different cluster bin sizes were examined, 1—5, 5-10 and >10. The average percentage of pixels in each bin was calculated and plotted (Fig. 3e). Within control-treated cells, significant aggregation of EGFP-LactC2 was observed, with 25% present in complexes of 5-10 LactC2 molecules and ~10% in complexes of >10 LactC2 molecules (Fig. 3d *top panel* and Fig. 3e). This corroborates previous work investigating PS clustering, which found EGFP-LactC2 clusters up to 15 molecules in size[15]. Treatment of cells with 1 μM fendiline led to no significant change in PS clustering (Fig. 3d *middle panel* and Fig. 3e) which was expected as 1 μM fendiline had no significant effect on EGFP-LactC2 PM localization at 48 hours (Fig. 3b,c). Strikingly, 5 μM fendiline treatment abolished the presence of EGFP-LactC2 complexes >10 molecules and significantly reduced the number of complexes of 5-10 LactC2 molecules large (from ~8%

bioRxiv preprint doi: https://doi.org/10.1101/2021.06.08.447555; this version posted June 8, 2021. The copyright holder for this preprint (which was not certified by peer review) is the author/funder. All rights reserved. No reuse allowed without permission.

in DMSO to ~0% in 5 μM fendiline; **p=0.0043) (Fig. 3d *bottom panel* and Fig. 3e). Moreover, there was a significant (~23%) increase in EGFP-LactC2 complexes of ~1-5 molecules in size in cells treated with 5 μM fendiline compared to control treated cells (****p<0.0001) (Fig. 3d *bottom panel* and Fig. 3e). Taken together, this data suggests that fendiline treatment disrupted large PS-dependent LactC2 complexes which was compensated by an increase in smaller PS-dependent complexes. Therefore, fendiline may possess antiviral properties by disassembling PS enriched regions that would otherwise have been used as platforms for viral assembly.

Fendiline significantly inhibits authentic EBOV and MARV replication

Recent studies have implicated PS as an essential component of the budding [14,43] and entry[22,23] of filovirus VLPs and authentic virions. To determine if the FDA-approved drug fendiline was able to inhibit authentic filovirus replication and spread, we first established the toxicity of fendiline in Vero E6 cells (Expanded View Fig. 5a) and then monitored the efficacy of fendiline at inhibiting EBOV and MARV replication in a BSL-4 setting. Vero E6 cells, an established model for BSL-4 filovirus studies[53], were used to examine filovirus replication 48, 72 and 96-hours post-infection at different multiplicity of infection (MOI). Several different dosing regimens were designed to account for the slow response of fendiline in lowering cellular PS levels. The toxicity of fendiline in Vero E6 cells was first established using treatment schedules that would directly mirror treatment schedules in the filovirus infection model. As can be seen in Expanded View Fig. 5a, minimal toxicity was observed compared to the vehicle (even at the highest treatment group of 20 μM). Therefore, we proceeded with the filovirus infection model using

bioRxiv preprint doi: https://doi.org/10.1101/2021.06.08.447555; this version posted June 8, 2021. The copyright holder for this preprint (which was not certified by peer review) is the author/funder. All rights reserved. No reuse allowed without permission.

treatments of fendiline up to 20 μM. Cell treatment groups included increasing concentrations of fendiline (2.5μM, 5 μM, 10 μM, and 20 μM) that were added to cell culture 24-hours prior to infection. An equivalent percent concentration of DMSO in culture media served as the vehicle control. Following removal of pretreatment compound, cells were then inoculated with either EBOV (Kikwit) or MARV (Ci67) at a multiplicity of infection MOI of 0.1 or 1.0, and incubated for 1 hour at 37C in 5% CO2, in a BSL-4 laboratory located at USAMRIID. Following infection, plates were separated into three post-infection treatment groups (day 0, every day dosing, or every other day dosing). In order to quantify viral replication, at 48 hours (MOI=1.0), 72 or 96 hours (MOI=0.1) post-infection, cells were washed and submerged in 10% neutral buffered formalin 24 hours prior to removal from the BSL-4 laboratory. Using virus specific antibodies to the glycoprotein (GP), cells were then imaged (Fig. 4a,e) and the percent of virus infected cells calculated using a high content imaging system (Fig. b-d, f-h).

Fendiline was most effective at reducing EBOV and MARV infection *in vitro* at the highest 20 μM concentrations in each treatment group with statistically significant inhibition observed for both EBOV and MARV at each time point and each treatment group (excluding EBOV 48 hours, e.d.)(****$p<0.0001$, **$p<0.0066$). Percent inhibition was directly affected by timing of treatments following infection. Furthermore, both EBOV and MARV treatment with fendiline e.d. had the highest inhibition on viral spread at each time point for 20 μM fendiline treatments. Cells of the e.o.d. treatments group, which did not receive treatment immediately following infection with virus, had a dramatically reduced degree of inhibition as compared to the day 0 and e.d. treatment groups, both of which received fendiline immediately following viral infection of one hour.

bioRxiv preprint doi: https://doi.org/10.1101/2021.06.08.447555; this version posted June 8, 2021. The copyright holder for this preprint (which was not certified by peer review) is the author/funder. All rights reserved. No reuse allowed without permission.

Fendiline reduced EBOV-VP40 but not MARV-VP40 localization to the plasma membrane

As both EBOV and MARV-VP40 assembly at the PM is in part governed by PS, we first analyzed both EGFP-eVP40 and EGFP-mVP40 PM localization in cells treated with fendiline for 24 or 48 hours. Treatment with 1 μM and 5μM fendiline had no significant effect on eVP40 PM at 24 hours post treatment (Expanded View Fig. 5b,c); therefore, EGFP-mVP40 PM localization was not assessed at 24 hours. Surprisingly, no significant change in EGFP-mVP40 PM localization was observed after 48 hours with either 1 μM or 5 μM fendiline treatment (Fig. 4a *bottom panel* and Fig. 4b); therefore, mVP40 was excluded from further experiments. In agreement with our results thus far, 1 μM fendiline did not significantly inhibit EGFP-eVP40 PM localization after 48 hours of treatment (Fig. 5a *top panel* and Fig.5 c). However, treatment with 5 μM fendiline for 48 hours led to a modest reduction in EGFP-eVP40 PM localization (~6% reduction compared to control treated cells; not significant as p=0.08) (Fig. 5a *top panel* and Fig. 5c). However, the reduction of eVP40 PM localization was not robust enough to lead to the observed inhibition of EBOV by fendiline treatment in our BSL-4 studies (Fig. 4). One possible explanation is that a limitation of this technique is the inability to differentiate the extent of VP40 oligomerization occurring using basic confocal microscopy. Therefore, it is possible that fendiline reduced PS levels within the PM, but not significantly enough to block VP40's ability to bind to the PM.

VP40 oligomerization is significantly reduced by fendiline treatment

bioRxiv preprint doi: https://doi.org/10.1101/2021.06.08.447555; this version posted June 8, 2021. The copyright holder for this preprint (which was not certified by peer review) is the author/funder. All rights reserved. No reuse allowed without permission.

PS is also a key factor promoting the self-assembly of VP40 into the matrix layer of the budding virion[14,43]. This self-assembly process has been highlighted in our *in vitro* crosslinking data (Fig. 2d,e) as well as previously reported in live cells utilizing the N&B technique[43]. To assess how fendiline impacted eVP40 oligomerization in cells, we examined the oligomerization profile of EGFP-eVP40 using the previously described N&B[39,43] (Fig. 5d,e). To accurately capture oligomerization at the PM, imaging was performed at a focal plane at the top of the cell. HEK293 cells expressing monomeric EGFP were imaged and quantified to calculate the experimental brightness value for a monomer (Expanded View Fig. 4f). The crystal structure and biochemical analysis of eVP40 suggests eVP40 binds to the PM as a dimer, subsequently oligomerizes into larger oligomers such as a hexamer, and these hexamers are building blocks for extensive filamentous formation [11]. Therefore, for our data to coincide with the current models of eVP40 oligomerization, EGFP-eVP40 oligomers were grouped into bins based on multiples of the hexamer (i.e. monomer-hexamer, hexamer-12mer, 12mer-18mer, and >18mer). The average percentage of pixels in each bin was calculated and plotted for HEK293 cells expressing EGFP-eVP40 and treated with either the control or indicated concentration of fendiline for 48 hrs (Fig. 5e).

Large eVP40 oligomeric structures corresponding to each bin size were readily detectable at the PM in control treated cells (Fig. 5d *top panel* and Fig. 5e), with ~72% of eVP40 found as a monomer-hexamer, ~16% as a hexamer-12mer, ~8% as a 12mer-18mer, and 3% in complexes >18mer. Treatment with 1 μM fendiline led to a ~8% increase in monomeric-hexameric eVP40, and small decreases in the larger oligomeric structures, although no changes were statistically significant (Fig. 5d *middle panel* and

bioRxiv preprint doi: https://doi.org/10.1101/2021.06.08.447555; this version posted June 8, 2021. The copyright holder for this preprint (which was not certified by peer review) is the author/funder. All rights reserved. No reuse allowed without permission.

Fig. 5e). However, the oligomeric profile of eVP40 was statistically different when cells were treated with 5 μM fendiline. Following 5 μM fendiline treatment, there was a significant increase in eVP40 found in the monomeric-hexameric state (~13% increase; **p=0.0035) which was counterbalanced by an equal reduction in the larger oligomeric states (~6% reduction for hexamer-12mer, 5% reduction for 12mer-18mer, and ~3% reduction for eVP40 structures >18mer) (Fig. 5d *bottom panel* and Fig. 5e). These results support our hypothesis that by reducing PS concentration and therefore the pool of PS available for clustering, eVP40 is unable to properly oligomerize once it traffics and binds to the PM. This, in combination with the modest reduction in eVP40 PM binding following fendiline treatment, may therefore impact the production of viral particles as suggested from our BSL-4 studies.

Fendiline reduced VLP production at the plasma membrane

As fendiline reduced VP40 oligomerization, we sought to determine the effect of fendiline treatment on VLP production using functional budding assays. VLPs were harvested at 24 (Fig. 6a,b) and 48 hours (Fig. 6c,d) post-treatment and the relative budding index was determined with western blotting and densitometry analysis. No significant effect on VLP production was observed for cells treated with 0.5 μM or 1 μM fendiline at either 24 (Fig. 6a *lane 3,4* and Fig. 6b) or 48 hours post-treatment (Fig. 6c *lanes 3,4* and Fig. 6d). However, treatment with one dose of 5 μM fendiline for 24 hours led to a ~25% reduction in VLP production (Fig. 6a *lane 5* and Fig. 6b) compared to DMSO treated cells (Fig. 6a *lane 2* and Fig. 6b). More importantly, this reduction in VLP production was even more robust when monitored at 48 hours post-treatment, with a

bioRxiv preprint doi: https://doi.org/10.1101/2021.06.08.447555; this version posted June 8, 2021. The copyright holder for this preprint (which was not certified by peer review) is the author/funder. All rights reserved. No reuse allowed without permission.

statistically significant ~60% reduction in the relative budding efficiency of 5 μM fendiline treated cells (*p-0.0260) (Fig. 6c *lane 5* and Fig. 6d) compared to DMSO treated cells (Fig. 6c *lane 2* and Fig. 6d). The reduction in VLPs is supported by our previous findings that a single dose of 5 μM fendiline reduced PS levels, PS clustering and the extent of eVP40 oligomerization at the PM. Therefore, we hypothesize that reduced virus budding is at least partially responsible for fendiline efficacy in authentic EBOV studies (Fig. 4).

To further investigate the reduction of VLP production in fendiline treated cells, and to determine if there were any observable morphological changes in VLPs, scanning electron microscopy (SEM) experiments were performed on mock transfected cells (Fig. 6e) and cells expressing FLAG-eVP40 (Fig. 6f). Cells were treated with either the control, 1 μM or 5 μM fendiline for 48 hours. SEM revealed the presence of filamentous protrusions from the PM of mock transfected cells in untreated and control treated cells (Fig. 6e). In both control and fendiline treated cells expressing FLAG-eVP40, a dense filamentous protrusion population was observed at the surface of cells, indicating abundant VLP production (Fig. 6f). This extensive budding of VLPs was present in untreated, DMSO treated, and 1 μM fendiline treated cells expressing FLAG-eVP40 (Fig. 6f). Importantly, micrographs of cells expressing FLAG-eVP40 and treated with 5 μM fendiline revealed minimal VLP production at the PM compared to control treated cells (Fig. 6f). These findings support the hypothesis that fendiline treatment considerably reduces the production of VLPs in eVP40 expressing cells.

VLP morphology is altered by fendiline treatment

bioRxiv preprint doi: https://doi.org/10.1101/2021.06.08.447555; this version posted June 8, 2021. The copyright holder for this preprint (which was not certified by peer review) is the author/funder. All rights reserved. No reuse allowed without permission.

The structure and stability of filoviruses is derived from the VP40 matrix underlying the lipid envelope of virions. Therefore, we utilized transmission electron microscopy (TEM) of purified VLPs to determine if disturbing matrix assembly and altering the lipid components of the PM with fendiline treatment changed VLP morphology and possibly infectivity (Fig. 7a-c). During filoviral entry, surface exposed GP and viral envelope PS interact with the receptor T-cell immunoglobulin receptor-1[18,22] (TIM-1). To recapitulate entry-competent VLPs (eVLPs), we co-expressed eVP40 with the Ebola virus glycoprotein (eGP). We performed TEM of eVLPs purified from control and 5 μM fendiline treated cells (48-hour treatment) and used ImageJ software to analyze VLP length and diameter (Fig. 7a-c). Control eVLPs were heterogenous in length with a mean length of 4.1 μm ± 2.9 (Fig. 7a *left panel* and Fig. 7b). Control eVLPs diameter also exhibited a level of heterogeneity but had a fairly consistent diameter of 75 nm ± 12.9, which is similar to previous studies of both virions and VLPs[2,7] (Fig. 7a *left panel* and Fig. 7c). The length and diameter of eVLPs derived from 5 μM fendiline treated cells were significantly less than control eVLPs. Strikingly, fendiline treatment reduced eVLP length by ~35%, from 4.1 μm to 2.7 μm (*p=0.0139) (Fig. 7a *right panel* and Fig. 7b) and modestly but statistically significantly reduced eVLP diameter (*p=0.043) (Fig. 7a *right panel* and Fig. 7c). To ensure that eVLPs derived from fendiline treated cells were not more susceptible to damage during the purification, circular dichroism thermal melting was performed and no difference in eVLP stability was observed (Expanded View Fig. 6). Reduced eVLP length and diameter could translate into reduced infectivity (e.g., less PS and less surface area and membrane available to bind TIM-1), therefore we next sought to determine the effect of fendiline on eVLP entry.

bioRxiv preprint doi: https://doi.org/10.1101/2021.06.08.447555; this version posted June 8, 2021. The copyright holder for this preprint (which was not certified by peer review) is the author/funder. All rights reserved. No reuse allowed without permission.

527

528 **Fendiline blocks EBOV eVLP entry**

529 A common characteristic of viral infectivity is the relationship between virion
530 associated PS and the TIM-1 receptor on target cells[18,22,23,54,55]. Moreover, it has
531 been previously reported that other ASM inhibitors blocked EBOV infectivity[56]. To
532 determine if fendiline treatment reduced the entry of eVLPs, we performed a fluorescent
533 based entry assay using 1,1'-dioctadecyl-3,3,3',3'-tetramethylindocarbocyanine
534 perchlorate (DiI) labelled eVLPs[20,57,58]. DiI labelled eVLPs were derived from cells
535 treated with either control or 5 μM fendiline. By testing entry of eVLPs derived from
536 fendiline treated cells rather than the entry of eVLPs on fendiline treated cells, we were
537 able to determine how fendiline treatment affected eVLP entry rather than how inhibition
538 of ASM in target cells affected eVLP entry (as previously described[56]). In brief, eVLPs
539 derived from both control and fendiline treated cells were purified and labelled with DiI,
540 incubated with target cells overexpressing increasing amounts of TIM-1, and the DiI signal
541 was imaged using confocal microscopy (Representative images in Fig. 7d). If entry of the
542 eVLPs was not altered by fendiline treatment, one would expect a dose-dependent
543 increase in infectivity with increasing TIM-1 expression. Conversely, if eVLP entry was
544 inhibited by fendiline treatment, a dose-dependent increase in eVLP entry would not be
545 observed with increasing TIM-1 expression.

546 For all VLPs, non-specific entry was observed for target cells lacking TIM-1
547 overexpression (~1.7-1.9 DiI/infected cell, Fig. 7d *left panel* and Fig. 7e). This was not
548 unexpected, as normal endocytic processes were not inhibited in these experimental
549 conditions. However, as TIM-1 overexpression increased in target cells, a detectable and

bioRxiv preprint doi: https://doi.org/10.1101/2021.06.08.447555; this version posted June 8, 2021. The copyright holder for this preprint (which was not certified by peer review) is the author/funder. All rights reserved. No reuse allowed without permission.

significant dose-dependent increase in control eVLP entry was observed, by more than 200% in the highest TIM-1 overexpressing cells (compared to no TIM-1 overexpression; Fig. 7d *top panel* and Fig. 7e). Remarkably, no measurable increase in eVLP entry was observed for fendiline derived-VLPs across any of the TIM-1 overexpressing target cell conditions (Fig. 7d *bottom panel* and 7e). From this comparison, these results suggest that the impaired entry of fendiline eVLPs is a result of reduced PS in the viral envelope, either from smaller VLPs or a lower % of PS content. These findings in combination with the observed reduction in VLP formation further substantiate the significant reduction of EBOV infection observed in our live virus studies following fendiline treatment.

Mathematical model of *in vitro* experiments

We next used a mathematical model to predict how the effects of fendiline on both viral budding and entry combine to produce the observed effects in the BSL-4 assays. We calibrate our mathematical model (equations 1-3) to experimental data from the budding, entry and cellular infection assays using approaches and parameter settings outlined in the methods and Table 1. Results from our two-phase calibration procedure are shown in fig. 8a-f and Expanded View fig. 7. The model captures key features of the data including a progressive increase in percentage of infected cells over time, differences between MOI as well as limited cell death in the first 48 hours of the experiment (Expanded View Fig. 7).

The dynamics behind these calibrated figures suggested that fendiline treatment significantly delayed the infection process (Fig. 8g,h), resulting in the observed decrease in percent infected cells with treatment over 4 days. The effects of fendiline on budding

bioRxiv preprint doi: https://doi.org/10.1101/2021.06.08.447555; this version posted June 8, 2021. The copyright holder for this preprint (which was not certified by peer review) is the author/funder. All rights reserved. No reuse allowed without permission.

and entry are estimated to have similar pharmacodynamics (PD), with entry effects estimated to have a slightly stronger response (lower C_{50} and higher E_{max}) compared to budding (Table 1). Based on PD parameters, the response to fendiline was estimated to be weaker in the BSL-4 assays, as is evident by higher C_{50} values and lower E_{max} values compared to the budding and entry assays (Table 1, Fig. 8i). These PD parameter differences between budding and entry assays vs BSL-4 results could suggest that other parts of the viral life cycle not affected by fendiline (not quantified explicitly in these experiments) become rate limiting in the BSL-4 assays, thereby reducing the overall effect of fendiline on infection progression. In summary, a mathematical model consistent with three independent experimental systems, predicts a combination of budding and entry effects resulting in the observed BSL-4 effects, and estimates PD parameters for each mechanism.

Discussion

The host cell PM is exploited by filoviruses for their assembly and budding, where they can egress the host cell to form a new virion. The matrix protein, VP40, is the main driver of this process as it harbors a high affinity for lipids in the PM inner leaflet. Lipid binding by VP40, which includes selectivity for PS[14,31,37,38] and PI(4,5)P_2[39] drives and stabilizes, respectively, VP40 oligomers that are necessary for viral budding. In fact, VP40 has been shown to be sufficient (in the absence of other filovirus proteins) to form VLPs from the host cell PM that are nearly indistinguishable from virions[6–8]. Again, this underscores the unique properties of VP40 structure and sequence, which provides a template for host lipid binding, oligomerization, and sufficient information to encode cues

bioRxiv preprint doi: https://doi.org/10.1101/2021.06.08.447555; this version posted June 8, 2021. The copyright holder for this preprint (which was not certified by peer review) is the author/funder. All rights reserved. No reuse allowed without permission.

596 for scission to complete the viral budding process. Further, VP40 derived VLPs enter cells
597 in a PS-dependent manner despite the absence of the EBOV glycoprotein[19]. While
598 some of the basic principles between VP40 and PM interactions have been previously
599 revealed, the mechanistic consequences of the interactions and their potential
600 pharmacological targeting have remained unknown.

601 In this study, we demonstrated that VP40 was able to cluster PS *in vitro* and in the
602 PM of cells. VP40-dependent PS clustering required PS binding and efficient PM
603 localization of VP40, as the K224A-VP40 mutant, previously defined as a PS-binding
604 residue did not significantly increase PS clustering. VP40 oligomerization was also crucial
605 to PS clustering efficiency as a VP40 oligomerization deficient mutant, which can still
606 exhibit PM localization, significantly reduced PS clustering. This is an important point as
607 the PM of host cells is generally thought to harbor 20-30 mol% PS in the inner leaflet. In
608 fact, VP40 effectively binds and oligomerizes on PS-containing membranes with
609 compositions close to the PS-content of the PM inner leaflet. In contrast, PS
610 concentrations below 15 mol% didn't provide robust affinity and oligomerization compared
611 to those with 22 mol% PS and greater. PS clustering and PS content may also play a
612 critical role in the loss of asymmetry that occurs during the EBOV budding process. For
613 instance, pooling of PS in distinct regions of VP40 assembly may provide a cue for
614 scramblases shown to distribute PS to the outer leaflet of the PM during the viral budding
615 process[57,59].

616 A recent study demonstrated that silencing PSS1, an enzyme responsible for PS
617 synthesis in mammalian cells was sufficient to inhibit EBOV replication[59]. However, to
618 the best of our knowledge, small molecules aimed at targeting host cell lipid distribution

bioRxiv preprint doi: https://doi.org/10.1101/2021.06.08.447555; this version posted June 8, 2021. The copyright holder for this preprint (which was not certified by peer review) is the author/funder. All rights reserved. No reuse allowed without permission.

have not previously been tested against EBOV. Fendiline was a logical choice to form an initial hypothesis of an FDA-approved drug that could inhibit EBOV budding as it was recently shown to lower PM PS[33] and inhibit K-Ras signaling[34,35] suggesting this FDA-approved drug may be sufficient to inhibit EBOV budding. Indeed, in BSL-4 experiments, fendiline was able to inhibit EBOV replication >75% at 20 μM and MARV replication >90% when given every day post-infection. Follow up mechanistic studies demonstrated that fendiline efficacy was due to inhibition of VP40 oligomerization, viral budding and viral entry. Thus, fendiline, which reduced the PS content of HEK293 cells by ~30%, subsequently reduced PS clustering and VP40 oligomerization necessary for efficient viral budding. VLPs that did form from fendiline-treated cells had an overall reduced length and surface area, which likely combined with the reduced PS-content of the virus or VLPs to limit subsequent viral entry. Thus, disruption of PM PS content by one small molecule was sufficient to effect at least three important steps in the filovirus life cycle.

Overall, this study lends credence to the hypothesis that host processes may be targeted to inhibit viral replication and spread. While the potency of fendiline may be low, the combination of fendiline with other FDA-approved drugs that have shown efficacy against EBOV[60–64] hold further promise. These studies also lay a framework to improved pharmacological targeting strategies against either VP40 matrix assembly or PS clustering that would not only reduce viral budding and spread, but lower subsequent viral entry, which partially relies on PS in the viral envelope[18,19,22,32]. Notwithstanding pharmacological principles learned from this study, a critical balance between VP40 and PS has been resolved demonstrating a critical need for VP40 clustering in the assembly

bioRxiv preprint doi: https://doi.org/10.1101/2021.06.08.447555; this version posted June 8, 2021. The copyright holder for this preprint (which was not certified by peer review) is the author/funder. All rights reserved. No reuse allowed without permission.

642 and budding process. VP40 oligomers are needed for enhanced PS clustering where PS
643 clustering seems to ensure optimal VP40 oligomerization.
644

645 Methods

646 Reagents & solutions

647 PBS, DMEM, ionomycin and Lipofectamine LTX + Plus were purchased from
648 Fisher Scientific, heat-inactivated fetal bovine serum (FBS) was purchased from Hyclone,
649 and Minimum Essential Medium (MEM) was purchased from Corning. Invitrogen Live Cell
650 Imaging Solution, DiI Stain, Halt Protease inhibitor cocktail, Pierce BCA Assay kit, and
651 BS3 were purchased from ThermoFisher Scientific. Non-essential amino acids (NEAA)
652 were purchased from Sigma Aldrich and L-glutamine was purchased from Gibco. Alexa
653 Fluor™ 488 C_5 Maleimide (Alexa-488) for protein conjugation was purchased from
654 Invitrogen. Fendiline was purchased from Cayman Chemical, prepared in DMSO and
655 stored at -20 °C. Ultra-Pure Grade DMSO was purchased from VWR and the Ni-NTA
656 slurry was purchased from Qiagen. L1 chips for SPR experiments were purchased from
657 GE Healthcare. For cell viability assays, CellTiter-Glo® was purchased from Promega.
658 Antibody information for immunoblotting and immunofluorescence can be found in Table
659 1. Ten percent neutral buffered formalin was purchased from Val Tech Diagnostics
660 (Brackenridge, PA). Cell staining buffer was purchased from BioLegend. Invitrogen™
661 Molecular Probes™ Hoechst 3342 stain was purchased from Fisher Scientific.
662

663 Plasmids

bioRxiv preprint doi: https://doi.org/10.1101/2021.06.08.447555; this version posted June 8, 2021. The copyright holder for this preprint (which was not certified by peer review) is the author/funder. All rights reserved. No reuse allowed without permission.

EGFP, EGFP-eVP40 and EGFP-WE/A-eVP40 were prepared as described previously[39,43]. GFP-K224A-eVP40 was prepared by site directed mutagenesis[40] GFP-mVP40 was used as described previously[10,16]. The GFP-LactC2 plasmid was a kind gift from Sergio Grinstein (University of Toronto). GFP-PLCδPH was a kind gift from Tamas Balla (NIH). pCAG-GPI-GFP was a gift from Anna Katerina Hadjantonakis (Addgene #32601). pEGFP-N3-Annexin A2 was a gift from Volker Gerke & Ursula Rescher (Addgene #10796). pCAGGS-FLAG-eVP40 (NR49337) and pcDNA3.1-eGP (NR-19814) were obtained from BEI Services. pCAGGS-TIM-1 was from Heinz Feldmann[65].

Lipids and LUV preparation

All lipids were purchased from Avanti Polar Lipids, Inc. (Alabaster, AL) and stored in chloroform and/or methanol at -20°C until use. POPC (#850457), DPPC (#850355), Chol (#700000), DPPS (#840037), POPE (#850757), POPS (#840034), Brain PI(4,5)P_2 (#840046) and TopFluor® TMR-PS (#810242). For large unilamellar vesicle (LUV) preparation used in SPR and chemical crosslinking experiments, lipid mixtures were prepared at the indicated compositions, dried down to lipid films under a continuous stream of N_2, and stored at -20°C until further use. On each day of experiments, LUVs were brought to room temperature, hydrated in either SPR buffer (10 mM HEPES, 150 mM NaCl, pH 7.4) or chemical crosslinking buffer (260 μM Raffinose pentahydrate in PBS, pH 7.4), vortexed vigorously, and extruded through a 100 nm (SPR experiments) or 200 nm (chemical crosslinking experiments) filter. Vesicle size was confirmed by dynamic light scattering using a DelsaNano S Particle Analyzer (Beckman Coulter, Brea, CA).

bioRxiv preprint doi: https://doi.org/10.1101/2021.06.08.447555; this version posted June 8, 2021. The copyright holder for this preprint (which was not certified by peer review) is the author/funder. All rights reserved. No reuse allowed without permission.

Preparation and imaging of GUVs

GUVs were prepared by a gentle hydration method.[66–68] Briefly, 1 mM of lipid control mixture was made and contained 1,2-dipalmitoyl-sn-glycero-3-phosphocholine (DPPC), cholesterol (Chol) and fluorescent phosphatidylserine (TopFluor® TMR-PS) at 90:9.8:0.2% molar ratio. For PS clustering and eVP40 binding analysis, 1,2-dipalmitoyl-sn-glycero-3-phosphoserine (DPPS) alone or with brain phosphatidylinositol 4,5-bisphosphate PI(4,5)P_2 were added at 40 and 2.5% molar ratios, respectively, and the ratios of DPPC were adjusted accordingly. The lipid mixtures were prepared in 5 mL round-bottom glass flasks and the chloroform was removed with rotary movements under a continuous stream of N_2. The lipid films were then hydrated over night at 50°C (DPPC:Chol:TopFluor TMR-PS) and 55°C (DPPC:Chol:DPPS:PI(4.5)P_2:TopFluor TMR-PS) in an appropriate volume of GUV hydration buffer (150 mM NaCl, 10 mM HEPES, 0.5 M sucrose, pH 7.4).

For imaging, the freshly hydrated GUVs were diluted 10 times in GUV dilution buffer (150 mM NaCl, 10 mM HEPES, 0.5 M glucose, pH 7.4) and placed on a 6-mm diameter chamber made from a silicon sheet using a core sampling tool (EMS # 69039-60). The silicon chamber was mounted on a 1.5-mm clean coverglass (EMS # 72200-31) pre-coated with 1 mg/mL BSA. The set up was then assembled in an Attofluor chamber (Invitrogen # A7816) and 1.25 μM eVP40-Alexa488 was added. GUVs imaged for eVP40 and PS colocalization and clustering analysis was performed at 37°C on a Nikon Eclipse Ti Confocal inverted microscope (Nikon Instruments, Japan), using a Plan Apochromat 60x 1.4 numerical aperture oil objective and a 100x 1.45 numerical aperture oil objective,

bioRxiv preprint doi: https://doi.org/10.1101/2021.06.08.447555; this version posted June 8, 2021. The copyright holder for this preprint (which was not certified by peer review) is the author/funder. All rights reserved. No reuse allowed without permission.

respectively. A 488 nm argon laser was used to excite GFP and a 561 nm argon laser was used to excite TopFluor®-TMR-PS. The 3D reconstruction was performed using ImageJ. Mander's correlational analysis was performed using the plugin JACoP.[69]

Cell culture, transfections, pharmacological treatments

All BSL-2 studies were performed using HEK293 cells obtained from the American Type Culture Collection and cultured in DMEM supplemented with 10% FBS and 1% PS. Transient transfections were performed using Lipofectamine LTX + PLUS, according to the manufacturer's protocol. All transfections were performed in DMEM supplemented with 10% FBS. Treatment with fendiline (in DMSO) occurred at 5-hours post-transfection in DMEM supplemented with 10% FBS. BSL-4 assays were also performed using Vero E6 cells cultured in MEM, 5% heat-inactivated fetal bovine serum, 1% L-glutamine, and 1% NEAA. Both HEK293 and Vero E6 cells were cultured and incubated at 37°C, 5% CO_2, 80% humidity.

Immunoblotting

Samples prepared for western blotting analysis were first separated using SDS-PAGE (8% for chemical crosslinking and 12% for cell lysates and VLPs). Following transfer onto a nitrocellulose membrane, membranes were blocked with 5% MILK-TBST and analyzed with their respective antibodies (See Supplement Table 1). Antibodies were detecting using an ECL detection reagent and imaged on the ImageQuant LAS 4000 or Amersham Imager 600 (GE Healthcare Life Sciences). All quantitative analysis derived from western blotting was performed using densitometry analysis in ImageJ.

bioRxiv preprint doi: https://doi.org/10.1101/2021.06.08.447555; this version posted June 8, 2021. The copyright holder for this preprint (which was not certified by peer review) is the author/funder. All rights reserved. No reuse allowed without permission.

Protein purification and Alexa-488 C_5 Maleimide labelling

The His_6-eVP40-pET46 expression vector was a kind gift from Erica Ollmann Saphire (La Jolla Institute for Immunology) and was expressed and grown in Rosetta2 BL21DE3 cells (Merck Millipore, Billerica MA). The pet28a-His_6-Lact C2 bacterial expression plasmid was a kind gift from Dr. Sergio Grinstein. His_6-eVP40 and His_6-LactC2 were grown and purified as described previously[39]. Following elution from a Ni-NTA slurry (Qiagen), the protein samples were then further purified using size exclusion chromatography on a HiLoad 16/600 Superdex 200 pg column (ÄKTA pure, GE Healthcare). The desired fractions containing dimeric VP40 or monomeric LactC2 were collected, concentrated and stored in 10 mM Tris, 300 mM NaCl, pH 8.0. Protein concentration was calculated using the Pierce BCA assay and the protein was stored at 4°C for no longer than 14 days.

Labeling of eVP40 cysteine residues was carried out using Alexa-488- C_5-maleimide. eVP40 dimer was treated with a 1.5-fold molar excess of Alexa-488-C5-maleimide dissolved in DMSO for 2 hours at room temperature in maleimide labelling buffer (20 mM NaPi solution pH 7.4, 150 mM NaCl, 4 M Guanidine HCl). The labeling reaction was quenched by adding diothiothreitol (final concentration of 50 mM) and the labeled protein was separated from the non-conjugated dye on a HiLoad 16/600 Superdex 200pg column. Fractions containing eVP40 dimeric form were collected and concentrated. The labelling efficiency and protein concentration were estimated using a NanoDrop according to Invitrogen's instructions.

bioRxiv preprint doi: https://doi.org/10.1101/2021.06.08.447555; this version posted June 8, 2021. The copyright holder for this preprint (which was not certified by peer review) is the author/funder. All rights reserved. No reuse allowed without permission.

Plasma membrane localization confocal microscopy

Live cell imaging experiments were performed at 24 hours and 48 hours post treatment. Experiments to quantify fluorescent protein PM localization were performed on a Zeiss LSM 710 inverted microscope using a Plan Apochromat 63x 1.4 numerical aperture oil objective. A 488 nm argon laser was used to excite GFP/EGFP. GFP-LactC2 PM localization was quantified ratiometrically by comparing the PM signal vs. the cytosolic signal. GFP-EBOV-VP40 and GFP-MARV-VP40 PM localization was quantified ratiometrically by comparing the PM signal vs. the total fluorescence signal within the cell.

TMR-PS quenching experiment

The Top Fluor TMR quenching analysis was performed as described previously[50]. Briefly, LUVs with 0.5% TopFluor® TMR-PS and increasing amounts of DPPS (0, 1, 5, 10, 20, 40, 60%) with or without PI(4.5)P_2 (2.5% with 60% DPPS) were made as described above. LUVs were then mixed at a final concentration of 40 μM with corresponding concentrations of eVP40 dimer in 10 mM HEPES, 160 mM NaCl pH 7.4 in a black/clear bottom 96-well plate and incubated at 37°C for 30 min. The Top Fluor TMR was excited at 547 nm and the fluorescence was recorded from 555 to 600 nm with no cutoff wavelength using the plate reader SpectraMax M5e (Molecular Devices, St Jose, CA). The fluorescence quenching ratio, ΔF, was calculated according to the ratio (F_0/F), where F_0 is the fluorescence in absence of protein and F is the fluorescence at a given eVP40 concentration.

Cellular Top Fluor TMR-PS clustering confocal microscopy

bioRxiv preprint doi: https://doi.org/10.1101/2021.06.08.447555; this version posted June 8, 2021. The copyright holder for this preprint (which was not certified by peer review) is the author/funder. All rights reserved. No reuse allowed without permission.

Each experimental day, a 100 μM working stock of TopFluor® TMR-PS in methanol was prepared. Immediately prior to imaging, cells were placed in 4°C for 5 min. The working stock was diluted to a final 500 nM TopFluor® TMR-PS solution in 3 mg/mL BSA/PBS. The 500 nM TopFluor® TMR-PS/BSA/PBS solution was incubated with cells at 4°C for 10 min, rinsed three times with cold PBS, and immediately imaged in fresh cold PBS. Top Fluor TMR was excited at 560 nm and GFP was excited at 488 nm. For PS clustering analysis, a custom macro in ImageJ was used. Prior to the macro analysis background was subtracted, and the contrast was enhanced. To isolate the PM area, a default threshold was applied. To isolate PS clusters the Moments analysis thresholding[70] was applied. Following the moments analysis thresholding, the custom ImageJ macro was applied: despeckle, close-, fill holes, and remove outliers (radius=5, threshold=50). The sum of the remaining particles area was calculated, as well as the PM area. %PS clustering was calculated according to the ratio ($Area_{clusters}/Area_{plasma\ membrane}$).

Number & Brightness

Number & Brightness experiments were performed as described previously[15,39,43] on a Zeiss LSM 880 upright microscope using a LD “C-Apochromat” 40x/1.1 W Corr M27 objective. HEK293 cells expressing either GFP, GFP-LactC2 or GFP-eVP40 were treated with fendiline (1 or 5 μM) for 48-hours prior to N&B analysis. Cells were imaged in phenol-free live cell imaging solution. For each experimental day, the brightness value of a monomer was determined in cells expressing monomeric GFP. Each image was acquired using the same laser power (0.01), resolution (256x256), pixel dwell time (16 us), frames (50), and zoom (pixel size of 50 nm). SimFCS Globals Software

bioRxiv preprint doi: https://doi.org/10.1101/2021.06.08.447555; this version posted June 8, 2021. The copyright holder for this preprint (which was not certified by peer review) is the author/funder. All rights reserved. No reuse allowed without permission.

(Laboratory for Fluorescence Dynamics, University of California, Irvine, CA) was used for analysis.

Chemical crosslinking

His_6-eVP40 and His_6-LactC2 were purified as previously described in *Protein Purification*. LUVs containing POPC and Brain $PI(4,5)P_2$ (2.5%) with varying PS mol% composition (0, 15,30, 60%) were prepared as previously described in *Lipids & Vesicle Preparation*. Experimental protocol was adapted from Johnson K.A. *et al* 2016, and the manufacturers protocol for BS^3 (ThermoFisher) with each step performed at RT. In brief, protein (final concentration of 0.3 μM in PBS pH 7.4) was mixed with LUVs (final concentration = 660 μM) at a 1:1 volumetric ratio for 30 min. Protein bound LUVs were separated from unbound protein through centrifugation (75,000 x *g*, 30 min, 22°C), and resuspended in PBS (pH 7.4) buffer containing BS^3 (final concentration- 200 μM). Samples were incubated for 45 min, quenched with glycine for 15 min and then analyzed through western blotting. Following immunoblotting, oligomerization of VP40 was quantified ratiometrically by comparing $VP40_o$ vs. $VP40_{m+d}$ (where $VP40_o$ is the oligomeric VP40 band density (>75 kDa) and $VP40_{m+d}$ is the sum of monomeric and dimeric eVP40 (~37 and 74 kDa) band density).

Surface plasmon resonance

To determine the affinity of 6xHis-eVP40 to LUVs with increasing PS concentrations, SPR was performed. SPR experiments were performed at 25°C using a Biacore X100 as described previously.[14] In brief, an L1 chip was coated at 5 μL/min

bioRxiv preprint doi: https://doi.org/10.1101/2021.06.08.447555; this version posted June 8, 2021. The copyright holder for this preprint (which was not certified by peer review) is the author/funder. All rights reserved. No reuse allowed without permission.

with LUVs containing 0% PS on flow cell 1 and either 1%, 11% or 22 mol% POPS on flow cell 2 (LUV preparation described in previous section, *Lipids and Vesicle Preparation)*. The LUV conjugated chip was stabilized by washing with 50 mM NaOH and blocked with 0.1 mg/mL BSA (in SPR buffer) at a flow rate of 10 µL/min until the response on each flow cell was <100 response units (RU). For quantitative affinity analysis, each concentration of eVP40 was injected for 540 s at a flow rate of 10 µL/min with a 180 s delay, and the difference in response between flow cell 1 and flow cell 2 was recorded (ΔRU). The apparent K_d of vesicle binding was determined using the non-linear least squares analysis: $Req = Rmax/(1 + \frac{Kd}{C})$where R_{eq} (measured in RU) is plotted against protein concentration (C). R_{max} is the theoretical maximum RU response and K_d is the apparent membrane affinity. Data were fit using the Kaleidagraph fit parameter of (m0*m1)/(m0+m2);m1=1100;m2=1. ΔRU data was normalized in GraphPad Prism 8 for windows (La Jolla, CA) and plotted in Kaleidagraph (Reading, PA).

Lipidomics

HEK293 cells were treated with the indicated concentration of fendiline for 48 hours, collected through centrifugation, rinsed with PBS and protein concentration was determined. Cells were pelleted, flash frozen in liquid N_2 and stored at -80°C until subsequent LC/MS/MS processing by Avanti Polar Lipids, Inc.. Prior to LC-MS/MS analysis, lipids were extracted using the Folch method.[71] The bottom chloroform layer taken after centrifugation was diluted with internal standards for LPA, LPS, PA and PS for quantization by injection on LC-MS/MS. Samples were injected on a LC-MS/MS method using a Waters Acquity UPLC / AB Sciex 5500 MS system performing reversed

bioRxiv preprint doi: https://doi.org/10.1101/2021.06.08.447555; this version posted June 8, 2021. The copyright holder for this preprint (which was not certified by peer review) is the author/funder. All rights reserved. No reuse allowed without permission.

phase separation of LPA and LPS and PA and PS components with MS/MS detection. Each molecular species identified by the [M-H] m/z of its acyl carbon:double bond (CC:DB i.e. 34:2 PA) was quantified against the response of the internal standards of known concentration. Content of individual and total LPA/PA and LPS/PS was reported. Values were corrected to $1x10^6$ cells for all samples.

BSL-4 immunofluorescence assay

Vero E6 cells were seeded at 2e4 cells/well in black 96-well poly-D-lysine treated plates (Greiner Bio-One Cellcoat®). Twenty-four hours prior to infection, fendiline was diluted in 0.5% DMSO and Vero E6 cell culture media at indicated concentrations and added to cells. An equivalent percentage of DMSO in culture media served as the vehicle control. Following pretreatment, compound was removed, and cells were incubated with Ebola virus (Kikwit) or Marburg virus (Ci67) at a multiplicity of infection (MOI) of 0.1 or 1.0 in a BSL-4 located at USAMRIID. Following absorption for 1 hour, virus inoculum was removed and cells were washed. Plates were divided into three post-infection treatment groups (day 0, every day- e.d., every other day-e.o.d.), and received either culture media or freshly prepared fendiline or vehicle control. Cells were then treated daily with freshly prepared compound or left to incubate based on their designated treatment group. At 48 hours (MOI=1.0), 72 or 96 hours (MOI=0.1) post infection, cells were washed with PBS and submerged in 10% neutral buffered formalin for 24 hours prior to removal from the BSL-4 laboratory. Formalin was removed and cells were washed with PBS. Cells were blocked with 3% BSA/PBS cell staining buffer (BioLegend) and incubated at 37°C for 2 hours. Ebola virus GP-specific mAb KZ52 or Marburg virus GP-specific mAb 9G4, diluted

bioRxiv preprint doi: https://doi.org/10.1101/2021.06.08.447555; this version posted June 8, 2021. The copyright holder for this preprint (which was not certified by peer review) is the author/funder. All rights reserved. No reuse allowed without permission.

in 3% BSA/PBS, were added to appropriate wells containing infected cells and incubated at room temperature for 2 hours. Cells were washed three times with PBS prior to addition of goat anti-human or goat anti-mouse IgG-Alexa-488 secondary antibody. Following 1-hour incubation with secondary antibody, cells were washed 3 times prior to counterstaining with Hoechst's stain diluted in PBS. Cells were imaged and percent of virus infected cells calculated using the Operetta High Content Imaging System and Harmony® High Content Imaging and Analysis Software (PerkinElmer).

VLP collections & functional budding assays

HEK293 cells were transfected and treated with fendiline as described in the previous section, *Cell Culture, Transfection & Pharmacological Treatments*. Budding assays were performed as described previously.[39,72] In brief, VLP containing supernatants were harvested from cells and clarified through low speed centrifugation. Clarified VLPs were loaded onto a 20% sucrose cushion in STE buffer (10 mM TRIS, 100 mM NaCl, 1 mM EDTA, pH 7.6), isolated through ultracentrifugation, and resuspended in either 150 mM ammonium bicarbonate (functional budding assays), 2.5% glutaraldehyde in 0.1 M cacodylate buffer (TEM experiments), STE buffer (entry assays) or 0.1 M phosphate buffer for CD and thermal melting (PB; 0.02 M sodium phosphate monobasic, 0.08 M sodium phosphate dibasic, pH 7.4). VLP samples were stored at -80°C for functional budding assays, -20°C for entry assays or 4°C for TEM and CD analysis.

For functional budding assays, cell lysate samples were harvested and lysed on ice with RIPA buffer (150mM NaCl, 5mM EDTA pH=8, 50mM Tris pH 7.4, 1% Triton-X, 0.1% SDS, 0.5% deoxycholic acid) supplemented with Halts protease inhibitors. Prior to

bioRxiv preprint doi: https://doi.org/10.1101/2021.06.08.447555; this version posted June 8, 2021. The copyright holder for this preprint (which was not certified by peer review) is the author/funder. All rights reserved. No reuse allowed without permission.

separation on a 12% SDS-PAGE gel, cell lysate and VLP sample volume loading were normalized to sample protein content, determined by a BCA assay. Gels were transferred to a nitrocellulose membrane and immunoblotted was performed as described previously in the section, *Immunoblotting*. Following ECL detection, VP40 cell lysate ($VP40_{CL}$) expression was normalized to the respective GAPDH band density. The relative budding index was calculated according to the ratio of $density_{VLP}/density_{C+VLP}$ (where $density_{VLP}$ is the eVP40 VLP band density and $density_{C+VLP}$ is the eVP40 cell lysate + VLP band density).

Scanning electron microscopy

HEK293 cells were transfected with FLAG-eVP40 and treated as described in the previous section, *Cell Culture, Transfections & Pharmacological Treatments.* Cells were scraped and collected through low-speed centrifugation at 48 hours post transfection, and stored in primary fixative (2% glutaraldehyde, 2% paraformaldehyde in 0.1 M cacodylate buffer, pH 7.35) at 4°C until processing. During processing, samples were fixed to coverslips and post-stained with 1% osmium tetroxide in 0.1 M cacodylate buffer. Samples were extensively rinsed with water and dehydrated with a graded series of ethanol followed by drying in a Tousimis 931 Supercritical Autosamdri® device. Prior to imaging, samples were coated with 3 nm Iridium. A Field Emission Scanning Electron Microscope Magellan 400 (FEI) (Hillsboro, OR) was used to collect images, with assistance from Tatyana Orlova at the Notre Dame Integrated Imaging Facility.

Transmission electron microscopy imaging

bioRxiv preprint doi: https://doi.org/10.1101/2021.06.08.447555; this version posted June 8, 2021. The copyright holder for this preprint (which was not certified by peer review) is the author/funder. All rights reserved. No reuse allowed without permission.

VLPs were purified as previous described in *VLP Collections & Functional Budding Assays.* Following ultracentrifugation, VLPs were resuspended in fixative (2.5% glutaraldehyde in 0.1 M cacodylate buffer). Purified VLPs were applied onto glow discharged carbon formvar grids and negatively stained using 4% uranyl acetate. Samples were imaged with a FEI Tecnai T12 electron microscope equipped with a tungsten source and operating at 80 kV. VLP length and diameter measurements were quantified using ImageJ software. For diameter analysis, eight different diameters were measured across random areas on each VLP, and the mean diameter was reported.

Circular dichroism

VLPs were produced in the presence of DMSO or fendiline and purified as previously described in the *VLP collections* section. PB buffer was added to a 10-mm path-length Spectrosil Far UV Quartz cuvette (Starna Cells CatID: 21-Q-10) and a background spectra was collected and autosubtracted from VLP samples. VLP samples were loaded into the 10-mm cuvette diluted in PB buffer to an approximate final protein concentration of 30 µg/mL. Circular dichroism spectra of VLP samples were collected between 200-280 nm at a 0.2 nm step size with 0.5s time-per-point (with adaptive sampling) using a Chirascan spectrometer (Applied Photophysics, Leatherhead, UK). Absorbance spectra (Abs) and detector signal (hv) were collected simultaneously as controls. After collecting the CD spectra, a microstir bar was added to the cuvette and thermal melting was run from 20°C-93°C using a 0.5°C step ramping at 1.00°C/minute with a tolerance of 0.20°C; simultaneously, spectra were collected at a single wavelength of 220 nm with a time-per-point of 24 seconds. Absorbance spectra (Abs) and detector

bioRxiv preprint doi: https://doi.org/10.1101/2021.06.08.447555; this version posted June 8, 2021. The copyright holder for this preprint (which was not certified by peer review) is the author/funder. All rights reserved. No reuse allowed without permission.

signal (hv) were collected simultaneously as controls. At the end of thermal melting measurement collection, temperature set-points were replaced with temperatures measured by the sample handling unit. Data was converted from Chirascan filetype to CSV and then extracted into GraphPad PRISM 7. Using the first derivative of the circular dichroism spectral signal in respect to temperature, the maxima was taken as the melting point of the sample. Melting temperatures of the three replicates were averaged for the reported T_m.

DiI entry assay

VLP labeling. VLPs produced from HEK293 cells expressing FLAG-eVP40 and eGP were purified as previously described in the *Functional Budding Assays* section. DiI entry assays were performed as described previously.[58,73] In brief, following ultra-centrifugation VLPs were resuspended in STE buffer and further purified by filtering through a 0.22 µm filter. Protein content of VLP samples were normalized to 0.1 µg/mL using STE buffer. VLPs were labeled with DiI for 1 hr at RT with gentle agitation (final DiI = 0.06 µM). Following incubation, labeled VLP samples were concentrated down to equal volumes, and brought up to volume in phenol-free MEM with 2% FBS and 4% BSA.

TIM-1 dependent entry. HEK293 cells were transfected with TIM-1 for 24 hours prior to incubation with DiI-labeled VLPs and briefly rinsed with phenol-free MEM with 2% FBS and 4%BSA. DiI-VLPs were added to TIM-1 expressing HEK293 cells, spinoculated for 45 min at 4°C, and allowed to incubate for 1 hr at 37°C. Plates were then rinsed with PBS, fixed with 4% paraformaldehyde in PBS, their nuclei stained with Hoechst 3342, and

bioRxiv preprint doi: https://doi.org/10.1101/2021.06.08.447555; this version posted June 8, 2021. The copyright holder for this preprint (which was not certified by peer review) is the author/funder. All rights reserved. No reuse allowed without permission.

stored at 4°C until imaging. During image acquisition, z-stacks were acquired of 10-15 frames (1 µm steps).

Toxicity analysis

HEK293 and Vero E6 cell toxicity following fendiline treatment was tested at the indicated time points using the Cell Titer Glo Viability Assay (Promega, Madison WI) according to the manufacturer's protocol. In brief, HEK293 cells were treated with the indicated concentration of fendiline or control for 24 or 48 hours. Vero E6 cells were treated for 24 hours, the drug was removed and the cells were replenished with Vero E6 culture media, to mirror the corresponding ebolavirus and Marburgvirus infections at BSL-4. Following the one-hour mock infection, cells were washed with PBS and plates were divided into three treatment groups (day 0, e.d., e.o.d.), and cells received either culture media or freshly prepared fendiline or vehicle control and were then treated daily with freshly prepared compound or left to incubate based on their designated treatment group. At 48, 72, and 96 hours following mock infection, and mirroring the post infection fixation time points, CellTiter-Glo® reagent was added to each well in accordance with the manufacturer's instructions. Both HEK293 and Vero E6 toxicity assays luminescence readings were recorded using a SpectraMax® M5 (Molecular Devices®) plate reader.

Mathematical model of *in vitro* experiments

We implemented a system of ordinary differential equations (ODEs) to describe the dynamics of host target cells, infected cells and free virus in different combinations

bioRxiv preprint doi: https://doi.org/10.1101/2021.06.08.447555; this version posted June 8, 2021. The copyright holder for this preprint (which was not certified by peer review) is the author/funder. All rights reserved. No reuse allowed without permission.

reflecting the *in vitro* experimental systems used here. These equations are similar to those used to simulate Ebola virus dynamics in earlier work [74,75].

$$\frac{dT}{dt} = -\beta TV \quad (1)$$

$$\frac{dI}{dt} = \beta TV - \delta I \quad (2)$$

$$\frac{dV}{dt} = pI - cV \quad (3)$$

Where *T*, *I* and *V* represent numbers of susceptible target host cells, infected cells and free virions respectively and parameters are described in Table 2.

We modified appropriate parameters in equations 1-3 to represent the following experimental systems during calibration of the mathematical model:

- Viral budding assay (set β=0, T(0) = 0, I(0) = 2.625x10^6, V(0) = 0, vary δ, c, p)
- Viral entry assay (set p=0, T(0) = 6.3x10^5, I(0) = 0, V(0) = 6.3x10^3, vary β, δ, c)
- BSL-4 Cellular infection assay (BSL4) (T(0) = 5x10^4, I(0) = 0, V(0) = 5x10^4 (MOI 1) or V(0) = 5x10^3 (MOI 0.1) , vary β, δ, c, p)

Fendiline treatment effects are simulated using E_{max} dose response curves:

$$f_X = E_{max} \frac{C^H}{C_{50}^H + C^H}$$

Where *C*: concentration of fendiline, E_{max}: maximum effect of fendiline, *H*: hill constant for the dose response curve, and C_{50} concentration with 50% of E_{max} efficacy. E_{max}, C_{50}

bioRxiv preprint doi: https://doi.org/10.1101/2021.06.08.447555; this version posted June 8, 2021. The copyright holder for this preprint (which was not certified by peer review) is the author/funder. All rights reserved. No reuse allowed without permission.

and H are fitted separately for fendiline effects on budding ($f_{budding}$) or entry (f_{entry}). Fendiline efficacy (f_X) is defined as a fraction where f_X=0 implies no effect and f_X=1 implies 100% inhibition of X (X = budding or entry). Fendiline effects are integrated into equations (1-3) by multiplying β by (1-f_{entry}) and multiplying p by (1-$f_{budding}$). Fendiline concentrations are assumed to be constant over the observation periods based on low *in vitro* degradation rates of the drug. Daily treatment in the BSL-4 assays (e.d.) are simulated by removing all free virus particles from the equations at each dosing time.

We calibrated the model in two stages. First, we calibrated to the budding and entry assays. The uncoupling of budding and entry in this data allows us to define biologically feasible ranges for the effects of fendiline on budding and entry separately. Using these feasible ranges, we proceed to calibrate the full model to the BSL-4 data (day-1/0 and e.d.). Therefore, we allow the budding and entry assays to inform the BSL-4 simulations without imposing strict assumptions about the equivalency between the two systems. In this way we progressively build complexity into the model accounting for fendiline effects on viral budding, entry, and infection progression.

Calibrating to budding and entry assays we restrict the value of p to be larger than 1 and c to be between 0 and 5. These assumptions are in line with previous estimates, and are necessary to qualitatively reproduce viral production observed, but not quantified, in the budding assays. Parameters are estimated using Matlab's non-linear least squares

bioRxiv preprint doi: https://doi.org/10.1101/2021.06.08.447555; this version posted June 8, 2021. The copyright holder for this preprint (which was not certified by peer review) is the author/funder. All rights reserved. No reuse allowed without permission.

optimization algorithm. Parameter bounds and final values are defined in Supplementary Information Table 2.

Statistical testing

All experiments were done in triplicate (unless otherwise noted). For analysis of eVLP diameter and length from TEM experiments, as well as total PA levels between control and 5 μM fendiline treated cells, a two-tailed t-test was performed. For all experiments which contained >2 experimental groups, a one-way ANOVA with Dunnett's multiple comparisons was performed on raw data. Lastly, for N&B analysis, a two-way ANOVA with Dunnett's multiple comparisons was performed.

Acknowledgements

These studies were supported by the NIH (AI081077) to R.V.S and the Indiana CTSI to E.P. and R.V.S.. M.L.H. was partially supported by a NIH T32 fellowship (T32 GM075762). We are grateful for lipidomic analysis by Avanti Polar Lipids, Inc., and for research support by Dr. Nathan Dissinger. The authors acknowledge the use of the facilities of the Bindley Bioscience Center, a core facility of the NIH-funded Indiana Clinical and Translational Sciences institute and the use of the Purdue Life Science Electron Microscopy facility.

Author Contributions

M.L.H. and R.V.S conceived of and designed the study. M.H., S.A., E.D., and C.P. performed experiments and analyzed the data. L.P. designed the BSL-4 experiments and L.P. and K.E.H. performed and analyzed the BSL-4 experiments. J.M.B. and J.D. oversaw

bioRxiv preprint doi: https://doi.org/10.1101/2021.06.08.447555; this version posted June 8, 2021. The copyright holder for this preprint (which was not certified by peer review) is the author/funder. All rights reserved. No reuse allowed without permission.

the BSL-4 work. E.P. designed and performed the mathematical modeling and analysis. M.L.H. and R.V.S. wrote the manuscript with input from all authors.

Conflict of Interest

The authors declare no conflict of interest.

bioRxiv preprint doi: https://doi.org/10.1101/2021.06.08.447555; this version posted June 8, 2021. The copyright holder for this preprint (which was not certified by peer review) is the author/funder. All rights reserved. No reuse allowed without permission.

References

1. Breman JG, Heymann DL, Lloyd G, McCormick JB, Miatudila M, Murphy FA, et al. Discovery and Description of Ebola Zaire Virus in 1976 and Relevance to the West African Epidemic during 2013-2016. J Infect Dis. 2016;214: S93–S101. doi:10.1093/infdis/jiw207
2. Liu L. Fields Virology, 6th Edition. Clin Infect Dis. 2014;59: 613–613. doi:10.1093/cid/ciu346
3. FDA. First FDA-approved vaccine for the prevention of Ebola virus disease, marking a critical milestone in public health preparedness and response | FDA. 2019 [cited 9 Jan 2020]. Available: https://www.fda.gov/news-events/press-announcements/first-fda-approved-vaccine-prevention-ebola-virus-disease-marking-critical-milestone-public-health
4. Banadyga L, Dolan MA, Ebihara H. Rodent-Adapted Filoviruses and the Molecular Basis of Pathogenesis. Journal of Molecular Biology Academic Press; Aug 28, 2016 pp. 3449–3466. doi:10.1016/j.jmb.2016.05.008
5. Mühlberger E. Filovirus replication and transcription. Future Virol. 2007;2: 205–215. doi:10.2217/17460794.2.2.205
6. Jasenosky LD, Neumann G, Lukashevich I, Kawaoka Y. Ebola virus VP40-induced particle formation and association with the lipid bilayer. J Virol. 2001;75: 5205–14. doi:10.1128/JVI.75.11.5205-5214.2001
7. Noda T, Sagara H, Suzuki E, Takada A, Kida H, Kawaoka Y. Ebola Virus VP40 Drives the Formation of Virus-Like Filamentous Particles Along with GP. J Virol. 2002;76: 4855–4865. doi:10.1128/jvi.76.10.4855-4865.2002
8. Licata JM, Simpson-Holley M, Wright NT, Han Z, Paragas J, Harty RN. Overlapping Motifs (PTAP and PPEY) within the Ebola Virus VP40 Protein Function Independently as Late Budding Domains: Involvement of Host Proteins TSG101 and VPS-4. J Virol. 2003;77: 1812–1819. doi:10.1128/jvi.77.3.1812-1819.2003
9. Wang YE, Park A, Lake M, Pentecost M, Torres B, Yun TE, et al. Ubiquitin-regulated nuclear-cytoplasmic trafficking of the Nipah virus matrix protein is important for viral budding. PLoS Pathog. 2010;6: e1001186. doi:10.1371/journal.ppat.1001186
10. Oda S-I, Noda T, Wijesinghe KJ, Halfmann P, Bornholdt ZA, Abelson DM, et al. Crystal Structure of Marburg Virus VP40 Reveals a Broad, Basic Patch for Matrix Assembly and a Requirement of the N-Terminal Domain for Immunosuppression. J Virol. 2016;90: 1839–48. doi:10.1128/JVI.01597-15
11. Bornholdt ZA, Noda T, Abelson DM, Halfmann P, Wood MR, Kawaoka Y, et al. Structural rearrangement of ebola virus vp40 begets multiple functions in the virus life cycle. Cell. 2013;154: 763–774. doi:10.1016/j.cell.2013.07.015
12. Panchal RG, Ruthel G, Kenny TA, Kallstrom GH, Lane D, Badie SS, et al. In vivo oligomerization and raft localization of Ebola virus protein VP40 during vesicular budding. Proc Natl Acad Sci U S A. 2003;100: 15936–41. doi:10.1073/pnas.2533915100
13. Jasenosky LD, Kawaoka Y. Filovirus budding. Virus Res. 2004;106: 181–8. doi:10.1016/j.virusres.2004.08.014
14. Adu-Gyamfi E, Johnson KA, Fraser ME, Scott JL, Soni SP, Jones KR, et al. Host Cell Plasma Membrane Phosphatidylserine Regulates the Assembly and Budding

bioRxiv preprint doi: https://doi.org/10.1101/2021.06.08.447555; this version posted June 8, 2021. The copyright holder for this preprint (which was not certified by peer review) is the author/funder. All rights reserved. No reuse allowed without permission.

of Ebola Virus. J Virol. 2015;89: 9440–53. doi:10.1128/JVI.01087-15

15. Bobone S, Hilsch M, Storm J, Dunsing V, Herrmann A, Chiantia S. Phosphatidylserine Lateral Organization Influences the Interaction of Influenza Virus Matrix Protein 1 with Lipid Membranes. J Virol. 2017;91: 1–15. doi:10.1128/jvi.00267-17
16. Wijesinghe KJ, Stahelin V. Investigation of the Lipid Binding Properties of the Marburg Virus. J Virol. 2016;90: 3074–3085. doi:10.1128/JVI.02607-15.Editor
17. Carnec X, Meertens L, Dejarnac O, Perera-Lecoin M, Hafirassou ML, Kitaura J, et al. The Phosphatidylserine and Phosphatidylethanolamine Receptor CD300a Binds Dengue Virus and Enhances Infection. J Virol. 2016;90: 92–102. doi:10.1128/JVI.01849-15
18. Moller-Tank S, Kondratowicz AS, Davey RA, Rennert PD, Maury W. Role of the phosphatidylserine receptor TIM-1 in enveloped-virus entry. J Virol. 2013;87: 8327–41. doi:10.1128/JVI.01025-13
19. Jemielity S, Wang JJ, Chan YK, Ahmed AA, Li W, Monahan S, et al. TIM-family Proteins Promote Infection of Multiple Enveloped Viruses through Virion-associated Phosphatidylserine. PLoS Pathog. 2013;9: e1003232. doi:10.1371/journal.ppat.1003232
20. Nanbo A, Kawaoka Y. Molecular Mechanism of Externalization of Phosphatidylserine on the Surface of Ebola Virus Particles. DNA Cell Biol. 2019;38: 115–120. doi:10.1089/dna.2018.4485
21. Amara A, Mercer J. Viral apoptotic mimicry. Nat Rev Microbiol. 2015;13: 461–9. doi:10.1038/nrmicro3469
22. Brunton B, Rogers K, Phillips EK, Brouillette RB, Bouls R, Butler NS, et al. TIM-1 serves as a receptor for Ebola virus in vivo, enhancing viremia and pathogenesis. PLoS Negl Trop Dis. 2019;13: e0006983. doi:10.1371/journal.pntd.0006983
23. Kondratowicz AS, Lennemann NJ, Sinn PL, Davey RA, Hunt CL, Moller-Tank S, et al. T-cell immunoglobulin and mucin domain 1 (TIM-1) is a receptor for Zaire Ebolavirus and Lake Victoria Marburgvirus. Proc Natl Acad Sci U S A. 2011;108: 8426–31. doi:10.1073/pnas.1019030108
24. Van Meer G, Voelker DR, Feigenson GW. Membrane lipids: Where they are and how they behave. Nature Reviews Molecular Cell Biology. 2008. pp. 112–124. doi:10.1038/nrm2330
25. Bell RM, Ballas LM, Coleman RA. Lipid topogenesis. J Lipid Res. 1981;22: 391–403.
26. Jeckel D, Karrenbauer A, Burger KNJ, Van Meer G, Wieland F. Glucosylceramide is synthesized at the cytosolic surface of various Golgi subfractions. J Cell Biol. 1992;117: 259–267. doi:10.1083/jcb.117.2.259
27. Hirama T, Das R, Yang Y, Ferguson C, Won A, Yip CM, et al. Phosphatidylserine dictates the assembly and dynamics of caveolae in the plasma membrane. J Biol Chem. 2017;292: 14292–14307. doi:10.1074/jbc.M117.791400
28. Fairn GD, Schieber NL, Ariotti N, Murphy S, Kuerschner L, Webb RI, et al. High-resolution mapping reveals topologically distinct cellular pools of phosphatidylserine. J Cell Biol. 2011;194: 257–275. doi:10.1083/jcb.201012028
29. Soni SP, Stahelin R V. The Ebola virus matrix protein VP40 selectively induces vesiculation from phosphatidylserine-enriched membranes. J Biol Chem. 2014;289:

bioRxiv preprint doi: https://doi.org/10.1101/2021.06.08.447555; this version posted June 8, 2021. The copyright holder for this preprint (which was not certified by peer review) is the author/funder. All rights reserved. No reuse allowed without permission.

33590–7. doi:10.1074/jbc.M114.586396

30. Stahelin R V. Membrane binding and bending in Ebola VP40 assembly and egress. Frontiers in Microbiology. Frontiers Research Foundation; 2014. p. 300. doi:10.3389/fmicb.2014.00300
31. Del Vecchio K, Frick CT, Gc JB, Oda S-I, Gerstman BS, Saphire EO, et al. A cationic, C-terminal patch and structural rearrangements in Ebola virus matrix VP40 protein control its interactions with phosphatidylserine. J Biol Chem. 2018;293: 3335–3349. doi:10.1074/jbc.M117.816280
32. Moller-Tank S, Maury W. Phosphatidylserine receptors: Enhancers of enveloped virus entry and infection. Virology. Academic Press Inc.; 2014. pp. 565–580. doi:10.1016/j.virol.2014.09.009
33. Cho K-J, van der Hoeven D, Zhou Y, Maekawa M, Ma X, Chen W, et al. Inhibition of Acid Sphingomyelinase Depletes Cellular Phosphatidylserine and Mislocalizes K-Ras from the Plasma Membrane. Mol Cell Biol. 2016;36: 363–74. doi:10.1128/MCB.00719-15
34. van der Hoeven D, Cho K, Zhou Y, Ma X, Chen W, Naji A, et al. Sphingomyelin Metabolism Is a Regulator of K-Ras Function. Mol Cell Biol. 2017;38: e00373-17. doi:10.1128/mcb.00373-17
35. van der Hoeven D, Cho K, Ma X, Chigurupati S, Parton RG, Hancock JF. Fendiline inhibits K-Ras plasma membrane localization and blocks K-Ras signal transmission. Mol Cell Biol. 2013;33: 237–51. doi:10.1128/MCB.00884-12
36. Bayer R, Mannhold R. Fendiline: a review of its basic pharmacological and clinical properties. Pharmatherapeutica. 1987;5: 103–36.
37. Ruigrok RW, Schoehn G, Dessen A, Forest E, Volchkov V, Dolnik O, et al. Structural characterization and membrane binding properties of the matrix protein VP40 of Ebola virus. J Mol Biol. 2000;300: 103–12. doi:10.1006/jmbi.2000.3822
38. Scianimanico S, Schoehn G, Timmins J, Ruigrok RH, Klenk HD, Weissenhorn W. Membrane association induces a conformational change in the Ebola virus matrix protein. EMBO J. 2000;19: 6732–41. doi:10.1093/emboj/19.24.6732
39. Johnson KA, Taghon GJF, Scott JL, Stahelin R V. The Ebola Virus matrix protein, VP40, requires phosphatidylinositol 4,5-bisphosphate (PI(4,5)P2) for extensive oligomerization at the plasma membrane and viral egress. Sci Rep. 2016;6: 19125. doi:10.1038/srep19125
40. Johnson KA, Budicini MR, Urata S, Gerstman BS, Chapagain PP, Li S, et al. PI(4,5)P 2 Binding Sites in the Ebola Virus Matrix Protein Modulate 2. bioRxiv. 2018; 341248. doi:10.1101/341248
41. Lemke EA. Site-specific labeling of proteins for single-molecule fret measurements using genetically encoded ketone functionalities. Methods in Molecular Biology. Humana Press Inc.; 2011. pp. 3–15. doi:10.1007/978-1-61779-151-2_1
42. Kay JG, Koivusalo M, Ma X, Wohland T, Grinstein S. Phosphatidylserine dynamics in cellular membranes. Mol Biol Cell. 2012;23: 2198–2212. doi:10.1091/mbc.E11-11-0936
43. Adu-Gyamfi E, Digman MA, Gratton E, Stahelin R V. Investigation of Ebola VP40 assembly and oligomerization in live cells using number and brightness analysis. Biophys J. 2012;102: 2517–25. doi:10.1016/j.bpj.2012.04.022
44. Hoenen T, Biedenkopf N, Zielecki F, Jung S, Groseth A, Feldmann H, et al.

bioRxiv preprint doi: https://doi.org/10.1101/2021.06.08.447555; this version posted June 8, 2021. The copyright holder for this preprint (which was not certified by peer review) is the author/funder. All rights reserved. No reuse allowed without permission.

Oligomerization of Ebola virus VP40 is essential for particle morphogenesis and regulation of viral transcription. J Virol. 2010;84: 7053–63. doi:10.1128/JVI.00737-10

45. Kerr D, Tietjen GT, Gong Z, Tajkhorshid E, Adams EJ, Lee KYC. Sensitivity of peripheral membrane proteins to the membrane context: A case study of phosphatidylserine and the TIM proteins. Biochim Biophys acta Biomembr. 2018;1860: 2126–2133. doi:10.1016/j.bbamem.2018.06.010
46. Stahelin R V. Lipid binding domains: More than simple lipid effectors. Journal of Lipid Research. 2009. pp. S299-30. doi:10.1194/jlr.R800078-JLR200
47. Stahelin R V, Scott JL, Frick CT. Cellular and molecular interactions of phosphoinositides and peripheral proteins. Chem Phys Lipids. 2014;182: 3–18. doi:10.1016/j.chemphyslip.2014.02.002
48. Menke M, Gerke V, Steinem C. Phosphatidylserine membrane domain clustering induced by annexin A2/S100A10 heterotetramer. Biochemistry. 2005;44: 15296–15303. doi:10.1021/bi051585i
49. Wen Y, Vogt VM, Feigenson GW. Multivalent Cation-Bridged PI(4,5)P2 Clusters Form at Very Low Concentrations. Biophys J. 2018;114: 2630–2639. doi:10.1016/j.bpj.2018.04.048
50. Zhao H, Hakala M, Lappalainen P. ADF/cofilin binds phosphoinositides in a multivalent manner to act as a PIP(2)-density sensor. Biophys J. 2010;98: 2327–2336. doi:10.1016/j.bpj.2010.01.046
51. Yeung T, Gilbert GE, Shi J, Silvius J, Kapus A, Grinstein S. Membrane phosphatidylserine regulates surface charge and protein localization. Science (80-). 2008;319: 210–213. doi:10.1126/science.1152066
52. Digman MA, Dalal R, Horwitz AF, Gratton E. Mapping the number of molecules and brightness in the laser scanning microscope. Biophys J. 2008;94: 2320–2332. doi:10.1529/biophysj.107.114645
53. Moe JB, Lambert RD, Lupton HW. Plaque assay for Ebola virus. J Clin Microbiol. 1981;13: 791–3. Available: http://www.ncbi.nlm.nih.gov/pubmed/7014628
54. Wang J, Qiao L, Hou Z, Luo G. TIM-1 Promotes Hepatitis C Virus Cell Attachment and Infection. J Virol. 2017;91. doi:10.1128/jvi.01583-16
55. Dejarnac O, Hafirassou ML, Chazal M, Versapuech M, Gaillard J, Perera-Lecoin M, et al. TIM-1 Ubiquitination Mediates Dengue Virus Entry. Cell Rep. 2018;23: 1779–1793. doi:10.1016/j.celrep.2018.04.013
56. Miller ME, Adhikary S, Kolokoltsov AA, Davey RA. Ebolavirus Requires Acid Sphingomyelinase Activity and Plasma Membrane Sphingomyelin for Infection. J Virol. 2012;86: 7473–7483. doi:10.1128/jvi.00136-12
57. Nanbo A, Imai M, Watanabe S, Noda T, Takahashi K, Neumann G, et al. Ebolavirus is internalized into host cells via macropinocytosis in a viral glycoprotein-dependent manner. PLoS Pathog. 2010;6: e1001121. doi:10.1371/journal.ppat.1001121
58. Kuroda M, Fujikura D, Nanbo A, Marzi A, Noyori O, Kajihara M, et al. Interaction Between TIM-1 and NPC1 Is Important for Cellular Entry of Ebola Virus. J Virol. 2015;89: 6481–93. doi:10.1128/JVI.03156-14
59. Younan P, Iampietro M, Santos RI, Ramanathan P, Popov VL, Bukreyev A. Disruption of Phosphatidylserine Synthesis or Trafficking Reduces Infectivity of Ebola Virus. J Infect Dis. 2018;218: S475–S485. doi:10.1093/infdis/jiy489

bioRxiv preprint doi: https://doi.org/10.1101/2021.06.08.447555; this version posted June 8, 2021. The copyright holder for this preprint (which was not certified by peer review) is the author/funder. All rights reserved. No reuse allowed without permission.

60. Jasenosky LD, Cadena C, Mire CE, Borisevich V, Haridas V, Ranjbar S, et al. The FDA-Approved Oral Drug Nitazoxanide Amplifies Host Antiviral Responses and Inhibits Ebola Virus. iScience. 2019;19: 1279–1290. doi:10.1016/j.isci.2019.07.003
61. Dyall J, Nelson EA, DeWald LE, Guha R, Hart BJ, Zhou H, et al. Identification of Combinations of Approved Drugs With Synergistic Activity Against Ebola Virus in Cell Cultures. J Infect Dis. 2018;218: S672–S678. doi:10.1093/infdis/jiy304
62. Nelson EA, Barnes AB, Wiehle RD, Fontenot GK, Hoenen T, White JM. Clomiphene and Its Isomers Block Ebola Virus Particle Entry and Infection with Similar Potency: Potential Therapeutic Implications. Viruses. 2016;8: E206. doi:10.3390/v8080206
63. Johansen LM, Brannan JM, Delos SE, Shoemaker CJ, Stossel A, Lear C, et al. FDA-approved selective estrogen receptor modulators inhibit Ebola virus infection. Sci Transl Med. 2013;5: 190ra79. doi:10.1126/scitranslmed.3005471
64. Johansen LM, DeWald LE, Shoemaker CJ, Hoffstrom BG, Lear-Rooney CM, Stossel A, et al. A screen of approved drugs and molecular probes identifies therapeutics with anti-Ebola virus activity. Sci Transl Med. 2015;7: 290ra89. doi:10.1126/scitranslmed.aaa5597
65. Watt A, Moukambi F, Banadyga L, Groseth A, Callison J, Herwig A, et al. A Novel Life Cycle Modeling System for Ebola Virus Shows a Genome Length-Dependent Role of VP24 in Virus Infectivity. J Virol. 2014;88: 10511–10524. doi:10.1128/jvi.01272-14
66. Darszon A, Vandenberg CA, Schönfeld M, Ellisman MH, Spitzer NC, Montal M. Reassembly of protein-lipid complexes into large bilayer vesicles: perspectives for membrane reconstitution. Proc Natl Acad Sci U S A. 1980;77: 239–243. doi:10.1073/pnas.77.1.239
67. Reeves JP, Dowben RM. Formation and properties of thin-walled phospholipid vesicles. J Cell Physiol. 1969;73: 49–60. doi:10.1002/jcp.1040730108
68. Yamashita Y, Oka M, Tanaka T, Yamazaki M. A new method for the preparation of giant liposomes in high salt concentrations and growth of protein microcrystals in them. Biochim Biophys Acta. 2002;1561: 129–34. doi:10.1016/s0005-2736(02)00338-3
69. Bolte S, Cordelières FP. A guided tour into subcellular colocalization analysis in light microscopy. Journal of Microscopy. Blackwell Publishing Ltd; 2006. pp. 213–232. doi:10.1111/j.1365-2818.2006.01706.x
70. Tsai W-H. Moment-preserving thresolding: A new approach. Comput Vision, Graph Image Process. 1985;29: 377–393. doi:10.1016/0734-189X(85)90133-1
71. Folch J, Lees M, Sloane Stanley GH. A simple method for the isolation and purification of total lipides from animal tissues. J Biol Chem. 1957;226: 497–509. doi:10.3989/scimar.2005.69n187
72. Harty RN. Hemorrhagic Fever Virus Budding Studies. In: Salvato MS, editor. Hemorrhagic Fever Viruses: Methods and Protocols. New York, NY: Springer New York; 2018. pp. 209–215. doi:10.1007/978-1-4939-6981-4_15
73. Nanbo A, Maruyama J, Imai M, Ujie M, Fujioka Y, Nishide S, et al. Ebola virus requires a host scramblase for externalization of phosphatidylserine on the surface of viral particles. Geisbert T, editor. PLOS Pathog. 2018;14: e1006848. doi:10.1371/journal.ppat.1006848

bioRxiv preprint doi: https://doi.org/10.1101/2021.06.08.447555; this version posted June 8, 2021. The copyright holder for this preprint (which was not certified by peer review) is the author/funder. All rights reserved. No reuse allowed without permission.

74. Nguyen VK, Binder SC, Boianelli A, Meyer-Hermann M, Hernandez-Vargas EA. Ebola virus infection modeling and identifiability problems . Frontiers in Microbiology Frontiers Media S.A.; 2015 p. 257. doi:10.3389/fmicb.2015.00257
75. Martyushev A, Nakaoka S, Sato K, Noda T, Iwami S. Modelling Ebola virus dynamics: Implications for therapy. Antiviral Res. 2016;135: 62–73. doi:10.1016/j.antiviral.2016.10.004

bioRxiv preprint doi: https://doi.org/10.1101/2021.06.08.447555; this version posted June 8, 2021. The copyright holder for this preprint (which was not certified by peer review) is the author/funder. All rights reserved. No reuse allowed without permission.

Figure Legends

Figure 1

Clustering of PS by eVP40 *in vitro* and in HEK 293 cells. a Representative 3D reconstructed confocal images of immobilized GUVs (DPPC:Cholesterol:DPPS:PI(4,5)P_2:TopFluor® TMR-PS(red)). Left panel: GUVs incubated without eVP40-Alexa488. Right three panels: GUVs incubated with 1.25 μM eVP40-Alexa488 (green). **b** Index of correlation (Mander's coefficient) between TopFluor® TMR-PS and eVP40-Alexa488 of different GUVs compositions incubated with 1.25 μM eVP40-Alexa488. Values are reported as mean ± s.d. A one-way ANOVA with multiple comparisons was performed; ****$p<0.0001$. **c** % TopFluor® TMR-PS quenching by eVP40 using GUVs (DPPC:Cholesterol:TopFluor®TMR-PS + increasing mol% of PS), 2.5% PI(4,5)P_2 was added to GUVs with 60% PS. Fluorescence spectra were recorded (Ex: 547 nm; Em: 550-600 nm); n=2. **d** Representative confocal images of HEK293 cells expressing various GFP-fused proteins (green) and supplemented with TopFluor® TMR-PS (red); scale bar= 10 μm. Yellow arrows indicate high intensity PS fluorescence regions **e** %PM with PS clusters = area of high intensity fluorescent PS clusters over total plasma membrane area from images in panel (d). Black bars are control proteins and blue bars are eVP40 proteins. Values are reported as mean ± s.d.; N>18, n=3; A one-way ANOVA was performed with multiple comparisons compared to the control GFP %PS clustering (***$p=0.0007$, **$p=0.004$). DPPC: dipalmitoyl-phosphatidylcholine; DPPS: dipalmitoyl-phosphatidylserine; GUVs: giant unilamellar vesicles; PS: phosphatidylserine; PM: plasma membrane.

bioRxiv preprint doi: https://doi.org/10.1101/2021.06.08.447555; this version posted June 8, 2021. The copyright holder for this preprint (which was not certified by peer review) is the author/funder. All rights reserved. No reuse allowed without permission.

Figure 2

Effect of PS concentration on eVP40 binding affinity to and oligomerization on membranes. a-c SPR demonstrates that eVP40 affinity to LUVs increases in relation to PS concentration. **a** Representative normalized sensorgram of His_6-eVP40 binding to LUVs containing 1% PS indicating an apparent affinity of 2.5 μM. **b** Representative normalized sensorgram of His_6-eVP40 binding to LUVs containing 11% PS indicating an apparent affinity of 0.65 μM. **c** Representative normalized sensorgram of His_6-eVP40 binding to LUVs containing 22% PS indicating an apparent affinity of 0.18 μM. **d-e** PS concentration in LUVs enhances the ability of His_6-eVP40 to oligomerize on membranes. **d** Representative western blot of chemical crosslinking performed on His_6-WT-eVP40 following incubation with LUVs of varying PS content (detected by Mouse α-His antibody & HRP-Sheep α-Mouse). **e** Oligomerization capacity was determined from the western blot band density ratio of oligomers/(monomer + dimer) from chemical crosslinking experiments. A one-way ANOVA was performed with multiple comparisons compared to the control 0% PS LUVs control (30% PS *p= 0.021; 60% PS *p=0.017). n=3**.** Values are reported as mean ± s.d.; SPR: surface plasmon resonance; LUVs: large unilamellar vesicles; PS: phosphatidylserine; HRP: horseradish peroxidase.

Figure 3

PS concentration, localization, and dynamics in fendiline treated HEK293 cells. a Lipidomic analysis (LC/MS/MS) of total lipids extracted from HEK293 cells treated with the indicated concentration of fendiline (48 hours) demonstrated a significant reduction of total cellular PS levels. Values are normalized to DMSO control and are reported as mean

bioRxiv preprint doi: https://doi.org/10.1101/2021.06.08.447555; this version posted June 8, 2021. The copyright holder for this preprint (which was not certified by peer review) is the author/funder. All rights reserved. No reuse allowed without permission.

± s.d.; n=3; A one-way ANOVA was performed with multiple comparisons to the control DMSO (*p=0.0120, ***p=0.0003). **b-c** Analysis of PS plasma membrane localization in response to fendiline treatment in HEK293 cells. **b** Representative confocal images from live cell imaging of HEK293 cells expressing GFP-LactC2 and treated with fendiline for 48 hours; scale bars= 10 µm. **c** Effect of fendiline on PS plasma membrane localization was calculated by the ratio of GFP fluorescence at the plasma membrane intensity/intracellular intensity. Values are normalized to DMSO control and are reported as mean ± s.d.; N>15, n=3; A one-way ANOVA was performed with multiple comparisons compared to the DMSO control (**p=0.0031) **d-e** Analysis of PS clustering in HEK293 cells in response to fendiline treatment through N&B analysis. **d** *Left panel:* Representative images from time-lapse (30 frames) imaging of HEK293 expressing GFP-LactC2 and treated with fendiline for 48 hours; scale bar= 5 µm. *Middle panel:* Brightness and Intensity plots for each representative image. *Right panel:* Selection map correlating each pixel in the representative image to an oligomerization state (b value) (red: monomer-5mer, green: 5mer-10mer, blue: >10mer). **e** Average % pixels quantification from panel (d)= Percentage of GFP-LactC2 with brightness values corresponding to monomer-5mer (~1.-1.5), 5mer-10mer (~1.5-1.9) and >10mer (>1.9) over the total pixels within each image. Values are reported as mean ± s.d.; N≥9, n=3; A two-way ANOVA was performed with Dunnett's multiple comparisons comparted to the control DMSO % average pixels (****p<0.0001, **p=0.0043).GFP-LactC2: phosphatidylserine sensor; N&B: Number & Brightness analysis; PM: plasma membrane; PS: phosphatidylserine.

<u>Figure 4</u>

bioRxiv preprint doi: https://doi.org/10.1101/2021.06.08.447555; this version posted June 8, 2021. The copyright holder for this preprint (which was not certified by peer review) is the author/funder. All rights reserved. No reuse allowed without permission.

Evaluation of fendiline efficacy in the inhibition of authentic EBOV and MARV spread. a-d Effect of fendiline on EBOV infection. **a** Representative confocal images of Vero E6 cells infected with EBOV (Kikwit) at the indicated MOI and treated with the indicated concentration of fendiline. Cells were pretreated 24 hours prior to infection with the indicated concentration of fendiline. Post infection, cells were treated 1 hour later (d -1/0), treated every day (e.d), or treated every other day (e.o.d) and fixed at either 48 hours, 72 hours or 96 hours post infection. (green=EBOV; blue= nuclei). White numbering in top right corner indicates %infection **b-d** Quantification of % inhibition of EBOV by fendiline. **b** 48 hours (MOI 1.0) **c** 72 hours (MOI 0.1) **d** 96 hours (MOI 0.1). Values are reported as mean ± s.d. A one-way ANOVA was performed with multiple comparisons was performed. n=3. **e-h** Effect of fendiline on MARV infection. **e** Representative confocal images of Vero E6 cells infected with MARV (Ci67) at the indicated MOI and treated with the indicated concentration of fendiline. Cells were pretreated 24 hours prior to infection with the indicated concentration of fendiline. Post infection, cells were treated 1 hour later (d -1/0), treated every day (e.d), or treated every other day (e.o.d) and fixed at either 48 hours, 72 hours or 96 hours post infection. (green=MARV; blue= nuclei). White numbering in top right corner indicates %infection. **f-h** Quantification of % inhibition of MARV by fendiline. **f** 48 hours (MOI 1.0) **g** 72 hours (MOI 0.1) **h** 96 hours (MOI 0.1). Values are reported as mean ± s.d. A one-way ANOVA was performed with multiple comparisons was performed. n=3. EBOV: Ebola virus; MOI: multiplicity of infection; MARV: Marburg virus; d. -1/0: treatment 1 hour after infection; e.d.: treatment every day; e.o.d.: treatment every other day.

bioRxiv preprint doi: https://doi.org/10.1101/2021.06.08.447555; this version posted June 8, 2021. The copyright holder for this preprint (which was not certified by peer review) is the author/funder. All rights reserved. No reuse allowed without permission.

Figure 5

Analysis of eVP40/mVP40 cellular localization and oligomerization following fendiline treatment. a-c Effect of fendiline on eVP40 and mVP40 PM localization in HEK293 cells after 48 hours of treatment. **a** Representative confocal images from live cell imaging experiments of HEK293 cells expressing EGFP-WT-eVP40 (top panel) and EGFP-WT-mVP40 (bottom panel) after 48 hours of fendiline treatment. scale bars= 10 µm. Effect of fendiline on eVP40 **(b)** and mVP40 **(c)** PM localization was quantified by the ratio of EGFP fluorescence intensity at the PM / total EGFP fluorescence intensity (and normalized to DMSO control). N>15, n=3. Values are reported as mean ± s.d. A one-way ANOVA with multiple comparisons was performed compared to the DMSO control. **d-e** Analysis of eVP40 oligomerization in HEK293 cells in response to 48 hour fendiline treatment using N&B analysis. **d** *Left panel:* Representative images from time-lapse (30 frames) of HEK293 expressing EGFP-WT-eVP40 and treated with fendiline for 48 hours. scale bar = 5 µm. *Middle panel:* Brightness and Intensity plots for each representative image. *Right panel:* Selection map correlating each pixel in the representative image to an oligomerization state (b value) (red: monomer-hexamer, green: hexamer-12mer, blue: 12mer-24mer, pink: >24mer). **e** Average % pixel quantification from panel (d)= % of GFP-WT-eVP40 with brightness values corresponding to monomer-hexamer (~1.-1.6), hexamer-12mer (~1.6-2.0), 12mer-24mer (2.0-3.2) and >24mer (>3.2) over the total pixels within each image. Values are reported as mean ± s.d.; N≥9, n=3; A two-way ANOVA was performed with Dunnett's multiple comparisons compared to the control DMSO % average pixels (**p=0.0035). PM: plasma membrane; N&B: Number & Brightness analysis.

bioRxiv preprint doi: https://doi.org/10.1101/2021.06.08.447555; this version posted June 8, 2021. The copyright holder for this preprint (which was not certified by peer review) is the author/funder. All rights reserved. No reuse allowed without permission.

Figure 6

VLP production and morphology in HEK293 cells in the presence of fendiline. a-d Functional budding assays assessed at 24 hours (a-b) and 48 hours (c-d) post treatment. **a** Representative western blot of budding assays performed at 24 hours. VLP samples (top panel) and cell lysate samples (bottom panel) collected from HEK293 cells and immunoblotted for eVP40 expression; GAPDH served as a loading control. eVP40 detected by (Rabbit α-eVP40 and HRP-Goat α-Rabbit); GAPDH detected by mouse α-GAPDH and HRP-Sheep α-Mouse) **b** Quantification of relative budding index at 24 hours post fendiline treatment. Relative budding index was determined by the western blot band density of eVP40 in the VLP fraction/(total eVP40 cell lysate + eVP40 VLP band density) and was normalized to the DMSO control. Cell lysate eVP40 band density was normalized to GAPDH band density prior to use in budding index quantification. n=3. Values are reported as mean ± s.d. A one-way ANOVA was performed with multiple comparisons compared to the DMSO control. **c** Representative western blot of budding assays performed at 48 hours. VLP samples (top panel) and cell lysate samples (bottom panel) collected from HEK293 cells and immunoblotted for eVP40 expression; GAPDH served as a loading control. eVP40 detected by (Rabbit α-eVP40 and HRP-Goat α-Rabbit); GAPDH detected by (Mouse α-GAPDH and HRP-Sheep α-Mouse) **b** Quantification of relative budding index at 48 hours post fendiline treatment. Relative budding index was determined by the western blot band density of eVP40 in the VLP fraction/(total eVP40 cell lysate + eVP40 VLP band density) and was normalized to the DMSO control. Cell lysate eVP40 band density was normalized to GAPDH band density prior to use in

bioRxiv preprint doi: https://doi.org/10.1101/2021.06.08.447555; this version posted June 8, 2021. The copyright holder for this preprint (which was not certified by peer review) is the author/funder. All rights reserved. No reuse allowed without permission.

budding index quantification. n=3. Values are reported as mean ± s.d. A one-way ANOVA was performed with multiple comparisons compared to the DMSO control. (*p=0.0260) **e-f** SEM micrographs of HEK93 cells. **e** Representative micrographs of mock transfected HEK293 cells harvested after 48 hours of no treatment or DMSO treatment. **f** Representative micrographs of HEK293 cells expressing FLAG-eVP40 and harvested after 48 hours of no treatment, DMSO treatment, or the indicated concentration of fendiline. VLPs: virus like particles; SEM: scanning electron microscopy; GAPDH: glyceraldehyde 3-phosphate dehydrogenase; HRP: horseradish peroxidase.

Figure 7

Effect of fendiline on eVLP morphology and TIM-1 dependent eVLP entry. **a-c** TEM analysis of eVLP morphology. **a** Representative transmission electron micrographs of eVLPs purified from HEK293 cells expressing FLAG-eVP40 and eGP following 48 hours of DMSO (left panel) or 5 μM fendiline treatment (right panel). **b** Quantification of eVLP length (μm) of DMSO-derived eVLPs (black) and fendiline-derived eVLPs (blue). N>50, n=3. Values are reported as mean ± s.d. A two-tailed t-test was performed (**p=0.0139). **c** Quantification of eVLP diameter (nm) of DMSO-derived eVLPs (black) and fendiline-derived eVLPs (blue). N>50, n=3. Values are reported as mean ± s.d. A two-tailed t-test was performed (*p=0.0430). **d-e** Fluorescence based DiI TIM-1 dependent entry assay. **d** Representative confocal images from the DiI-entry assay comparing entry of eVLPs produced from DMSO (top panel) and fendiline-treated HEK293 cells (bottom panel) into target cells (HEK293 cells transiently expressing increasing amounts of TIM-1; 0.0 μg, 0.5 μg, 1.0 μg). A stack of 10 frames was acquired for each image. DiI (initially red) was

bioRxiv preprint doi: https://doi.org/10.1101/2021.06.08.447555; this version posted June 8, 2021. The copyright holder for this preprint (which was not certified by peer review) is the author/funder. All rights reserved. No reuse allowed without permission.

recolored to yellow for easier observation in print; blue (Hoechst 3342 stain); scale bar = 10 µm. **e** Quantification of eVLP entry was performed by calculating the total number of DiI punctate / the total number of DiI-positive cells. Three images from each z-stack was quantified. N=9, n=3. Values are reported as mean ± s.d. A one-way ANOVA was performed with multiple comparisons against the 0.0 µg TIM-1 condition for both DMSO- and fendiline derived eVLPs.(****p<0.0001; **p=0.0093). eVLP: entry-competent viral like particles; TEM: transmission electron microscopy; TIM-1: t-cell immunoglobulin receptor-1; eVLPs: entry-competent VLPs; eGP: Ebola glycoprotein; DiI: 1,1'-Dioctadecyl-3,3,3',3'-Tetramethylindocarbocyanine Perchlorate.

Figure 8

Calibrated mathematical model reproduces key observations in multiple experimental datasets. Percentage infected cells is shown for various fendiline concentrations given prior to infection (d-1/0, **a-c**) or daily (e.d., **d-f**). (**a,d**) MOI 1; (**b,c,e,f**) MOI 0.1. (**g-h**) Model predicted cell and viral dynamics for MOI 0.1. (**i**) Model predicted dose response curves for fendiline effects on viral budding and entry in the BSL4 experiments.

bioRxiv preprint doi: https://doi.org/10.1101/2021.06.08.447555; this version posted June 8, 2021. The copyright holder for this preprint (which was not certified by peer review) is the author/funder. All rights reserved. No reuse allowed without permission.

Tables

Table 1. Antibodies used in immunoblotting

Target	Species	Tag	Dilution	Cat. #	Company
eVP40	Rabbit		1/40,000	0301-010	IBT Bioservices
Rabbit	Goat	HRP	1/5,000	205718	Abcam
GAPDH	Mouse		1/5,000	8245	Abcam
Mouse	Sheep	HRP	1/10,000	6808	Abcam
EBOV-GP (KZ52)	Human		1.0 µg/ml	0260-001	IBT Bioservices
Human	Goat	Alexa-488	0.7 µg/ml	A11013	Invitrogen
MARV-GP (9G4)	Mouse		4.0 µg/ml	N/A	USARMIID Hybridoma Division
Mouse	Goat	Alexa-488	1.0 µg/ml	A11029	Invitrogen
6xHis	Mouse		1/1,000	A5588	Sigma

Table 2. Mathematical model parameter descriptions and values

Symbol	Description	Unit	Value from calibration to budding and entry assays	Ranges based on fits to budding and entry assays	Value from calibration to BSL4 data – using ranges defined by budding and entry assays
β	Infection rate constant of target cells by free virions	$(\text{Virion.day})^{-1}$	N/A	0 - inf	$6.6\text{x}10^{-6}$
δ	Death rate constant of infected cells	Day^{-1}	N/A	0 - inf	$4.6\text{x}10^{-6}$
c	Decay rate constant of free virions	Day^{-1}	N/A	0 - 5	5
p	Viral production rate constant by infected cells	$\text{Virions.(Infected cell.day)}^{-1}$	N/A	1 - inf	49

bioRxiv preprint doi: https://doi.org/10.1101/2021.06.08.447555; this version posted June 8, 2021. The copyright holder for this preprint (which was not certified by peer review) is the author/funder. All rights reserved. No reuse allowed without permission.

H_b	Hill constant for Fendiline effects on VLP budding		2.7	0.5 - 7	3.4
H_e	Hill constant for Fendiline effects on VLP entry		11	0.5 - 20	4.7
C_{50}^{b}	Concentration with 50% of maximum Fendiline effect on VLP budding	μM	5.7	2 - 20	18
C_{50}^{e}	Concentration with 50% of maximum Fendiline effect on VLP entry	μM	4.8	0.5 - 20	15
E_{max}^{b}	Maximum Fendiline effect on VLP budding		0.98	0.3 - 1	0.3
E_{max}^{e}	Maximum Fendiline effect on VLP entry		0.76	0.3 - 1	0.33

bioRxiv preprint doi: https://doi.org/10.1101/2021.06.08.447555; this version posted June 8, 2021. The copyright holder for this preprint (which was not certified by peer review) is the author/funder. All rights reserved. No reuse allowed without permission.

Expanded View Figure Legends

Expanded View 1 (EV1)

Fluorescence profiles of PS and WT-eVP40 through confocal microscopy and plot profile analysis of fluorescently labeled GUVs and Alexa488-eVP40. **a** Representative confocal images of fluorescently labeled (TopFluor® TMR-PS) GUVs with varying lipid compositions (red) following incubation with eVP40-Alexa88 (green). Colocalization between eVP40 and PS within GUVs was indicated by plot profile analyses of fluorescence signals between TopFluor® TMR-PS (red dotted line) and eVP40-Alexa488 (green solid line) performed at indicated open yellow lines in **a** and shown in **b-d**. **b** Plot profile analysis of eVP40-Alexa488 and control GUVs (DPPC:Cholesterol:0.2mol% TopFluor® TMR-PS), **c** Plot profile analysis of eVP40-Alexa488 and PS GUVs (DPPC:Cholesterol:0.2mol% TopFluor® TMR-PS:DPPS). * indicates overlap in fluorescence signals. **d** Plot profile analysis of eVP40-Alexa488 and PS+PI(4,5)P_2 GUVs (DPPC:Cholesterol:0.2mol% TopFluor® TMR-PS:DPPS:PI(4,5)P_2). PS: phosphatidylserine; DPPC: dipalmitoyl-phosphatidylcholine; DPPS: dipalmitoyl-phosphatidylserine.

Expanded View 2 (EV2)

Fluorescence profiles of PS and GFP-WT-eVP40 in HEK 293 cells through confocal microscopy. **a** Representative confocal images from live cell imaging of HEK293 expressing various GFP-fused proteins (GFP; green) following supplementation with TopFluor® TMR-PS (red). Solid white lines indicate where plot profile analysis was performed; scale bar= 10 µm. **b-c** Validation of ability to detect exogenously added

bioRxiv preprint doi: https://doi.org/10.1101/2021.06.08.447555; this version posted June 8, 2021. The copyright holder for this preprint (which was not certified by peer review) is the author/funder. All rights reserved. No reuse allowed without permission.

fluorescently labelled PS within the inner leaflet of the plasma membrane of cells **b** Plot profile analysis of HEK293 cells expressing cytosolic GFP. **c** Plot profile analysis of HEK293 cells expressing the PS sensor GFP-LactC2 **d-e** Investigation of functionally distinct eVP40 proteins ability to bind to fluorescently labelled PS within the inner leaflet of the plasma membrane in living cells. **d** Plot profile analysis of HEK293 cells expressing GFP-WT-eVP40. **e** Plot profile analysis of HEK293 cells expressing GFP-K224A-eVP40 (PS-binding residue mutant). **f** Plot profile analysis of HEK293 cells expressing GFP-WE/A-eVP40 (oligomerization deficient mutant). TopFluor TMR-PS fluorescence signal intensity (red dotted line) and GFP fluorescence signal intensity (green solid line).

Expanded View 3 (EV3)

Validation of *in-vitro* and cellular PS clustering experiments. **a** GUVs of varying compositions were imaged prior to and following the addition of 1.25 μM eVP40-Alexa. eVP40-Alexa 488 enrichment ratios at the membrane of the GUVs was calculated by the ratio the Alexa488 fluorescence intensity at the GUV membrane / Alexa488 total fluorescence. Values are reported as mean ± s.d.; of n=3. A two-way ANOVA with multiple comparisons was performed. *$p<0.0001$. **b** Representative images of the step-wise image analysis workflow of quantifying PS clustering in living HEK293 cells expressing GFP-fused proteins using a custom ImageJ macro. scale bar= 10 μm. **c** Representative images from live cell imaging experiments of HEK293 cells expressing control GFP-fused proteins specific for the plasma membrane (GPI), and specific lipids, PS (LactC2) and $PI(4,5)P_2$ (PLCδ-PH). scale bar= 10μm.

bioRxiv preprint doi: https://doi.org/10.1101/2021.06.08.447555; this version posted June 8, 2021. The copyright holder for this preprint (which was not certified by peer review) is the author/funder. All rights reserved. No reuse allowed without permission.

Expanded View 4 (EV4)

Profile of fendiline toxicity and efficacy in BSL-2 models. a CellTiter-Glo® viability results of HEK293 cells. **a** HEK293 cells were treated with fendiline for 24 hours (black line) and 48 hours (blue line) and viability was assessed as a % viability of control. **b** PS saturation analysis from lipidomic analysis (LC/MS/MS) of total lipids extracted from HEK293 cells treated with the indicated concentration of fendiline (48 hours). Values are normalized to DMSO control and are reported as mean ± s.d.; n=3; A one-way ANOVA was performed with multiple comparisons compared to the control DMSO. **c** PA level analysis from lipidomic analysis (LC/MS/MS) of total lipids extracted from HEK293 cells treated with 5 μM fendiline (48 hours). Values are normalized to DMSO control and are reported as mean ± s.d.; n=3; A two-tailed t-test was performed. **d-e** Analysis of PS plasma membrane localization in response to 24 hour fendiline treatment. **d** Representative confocal images from live cell imaging of HEK293 cells expressing GFP-LactC2 and treated with fendiline for 24 hours; scale bars= 10 μm. **d** Effect of fendiline on PS plasma membrane localization was calculated by the ratio of GFP fluorescence at the (plasma membrane intensity/intracellular intensity). Values are normalized to DMSO control and are reported as mean ± s.d.; N>15, n=3; A one-way ANOVA was performed with multiple comparisons compared to the DMSO control. **p=0.0045; ***p=0.0003. **f** N&B analysis of HEK293 cells expressing the control GFP. Analysis was performed at 48 hours post treatment (DMSO) to align with N&B analysis performed on experiments with HEK293 cells expressing GFP-LactC2 or GFP-eVP40 and treated with the control or fendiline. *Left panel:* Representative images from time-lapse (30 frames) of HEK293 expressing EGFP and treated with fendiline for 48 hours. scale bar = 5 μm. *Middle panel:*

bioRxiv preprint doi: https://doi.org/10.1101/2021.06.08.447555; this version posted June 8, 2021. The copyright holder for this preprint (which was not certified by peer review) is the author/funder. All rights reserved. No reuse allowed without permission.

Brightness and Intensity plots for representative image. *Right panel:* Selection map correlating each pixel in the representative image to an oligomerization state (b value) (red: monomer). PS: phosphatidylserine; PA: phosphatidic acid; N&B: number & brightness analysis.

Expanded View 5 (EV5)

Vero E6 toxicity and effect of fendiline on eVP40 plasma membrane localization at 24 hours post treatment. a CellTiter-Glo® viability results of Vero cells. Cells were treated with control or fendiline for 48 hours according to the BSL-4 infection model; d-1/0 (black line), e.d. (blue line) and e.o.d (gray line) and viability was assessed as a % viability of control. **b-c** Effect of fendiline on eVP40 PM localization in HEK293 cells after 24 hours of treatment. **b** Representative confocal images from live cell imaging experiments of HEK293 cells expressing EGFP-WT-eVP40 after 48 hours of fendiline treatment. scale bars= 10 µm. **c** Effect of fendiline on eVP40 PM localization was quantified by the ratio of EGFP fluorescence intensity at the PM / total GFP fluorescence intensity (and normalized to DMSO control). N>15, n=3. Values are reported as mean ± s.d. A one-way ANOVA with multiple comparisons was performed compared to the DMSO control. PM: plasma membrane.

Expanded View 6 (EV6)

Thermal melting of eVLPs produced in the presence and absence of fendiline. a Ebola virus-like particles (eVLPs) were produced in DMSO treated HEK293 cells expressing FLAG-eVP40 and eGP constructs which were then collected, purified, and melted while measuring the loss in polarized light absorption at 220 nm. **b** Prior to melting, the circular dichroism spectra of DMSO

bioRxiv preprint doi: https://doi.org/10.1101/2021.06.08.447555; this version posted June 8, 2021. The copyright holder for this preprint (which was not certified by peer review) is the author/funder. All rights reserved. No reuse allowed without permission.

VLPs was measured alongside the absorbance and detector (hv) signals. **c** Ebola VLPs were produced in 5 μM fendiline treated HEK293 cells using the same FLAG-eVP40 and eGP constructs which were then collected, purified and melted while measuring the loss in polarized light absorption at 220 nm. **d** Prior to melting, the circular dichroism spectra of Fendiline VLPs was measured alongside the absorbance and detector (hv) signals.

Expanded View 7 (EV7)

Calibration results from the first and second phase of model development. a-c First phase calibration results between experimental (black bars) and simulation (gray) data from budding **(a-b)** and entry **(c)** assays. **d-e** Second phase calibration results showing comparison between experimental and simulation data from cell viability assays. The mathematical model was calibrated to this data and the data in Figure 8 in the main text simultaneously.

bioRxiv preprint doi: https://doi.org/10.1101/2021.06.08.447555; this version posted June 8, 2021. The copyright holder for this preprint (which was not certified by peer review) is the author/funder. All rights reserved. No reuse allowed without permission.

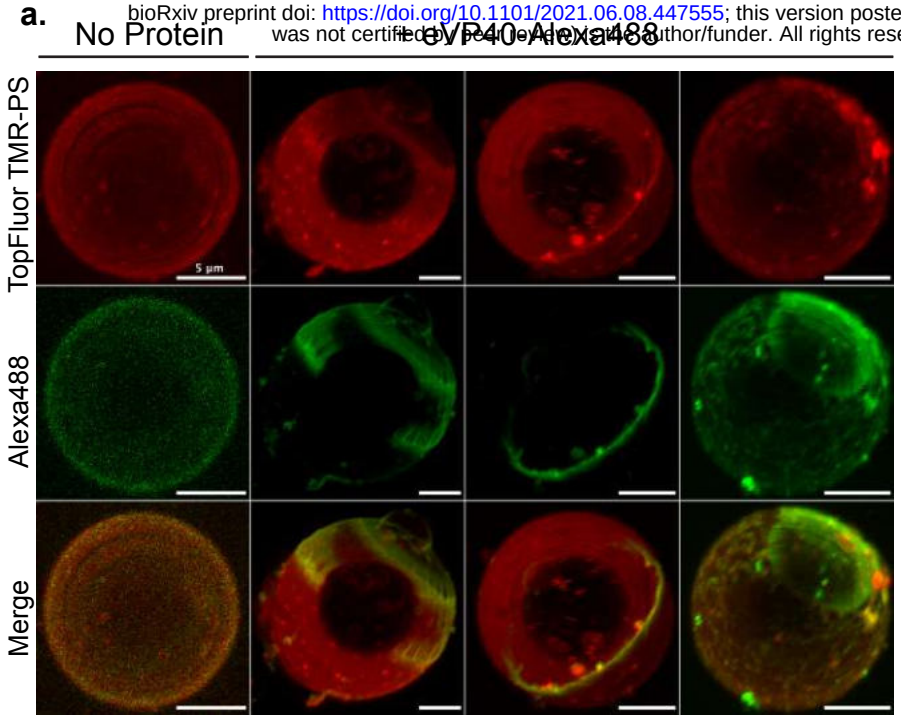

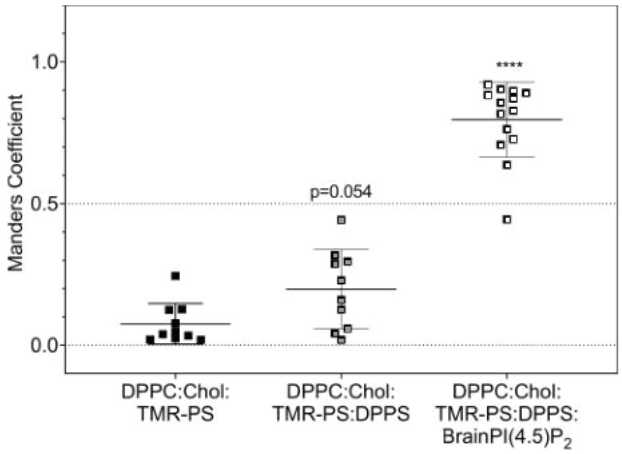

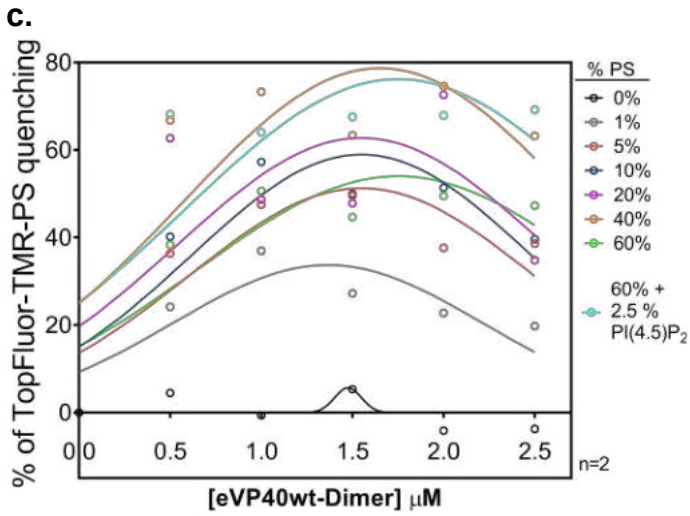

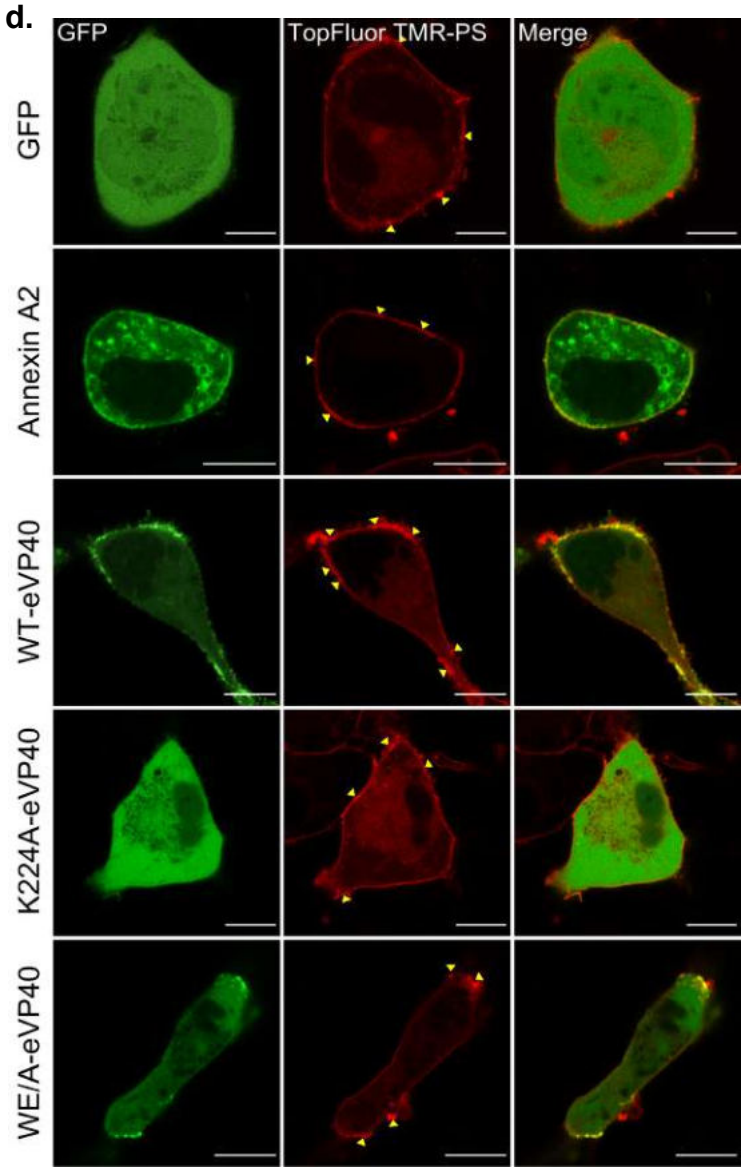

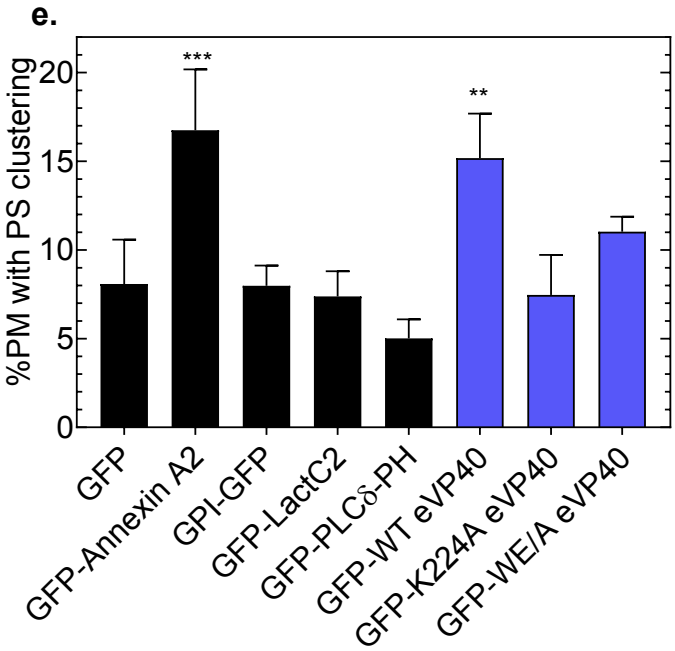

bioRxiv preprint doi: https://doi.org/10.1101/2021.06.08.447555; this version posted June 8, 2021. The copyright holder for this preprint (which was not certified by peer review) is the author/funder. All rights reserved. No reuse allowed without permission.

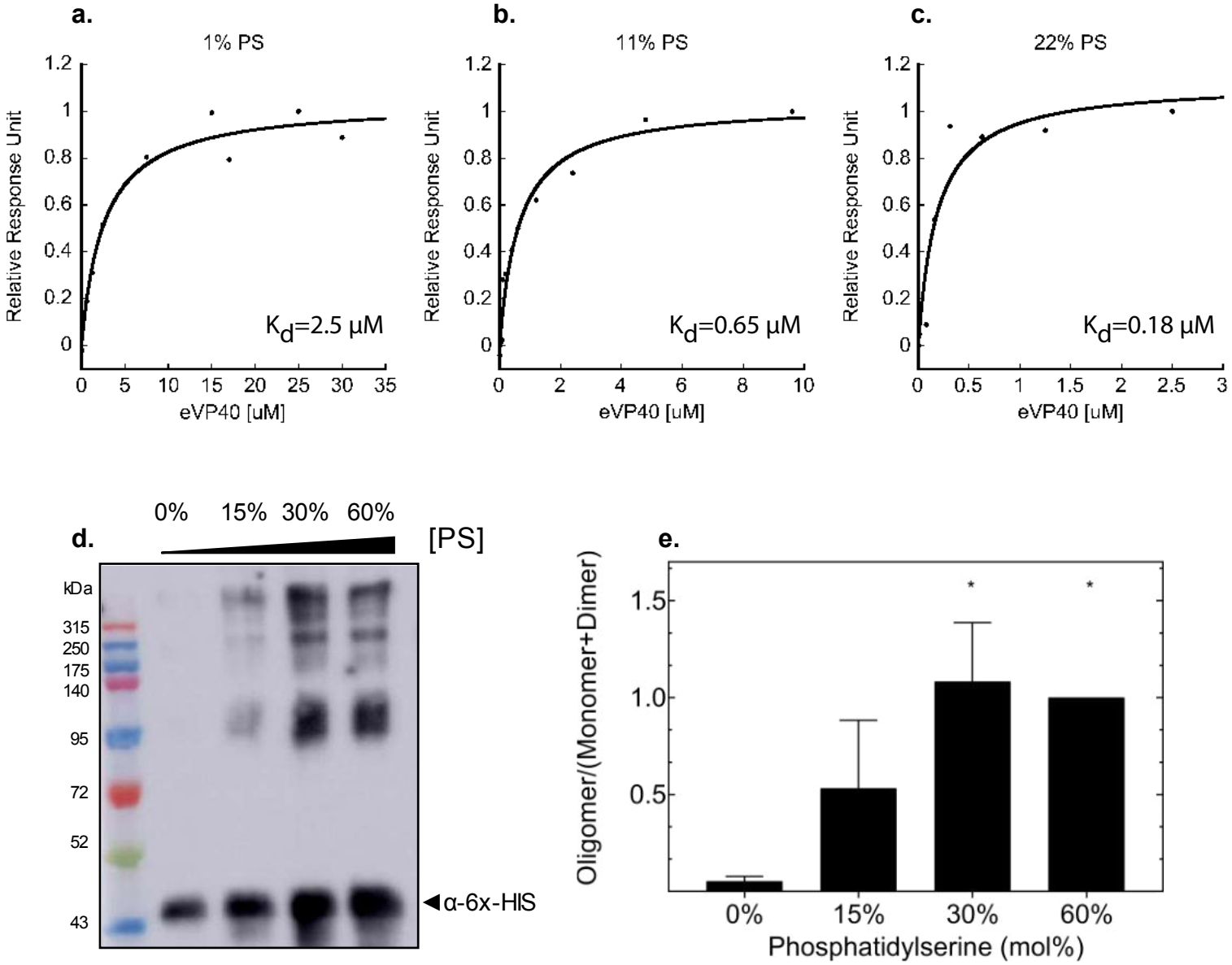

bioRxiv preprint doi: https://doi.org/10.1101/2021.06.08.447555; this version posted June 8, 2021. The copyright holder for this preprint (which was not certified by peer review) is the author/funder. All rights reserved. No reuse allowed without permission.

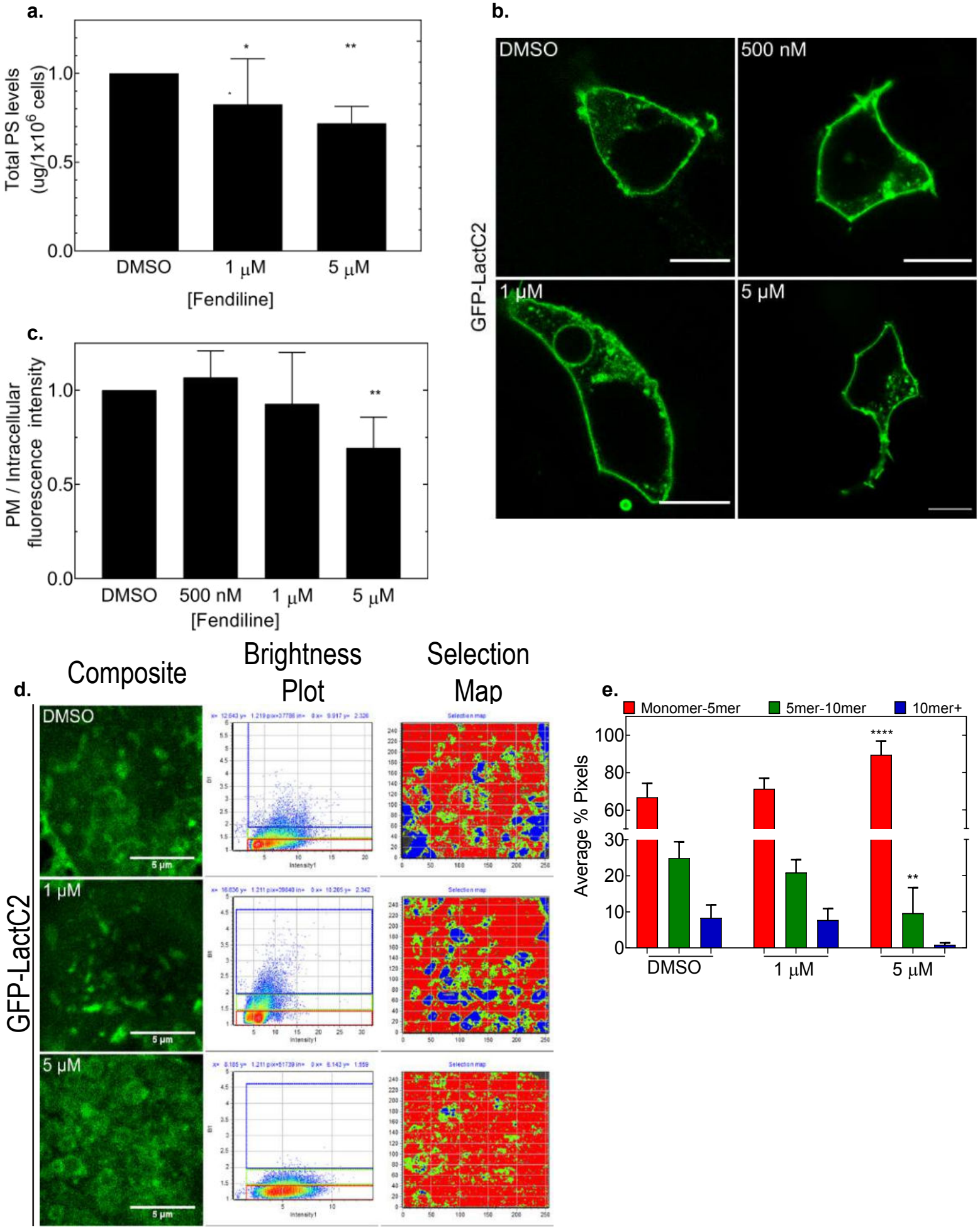

bioRxiv preprint doi: https://doi.org/10.1101/2021.06.08.447555; this version posted June 8, 2021. The copyright holder for this preprint (which was not certified by peer review) is the author/funder. All rights reserved. No reuse allowed without permission.

EBOV - Fendiline Treated

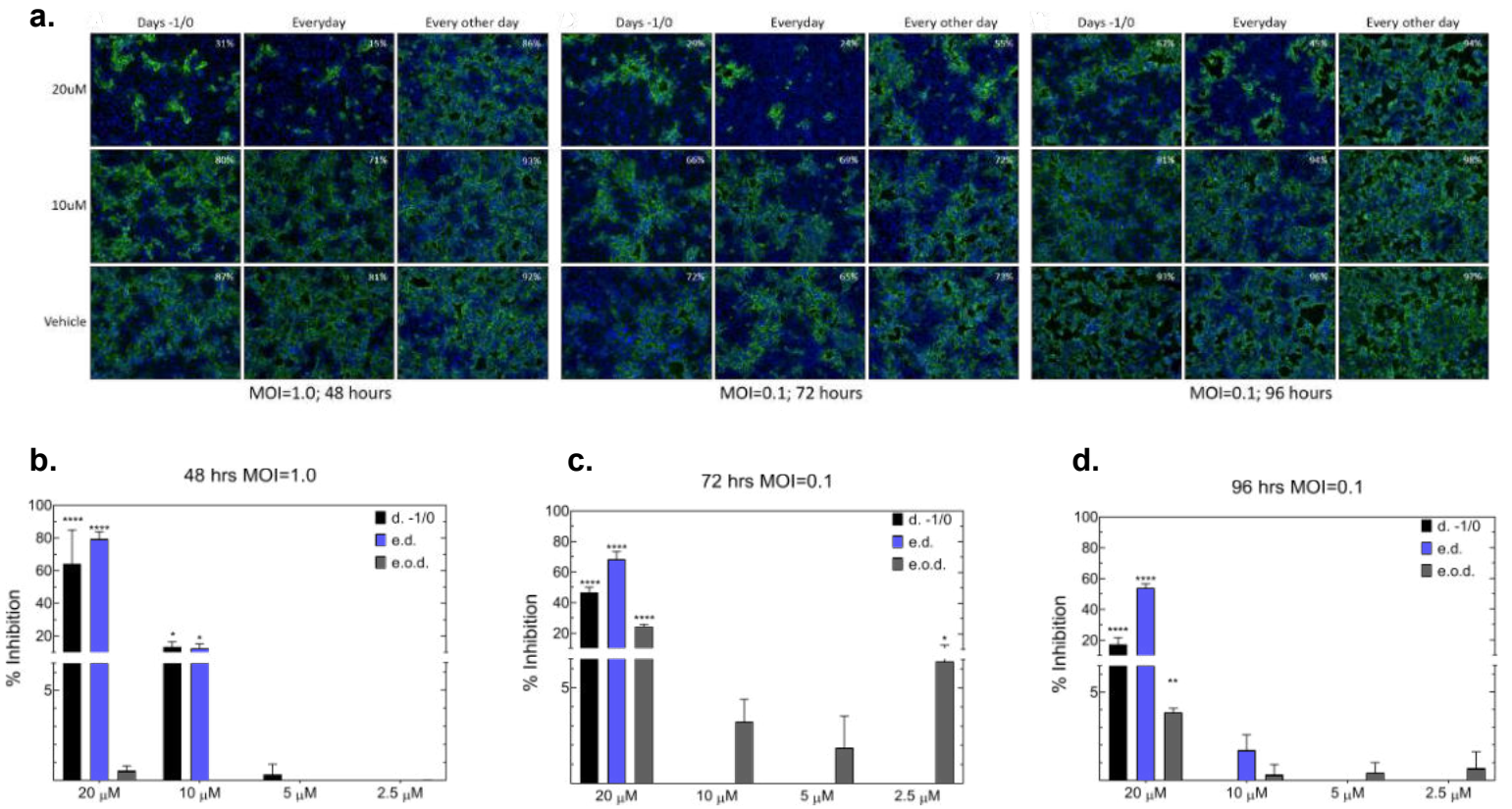

MARV - Fendiline Treated

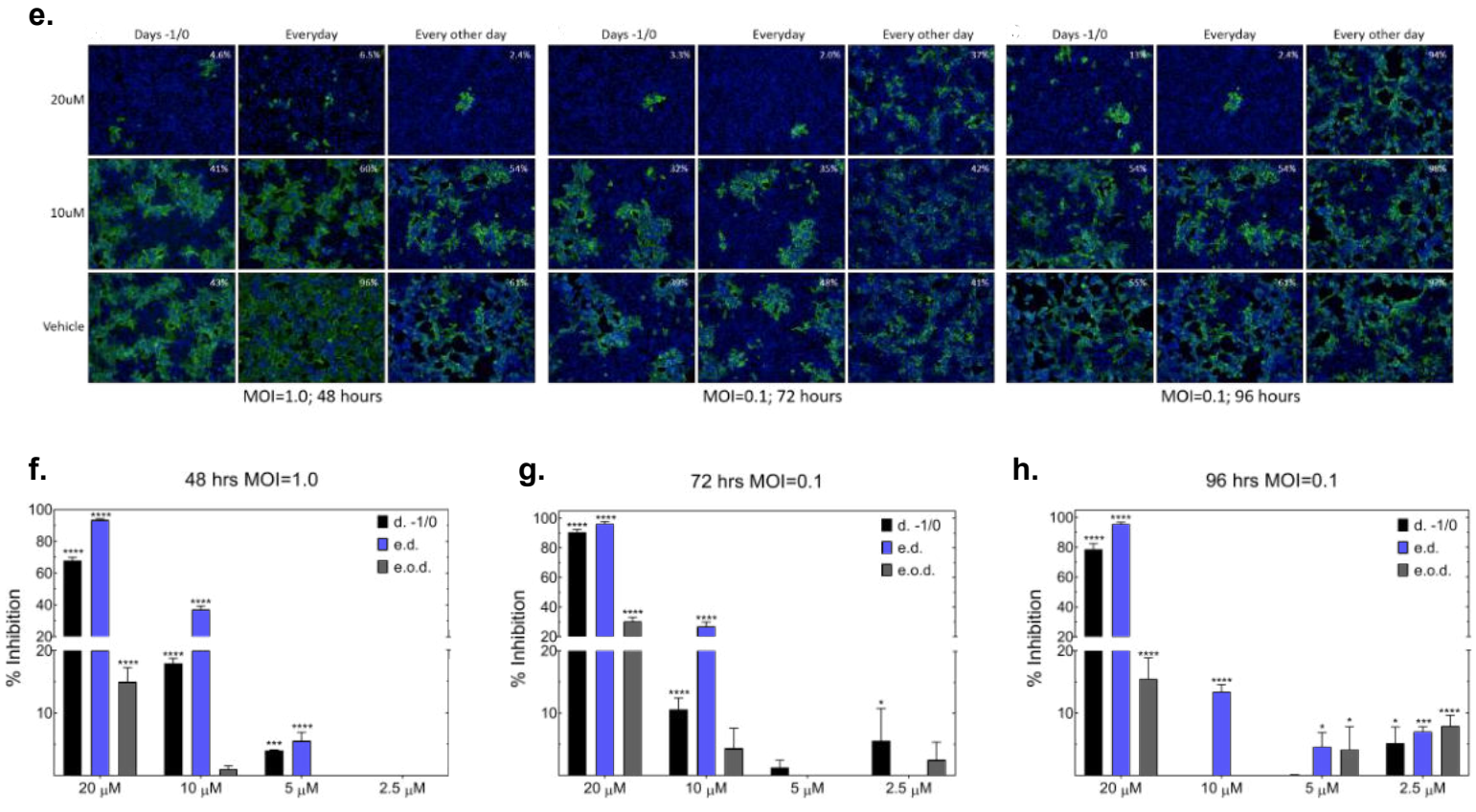

bioRxiv preprint doi: https://doi.org/10.1101/2021.06.08.447555; this version posted June 8, 2021. The copyright holder for this preprint (which was not certified by peer review) is the author/funder. All rights reserved. No reuse allowed without permission.

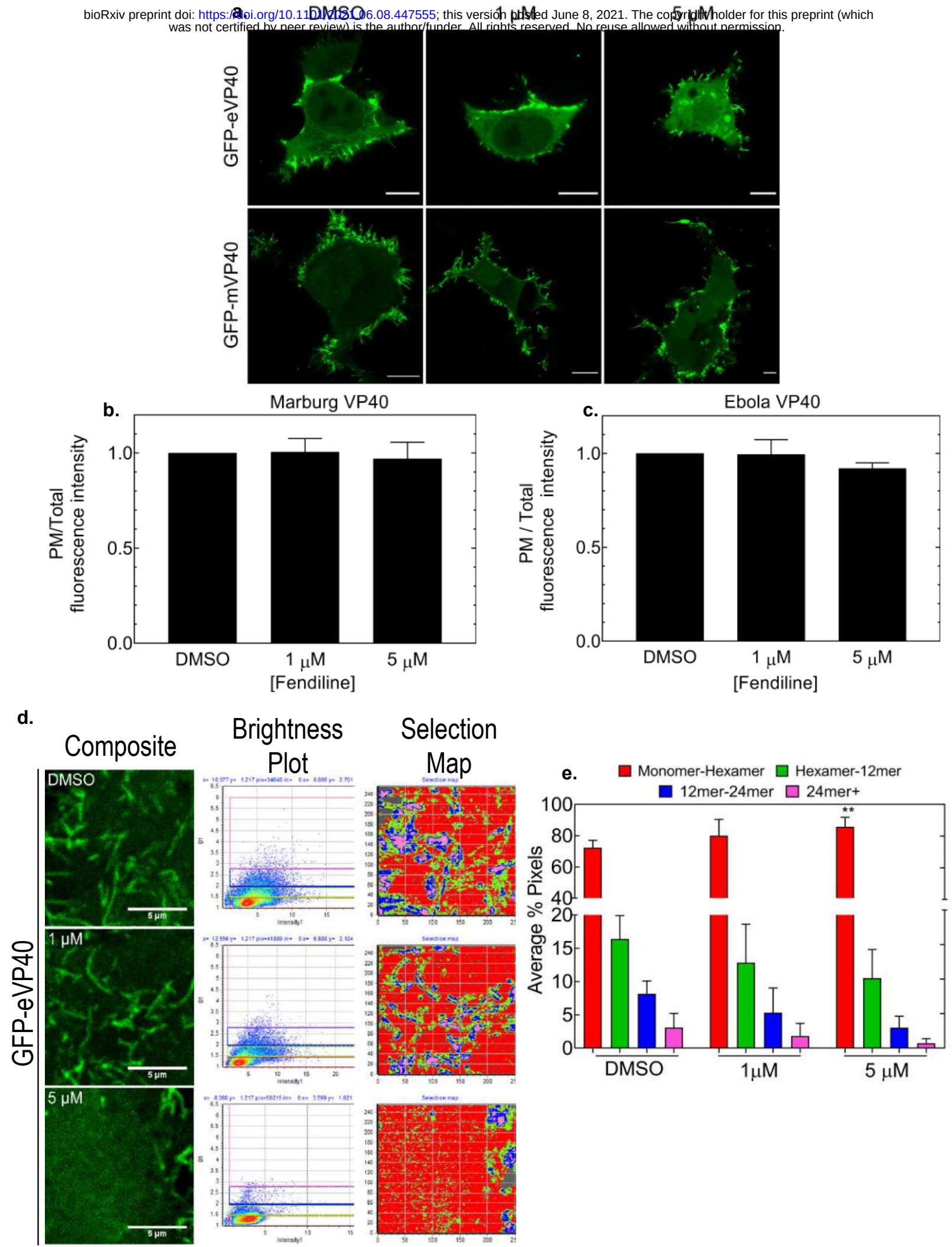

bioRxiv preprint doi: https://doi.org/10.1101/2021.06.08.447555; this version posted June 8, 2021. The copyright holder for this preprint (which was not certified by peer review) is the author/funder. All rights reserved. No reuse allowed without permission.

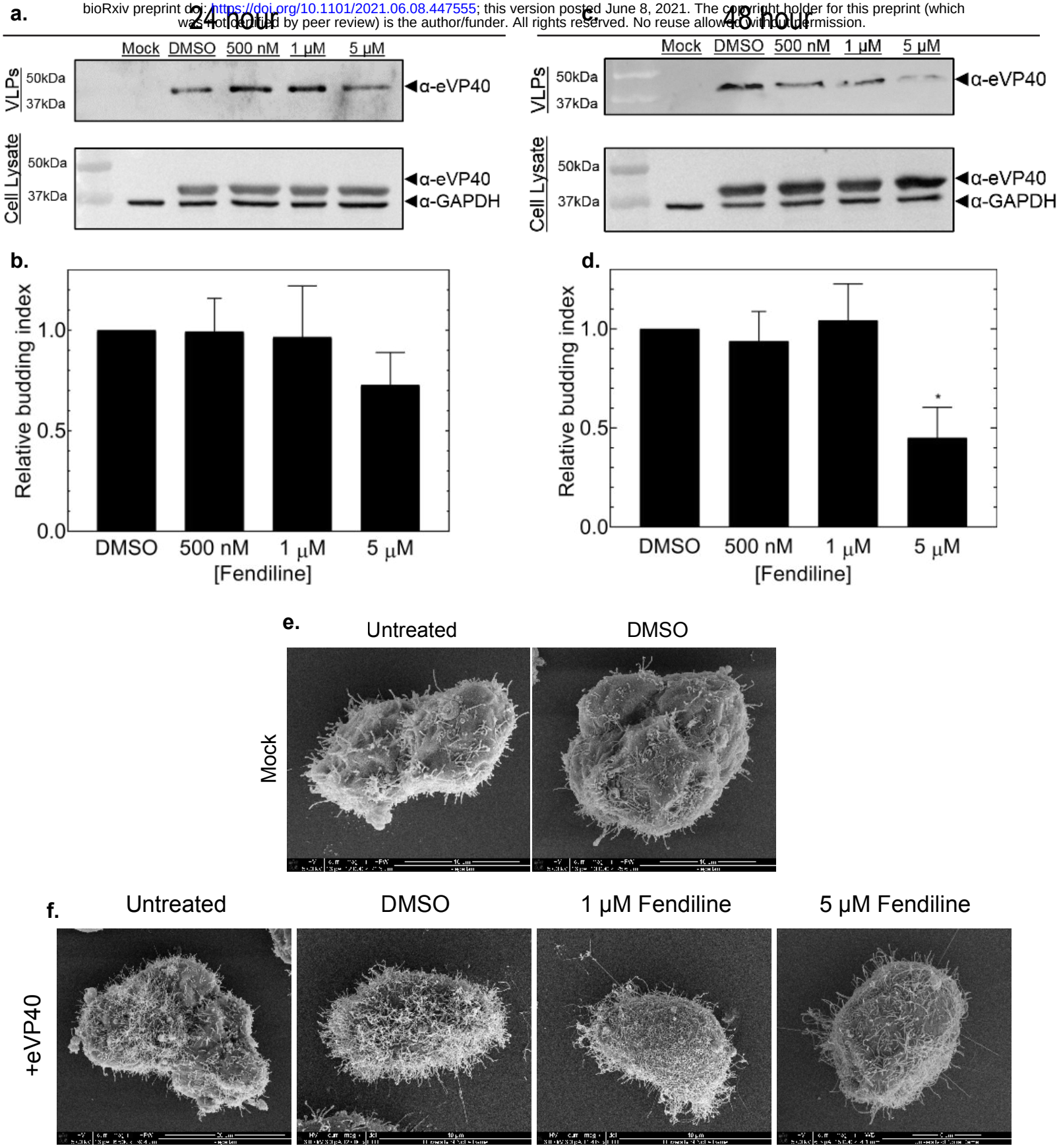

bioRxiv preprint doi: https://doi.org/10.1101/2021.06.08.447555; this version posted June 8, 2021. The copyright holder for this preprint (which was not certified by peer review) is the author/funder. All rights reserved. No reuse allowed without permission.

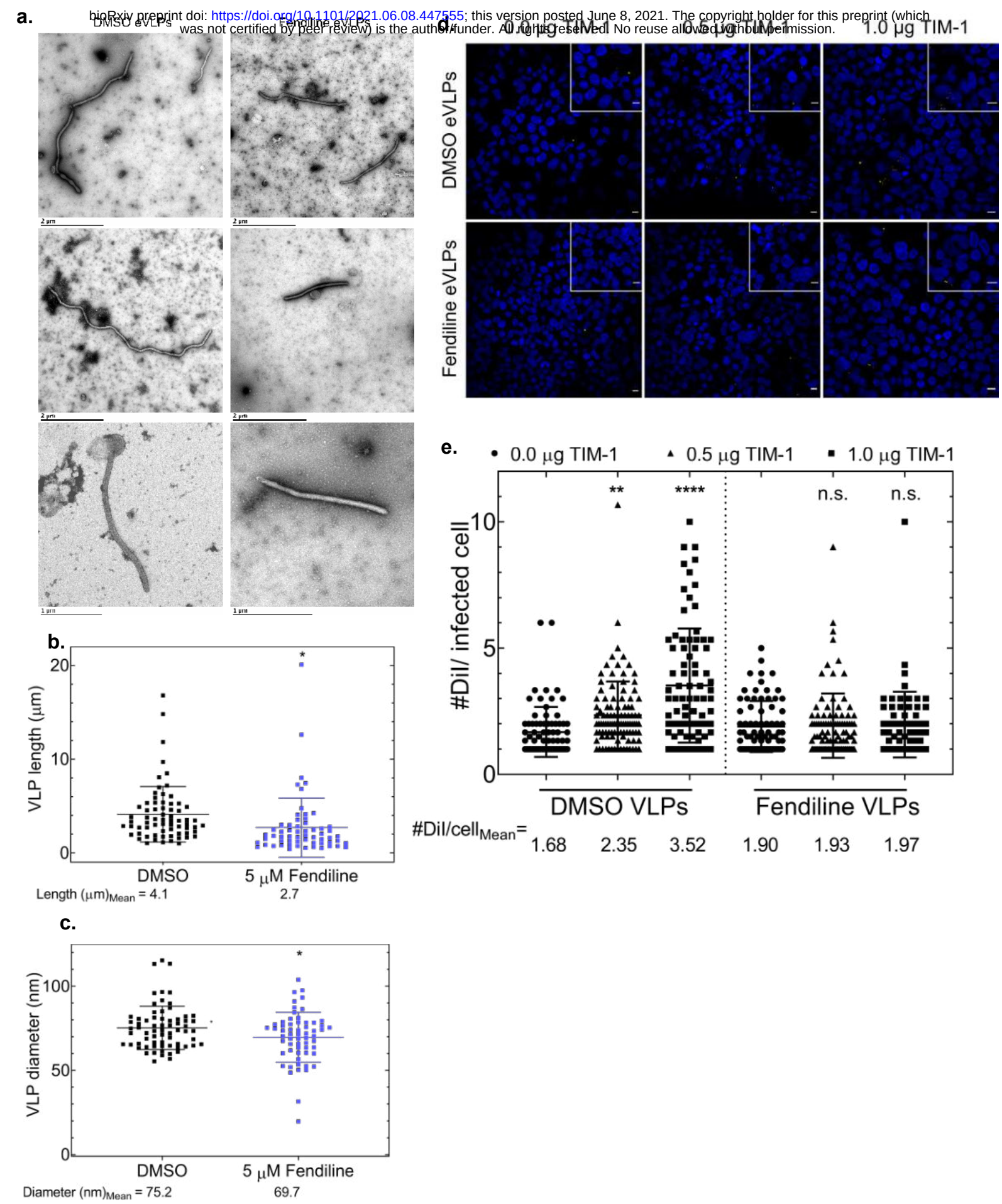

bioRxiv preprint doi: https://doi.org/10.1101/2021.06.08.447555; this version posted June 8, 2021. The copyright holder for this preprint (which was not certified by peer review) is the author/funder. All rights reserved. No reuse allowed without permission.

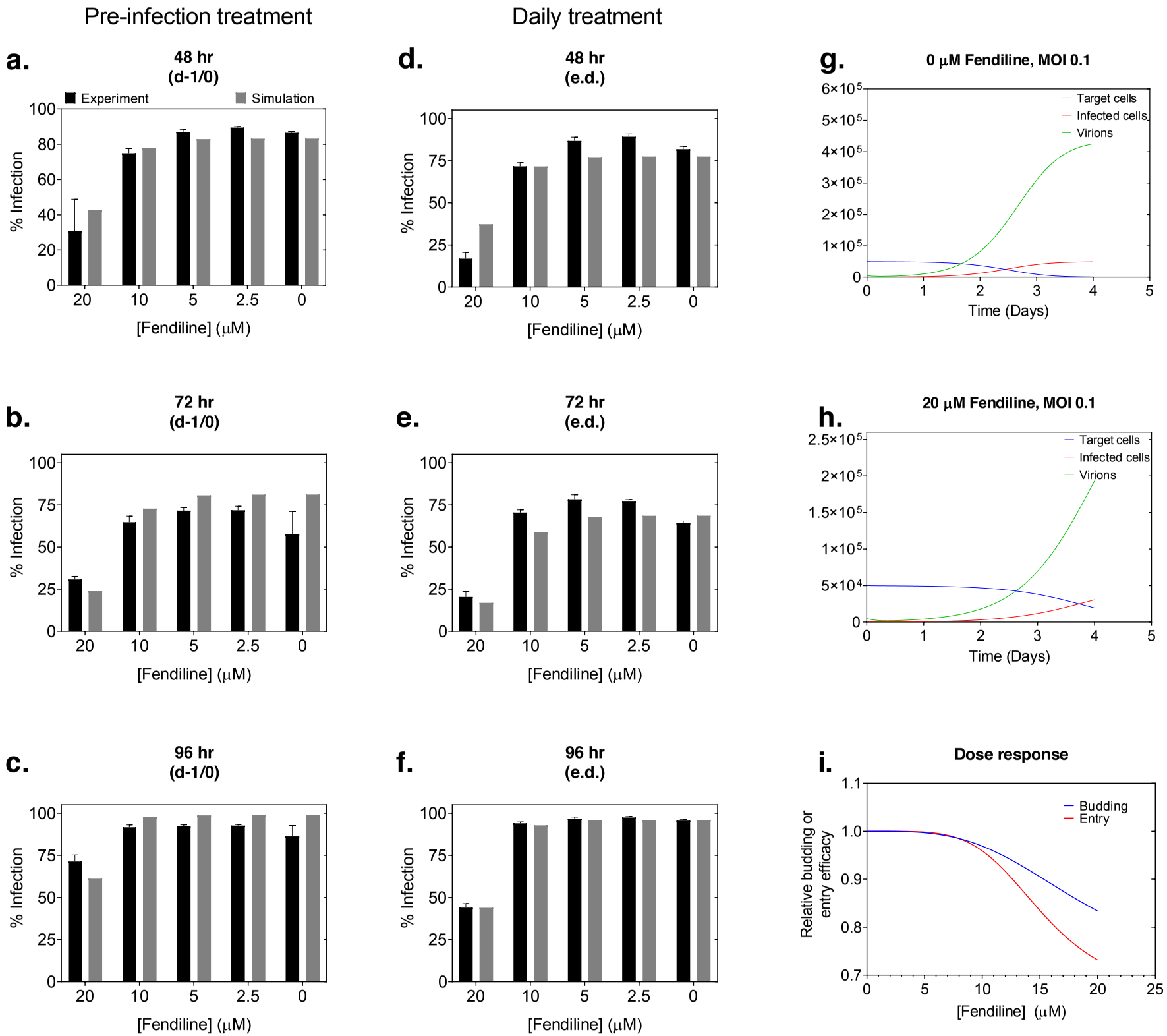

bioRxiv preprint doi: https://doi.org/10.1101/2021.06.08.447555; this version posted June 8, 2021. The copyright holder for this preprint (which was not certified by peer review) is the author/funder. All rights reserved. No reuse allowed without permission.

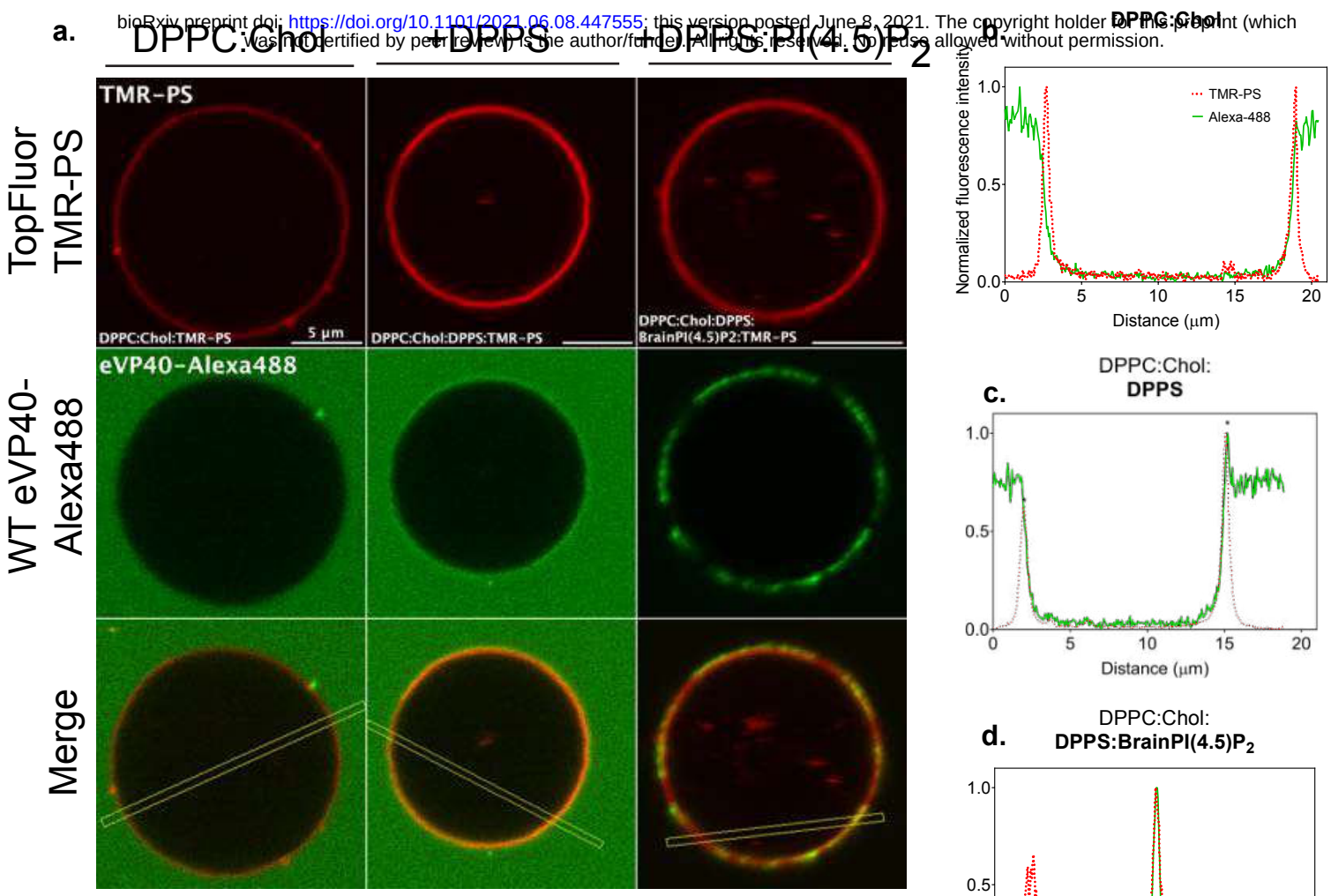

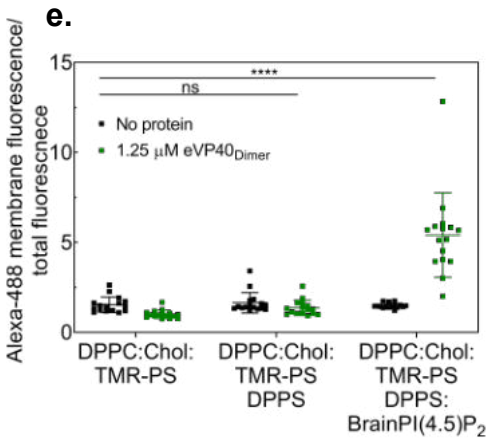

EV1

bioRxiv preprint doi: https://doi.org/10.1101/2021.06.08.447555; this version posted June 8, 2021. The copyright holder for this preprint (which was not certified by peer review) is the author/funder. All rights reserved. No reuse allowed without permission.

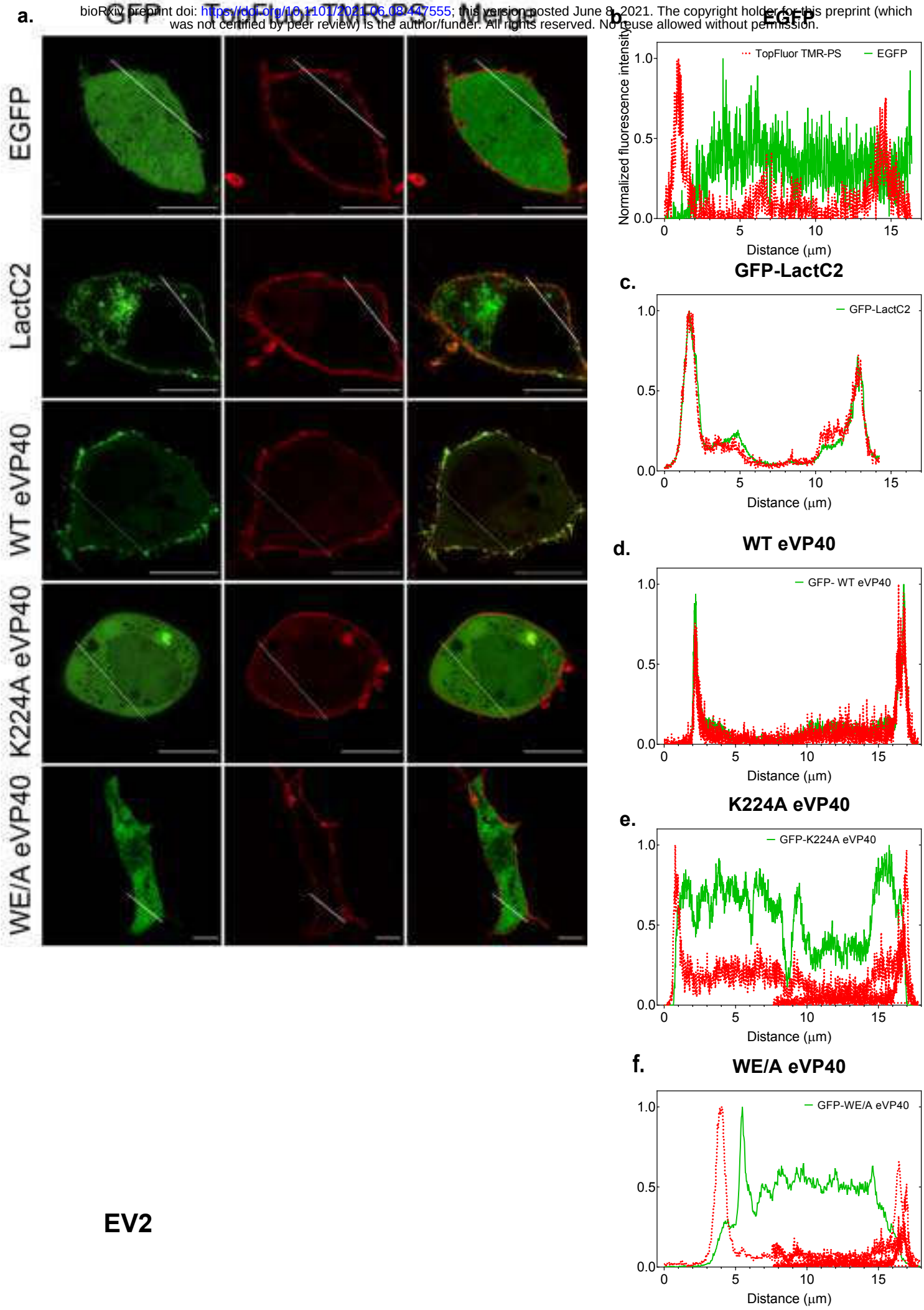

EV2

bioRxiv preprint doi: https://doi.org/10.1101/2021.06.08.447555; this version posted June 8, 2021. The copyright holder for this preprint (which was not certified by peer review) is the author/funder. All rights reserved. No reuse allowed without permission.

a.

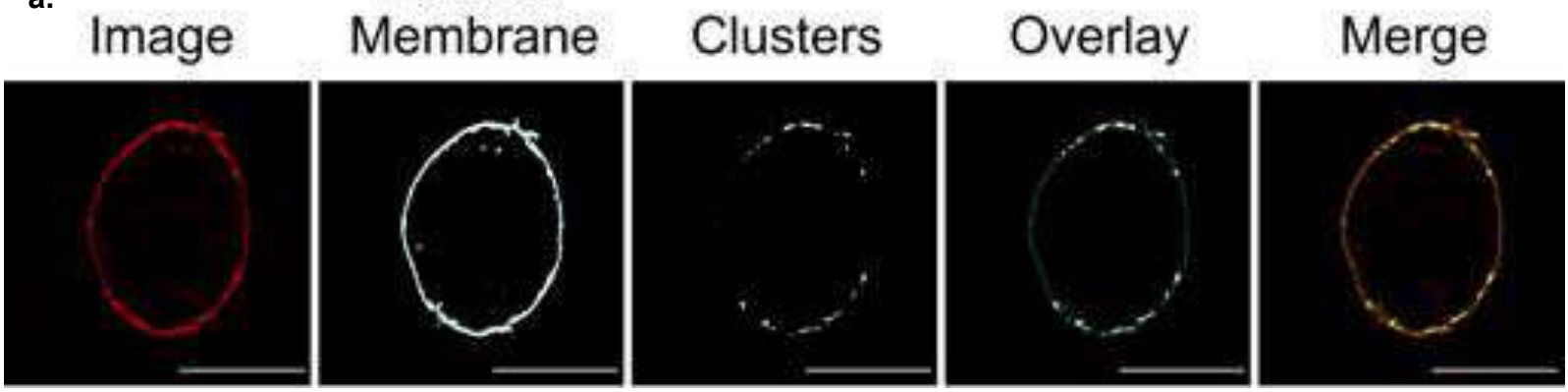

b.

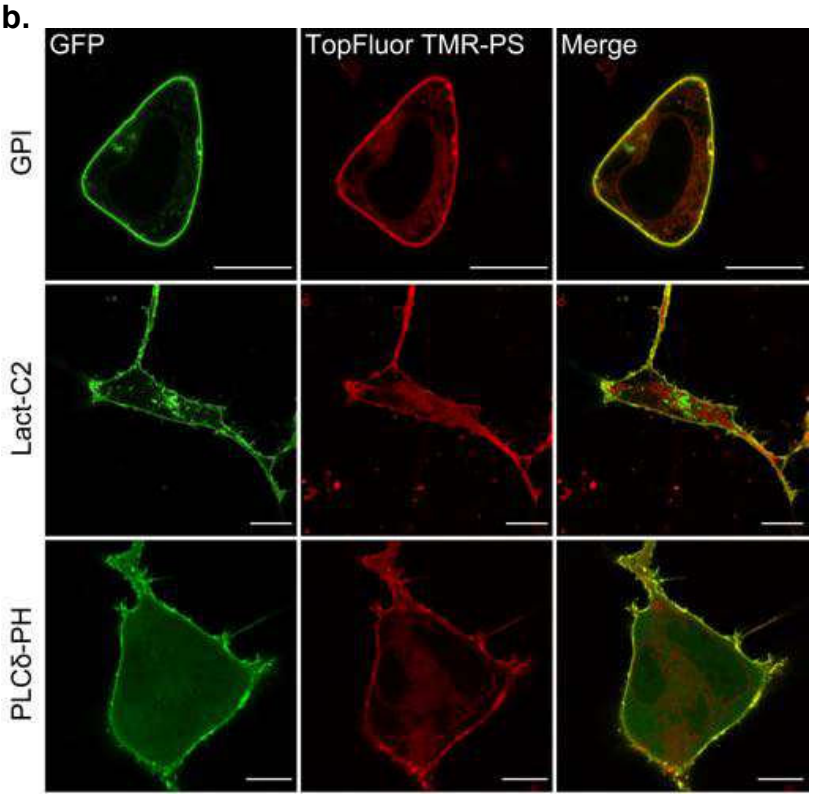

EV3

bioRxiv preprint doi: https://doi.org/10.1101/2021.06.08.447555; this version posted June 8, 2021. The copyright holder for this preprint (which was not certified by peer review) is the author/funder. All rights reserved. No reuse allowed without permission.

a.

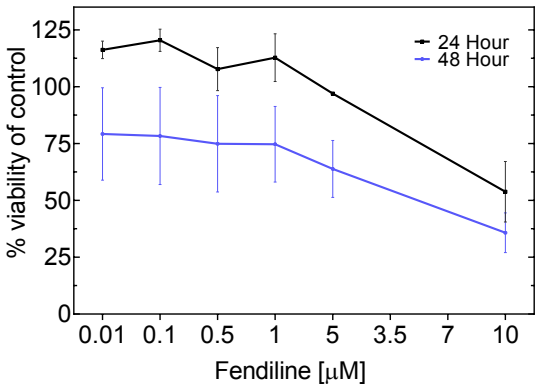

b.

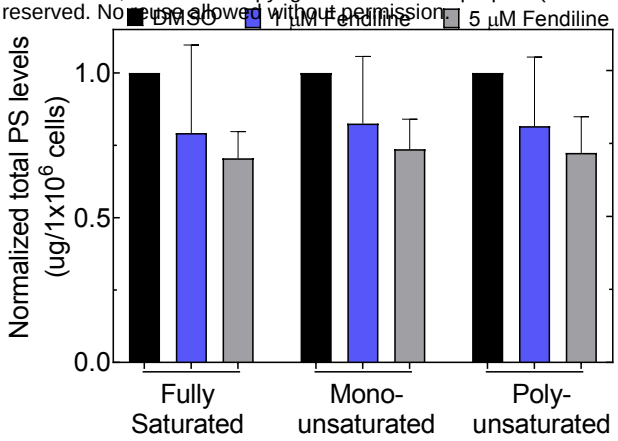

c.

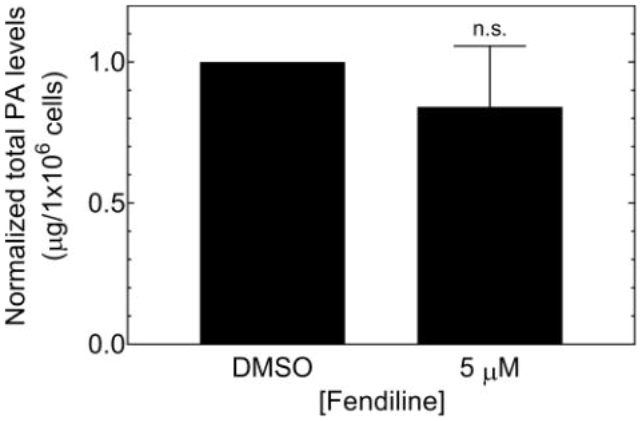

e.

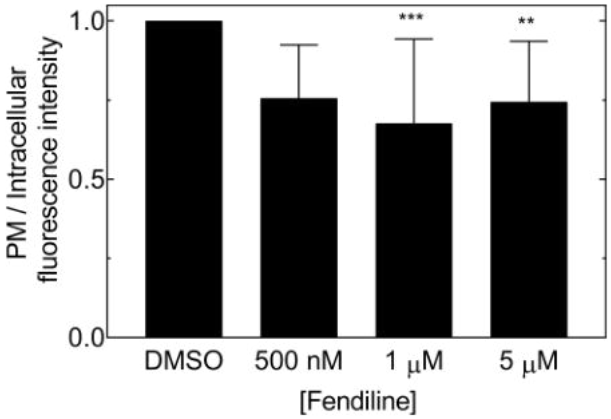

d.

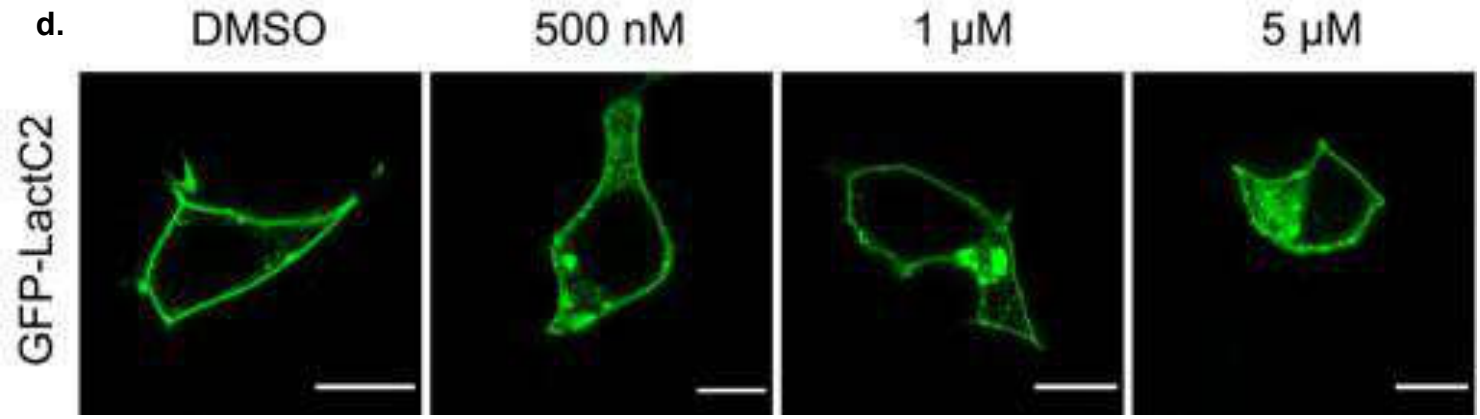

f.

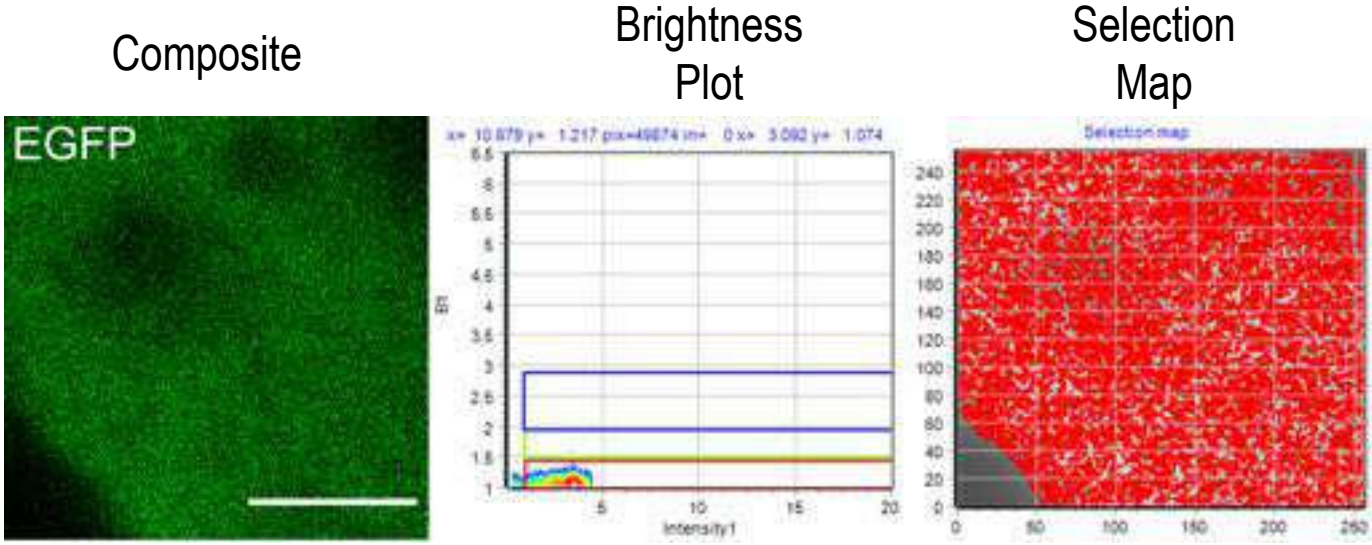

EV4

bioRxiv preprint doi: https://doi.org/10.1101/2021.06.08.447555; this version posted June 8, 2021. The copyright holder for this preprint (which was not certified by peer review) is the author/funder. All rights reserved. No reuse allowed without permission.

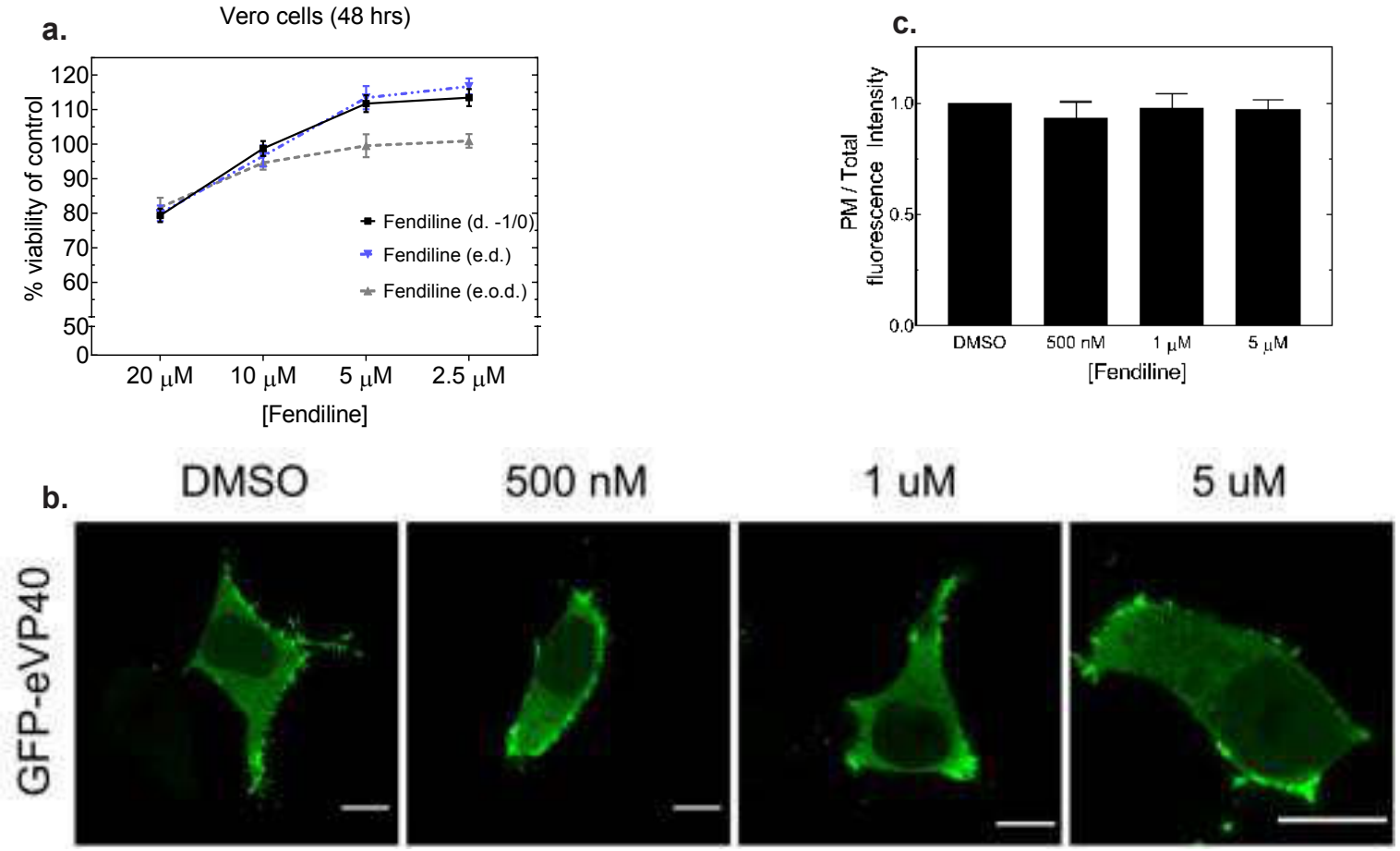

EV5

bioRxiv preprint doi: https://doi.org/10.1101/2021.06.08.447555; this version posted June 8, 2021. The copyright holder for this preprint (which was not certified by peer review) is the author/funder. All rights reserved. No reuse allowed without permission.

a.

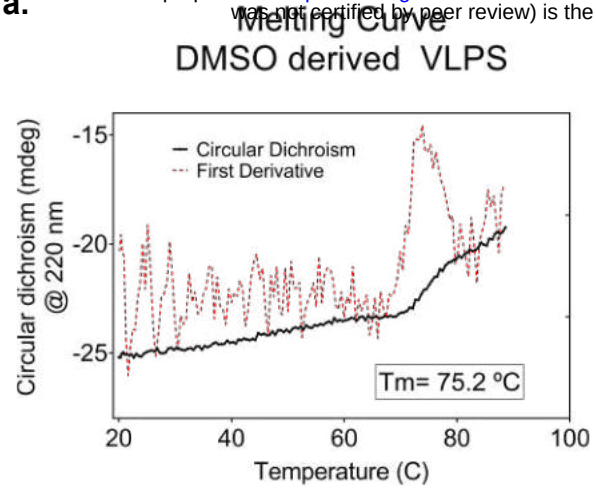

c.

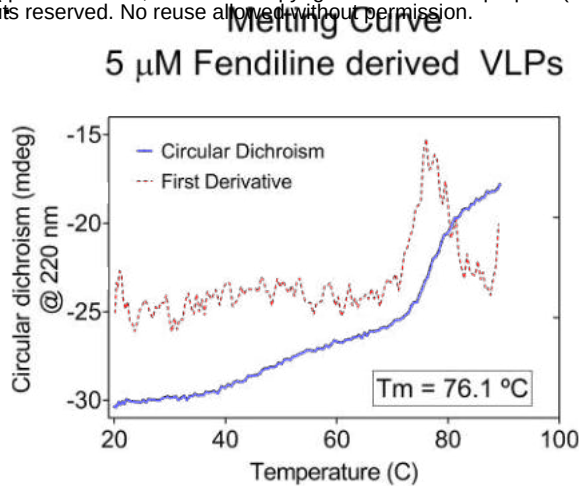

b.

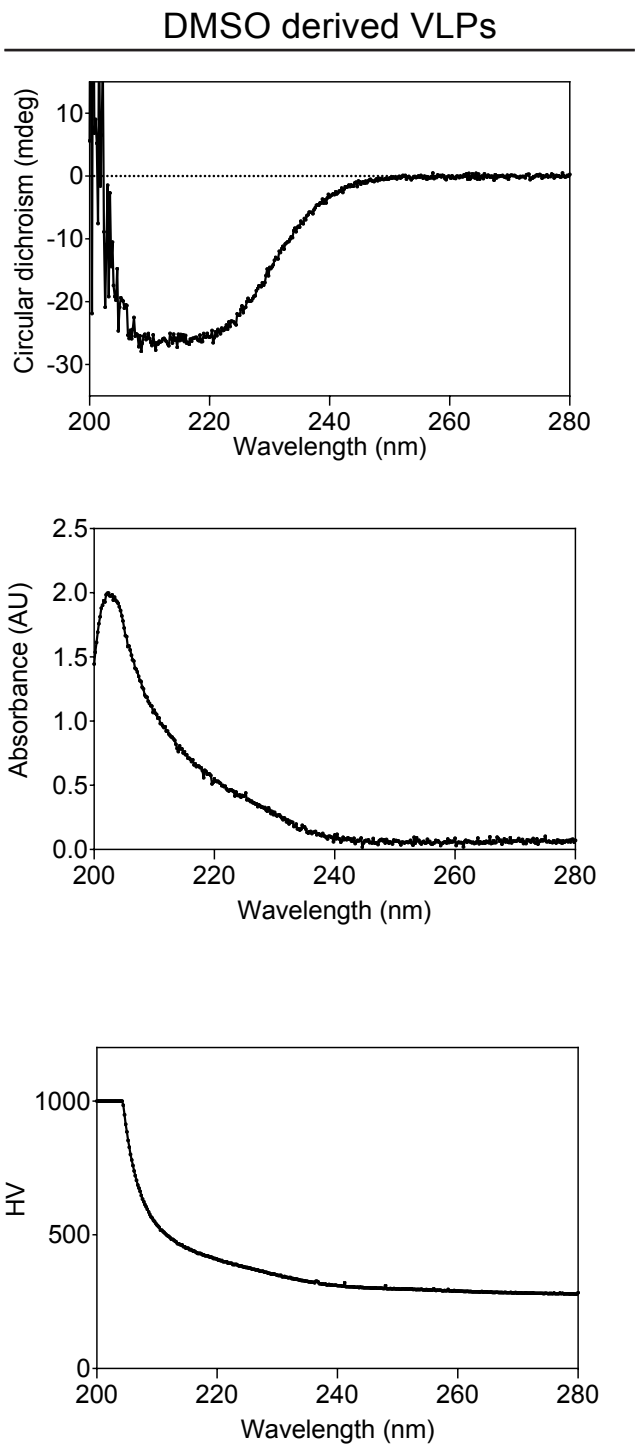

d.

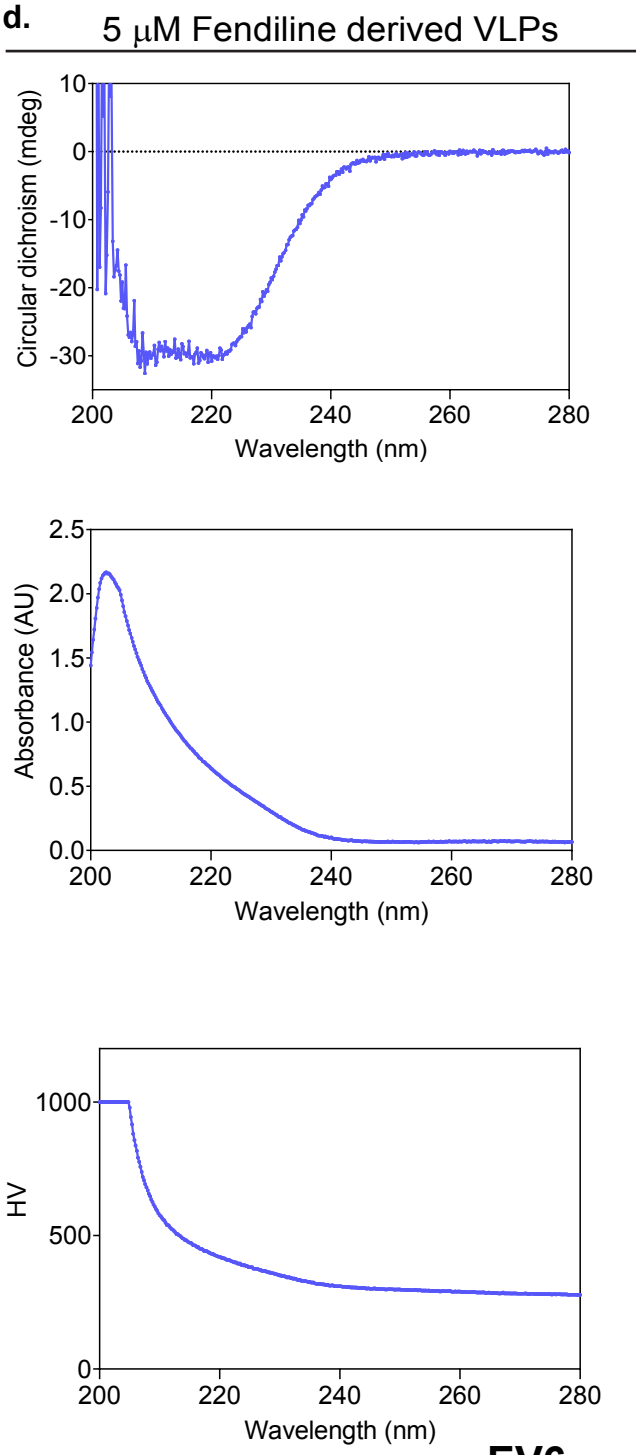

EV6

bioRxiv preprint doi: https://doi.org/10.1101/2021.06.08.447555; this version posted June 8, 2021. The copyright holder for this preprint (which was not certified by peer review) is the author/funder. All rights reserved. No reuse allowed without permission.

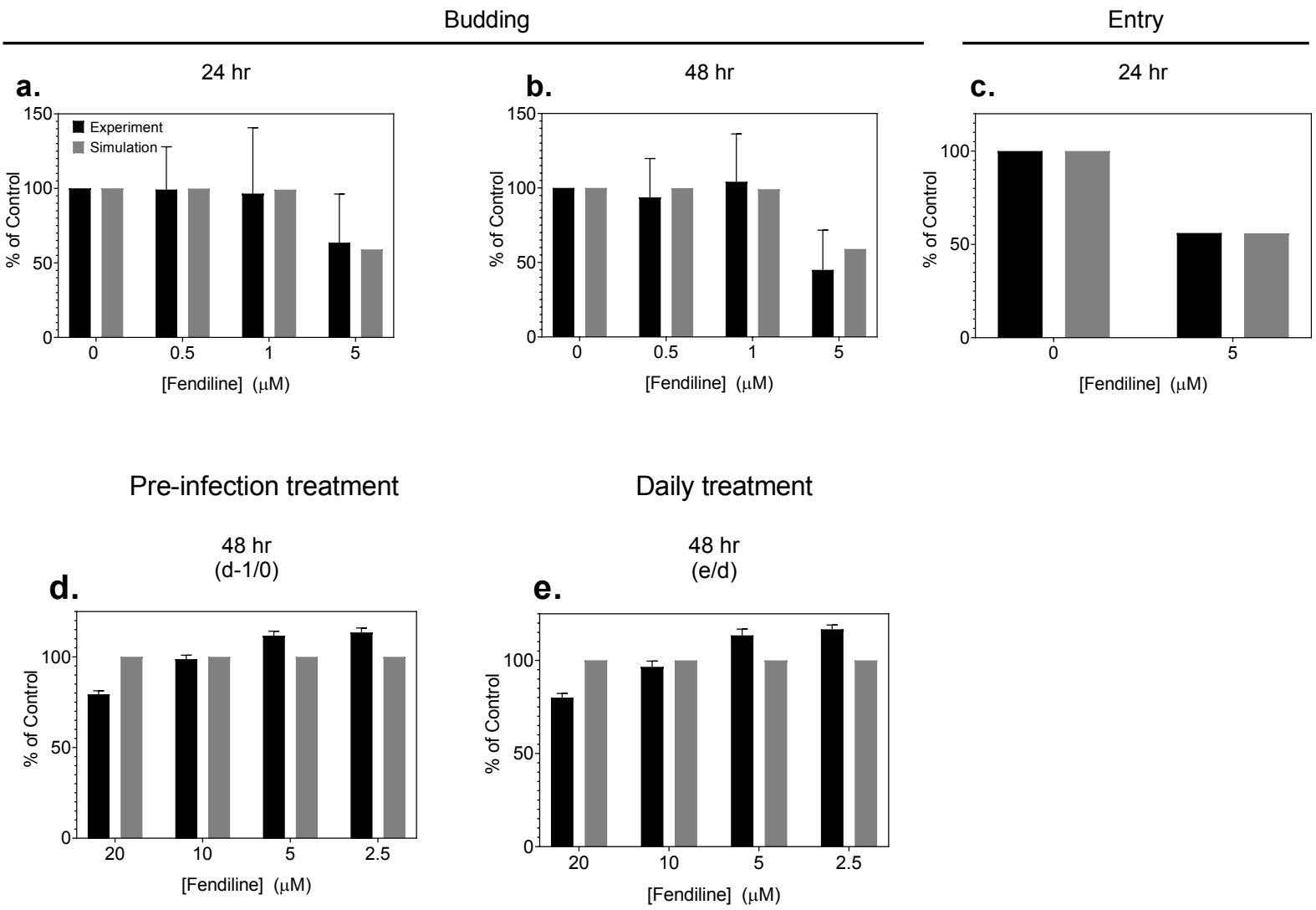

EV7